國立交通大學

電子工程學系 電子研究所碩士班

碩士論文

利用大氣電漿沉積以氧化鋅為主的透明導電膜其光電特性和熱穩定性的研究

Investigation on Opto-electrical Properties and Thermal Stability of Zinc Oxide Based Transparent Conductive Oxides Prepared by Atmospheric Pressure Plasma Jet

研究生：林煒力

指導教授：張國明 博士

中華民國 九十九 年 八 月

利用大氣電漿沉積以氧化鋅為主的透明導電膜其光電特性和熱穩定性的研究

Investigation on Opto-electrical Properties and Thermal Stability of Zinc Oxide Based Transparent Conductive Oxides Prepared by Atmospheric Pressure Plasma Jet

研究生：林煒力　　Student：Wei-Li Lin

指導教授：張國明 博士　　Advisor：Dr. Kow-Ming Chang

國立交通大學

電子工程學系 電子研究所碩士班

碩士論文

A Thesis
Submitted to Department of Electronics Engineering and Institute of
Electronics College of Electrical and Computer Engineering
National Chiao Tung University
in Partial Fulfillment of the Requirements
for the Degree of Master
in
Electronics Engineering
August 2010
Hsinchu, Taiwan

中華民國九十九年八月

利用大氣電漿沉積以氧化鋅為主的透明導電膜
其光電特性和熱穩定性的研究

研究生：林煒力　　　　　　　　　　指導教授：張國明 博士

國立交通大學

電子工程學系 電子研究所碩士班

摘要

於本論文中，我們利用大氣電漿化學氣相沉積法去成長以氧化鋅為主的透明導電膜，包含了氧化鋅摻雜銦、氧化鋅摻雜鋁和氧化鋅摻雜鎵。我們將研究不同的摻雜濃度和基板溫度對這些薄膜在表面型態、結構、電性和光學的影響。並且我們也將探討氧化鋅摻雜銦和氧化鋅摻雜鎵在高溫處理下的熱穩定性。所有薄膜都顯現出垂直基板之(002)晶向的結構。摻雜八個原子百分濃度和兩百度的氧化鋅摻雜銦有最佳的電性表現，電阻值為 1.71E-3 Ωcm。氧化鋅摻雜銦在光學性質上的表現都比氧化鋅摻雜鋁好，穿透率在可見光範圍約 85%左右。在熱穩定性的表現上面，即使在高溫的氧氣環境下，氧化鋅摻雜銦的穩定性仍比氧化鋅摻雜鎵還要好。我們的研究顯示：氧化鋅摻雜銦是很有希望被應用在下一個世代的透明導電薄膜上面。

Investigation on Opto-electrical Properties and Thermal Stability of Zinc Oxide Based Transparent Conductive Oxides Prepared by Atmospheric Pressure Plasma Jet

Student：Wei-Li Lin　　Advisor：Dr. Kow-Ming Chang

Department of Electronics Engineering and Institute of Electronics
National Chiao Tung University, Hsinchu, Taiwan

Abstract

In this thesis, we use the APPCVD system to deposit the ZnO based transparent conductive oxides (TCO), including IZO, AZO and GZO. The effect of different doping concentration and substrate temperature on the morphological, structural, electrical and optical properties of the thin films has been investigated. Moreover, we investigate the thermal stability of IZO and GZO at different annealing conditions. All films show the preferred (002) orientation perpendicular to the substrate. The minimum resistivity of 1.7E-3 Ωcm was obtained at a substrate temperature of 200℃ and 8 at% indium-doped. The transmittance of IZO thin films were around 85% in the visible spectrum. The IZO thin films show better transmittance than the AZO films. It is shown that the IZO thin films show better thermal stability than GZO films even in oxygen ambient at high temperature. Our study shows that the IZO thin films were a promising candidate for next generation TCO applications.

誌 謝

於本人碩士求學時間中，我首先要感謝指導老師張國明教授，讓我在研究和平常的做人處世上都獲益良多。除此之外，感謝王水進教授和龔正教授在口試中，對我的論文研究有進一步的探討和指教，讓我的想法可以更加廣泛。

其次感謝實驗室學長們的熱心指導，尤其是黃菘宏學長，在我的研究上提供了許多寶貴的意見，讓我可以順利的進行自己的實驗研究。另外也要感謝工業技術研究院(ITRI)、國家奈米元件實驗室(NDL)與國立交通大學奈米中心(NFC)提供良好的研究機台和實驗環境，讓我們能心無旁鶩的做好自己的實驗；且也要感謝林哲蔚先生、何惟梅小姐、姚潔宜小姐和沈奕伶小姐等人的協助下，讓我可以順利的進行並完成實驗的研究。

接著，我要感謝實驗室的同學們在我研究有問題的時候可以一起討論，並且提供適切的意見來幫助我，尤其是實驗夥伴吉家威和陳偉強在實驗上的助益更為重要，還有同組的學弟蔣偉韓能盡他所能幫助之力幫助我，才得以完成此論文。

最後，我要特別感謝家人對我的幫助和支持，女友思匀的陪伴，讓我可以順利的完成碩士學位。

Contents

Table Captions

Figure Captions

Chapter 1

Introduction

1.1 Transparent Conductive Oxide (TCO)

Transparent Conductive Oxide (TCO) films composed of binary compounds such as stannum oxide (SnO_2) [1,2], indium oxide (In_2O_3) [2,3] and zinc oxide (ZnO) [2,4] are widely used in transparent electrodes for photovoltaic devices [5-7] and touch panels [8], heat mirrors [9], amorphous silicon solar cells [10], flat panel display (FPD) [11], IR reflectors [12-14] and other optoelectronic devices [15-20]. Therefore, transparent conductive oxide (TCO) thin films have been the indispensable component to opto-electrical products.

Among these applications, TCO films must possess a high optical transmittance in the visible region (over 80%), a high electrical conductivity (about 10^{-3} Ω-cm), and stability in various environments. So far, indium-tin oxide (ITO) films which is the indium rich thin film prepared by sputtering system have been generally used as TCO films owing to their high transmittance in the visible range and low electrical resistivity. However, the indium is the rare-earth metal even less than gold, so it will be more expensive in the future. Hence, the decreasing of the indium content or other TCO materials becomes more popular investigation in recent years.

Transparent conductive impurity-doped zinc oxides, such as aluminum doped zinc oxide (AZO) [21-23], gallium doped zinc oxide (GZO) [24-27] and indium doped zinc oxide (IZO) [27-32] has recently attracted much attention for altering ITO films because of their non-toxicity, low material cost, relatively low deposition temperature and stability in hydrogen plasma. ZnO is an n-type wide band gap (Eg = 3.37eV) II-VI semiconductor with hexagonal structure. And it has a large exciton binding energy (60meV) [33] emitting blue emission in bulk form when it is pumped by an electron beam at cryogenic temperature [34,35]. In electrical conductivity is mainly due to zinc excess at the interstitial site. ZnO is highly antagonistic to chemical attack and has excellent adherence to many substrates. High transmittance in the visible region and reflective index (n_r = 1.7-2) enable it to act as an antireflection coating, light emitting devices [36], conductive electrode, and window layer in solar cells [37]. Furthermore, ZnO with wide band gap are transparent in the visible spectrum and serve as the channel layer of transparent thin-film transistors (TFTs) [38]. Even it can be apply in the nonvolatile memories such as resistive switching memory [39-41].

Group III elements such as Al^{3+}, Ga^{3+} and In^{3+} are used to improve/or change the electrical conductivity and the optical property of the ZnO films. These dopants play the rule of a donor to occupy a substitutional site for Zn^{2+} cation of higher valency, but it may occupy an interstitial site in the ZnO lattice and be a scattering center to decrease the electrical and optical property of the ZnO films. Besides, the size of the ionic radius of the impurity that has to be similar to the zinc ion that it substitutes in order to avoid lattice distortions. So, the efficiency of the dopant element that depends on its electro-negativity and the ionic radius is an important term to select the suitable dopants.

1.2 TCO deposition method

An extensively-variety of physical and chemical method such as reactive evaporation [43], DC/or RF magnetron sputtering [44,45], laser ablation [46], pulsed laser deposition (PLD) [47], molecular beam epitaxy (MBE) [48], metal organic chemical vapor deposition (MOCVD) [49], sol-gel [50,51], chemical spray pyrolysis [52-55] and atmospheric pressure plasma chemical vapor deposition (APPCVD), have been used in the deposition of highly conductive and transparent ZnO thin films on several substrates.

In the above mentioned deposition methods, we choose the APPCVD system to deposit our impurity doped zinc oxides that is due to the deposition way has a lot of merits, such as it could be manufacture in the air ambient, economical, easy-to-handle, large area deposition feasibility, and controlled quality [56,57].

Based on the plasma used methods to make high quality thin films [58], the APPCVD can be deposited TCO thin films in the atmosphere ambient, but the PECVD can not. And other plasma CVD processes for making thin films also use low-pressure conditions. The APPCVD system is mainly used in high temperature arc plasma, for example, the plasma jet used for diamond synthesis [59] and the inductively coupled plasma (ICP) flash evaporation process for producing ferrite films formation [60] is possible to generate atmospheric pressure cold glow plasma. The atmospheric pressure cold glow plasma which is used the nitrogen gas as a plasma gas, employed a high frequency power source over one kilohertz, and stetted an insulating between two electrodes [61].

From the viewpoint of the process cost, and particularly in the application of thin film deposition on ready prepare glass substrates, the APPCVD would be quite advantageous than other plasma enhanced CVD. By using the APPCVD system, numerous films were fabricated such as SiO_2 films [62], TiO_2 films [63] and ZnO films. We can choose the appropriate source material in the form of solution even mixing two or more solutions to be the film deposition precursor for an APPCVD process, it would be a convenient process for making a variety of thin films, even though TCO films.

1.3 Motivation

In this essay, we used the APPCVD system to deposit the ZnO based transparent conductive oxides (TCO), including aluminum doped zinc oxide (AZO), gallium doped zinc oxide (GZO) and indium doped zinc oxide (IZO). The three group-III elements are common used to dope the ZnO that could be occupied a substitutional site for Zn^{2+} cation of higher valency. The optical and electrical properties on Al^{3+}-, Ga^{3+}- and In^{3+}-ZnO films have been widely published with lots of physical and chemical deposition method. However, little information is known about the opto-electrical properties of above TCO thin films which are fabrication in the APPCVD system. So, we interested on the opto-electrical characteristics of the TCO films, and compared them in some of aspect. Post annealing treatments are frequently conducted to optimize the electrical and optical properties. The thermal budget for opto-electronic devices required serious considerations. As a result, studies on the thermal stability of TCO films are in demand. In modern years, the thermal stability of the indium tin oxide (ITO) film of their synthesized optoelectronic devices had been discussed. Zinc oxide film is a promising candidate for replacing the commercial ITO film. So, the thermal stability of ZnO is a worthy work to investigate.

Table 1-1 The basic properties of three in common used TCO films [42]

Material	In_2O_3	SnO_2	ZnO
Crystal structure	bixbyite	rutile	wurtz
Band gap (eV)	3.5 - 4.0	3.8 - 4.0	3.3 - 3.6
Main dopant	Sn^{4+}	F^{1+}, Sb^{5+}	Al^{3+}, Ga^{3+} , In^{3+}
Mobility ($cm^2/V\text{-}s$)	103	18 - 31	28 - 120
Carrier concentration (cm^{-3})	1.4×10^{21}	2.7×10^{20} - 1.2×10^{21}	1.1×10^{20} - 1.5×10^{21}
Resistivity (Ω-cm)	4.4×10^{-5}	7.5×10^{-5} – 7.5×10^{-4}	1.9×10^{-4} – 5.1×10^{-4}

Table 1-2 Application of TCO films [42]

Material	Application	Property
SnO_2:F	Low radiation building glasses at the frigid zone	Plasma wavelength～3um
Ag, TiN	Heat insulating glasses at the torrid zone	Plasma wavelength≦1um
SnO_2:F	Outer surface of solar cell	Thermal stability, low cost
ITO, SnO_2:F	Electrochromic windows	Chemical stability, High transparency, low cost
ITO	Electrodes of flat panel display	Easy to etching, low process temperature, low resistance
ITO, ZnO	Window layers of light emitting diode	High transparency, low resistance
ITO, Ag, Ag-Cu alloy	Defogger glasses	Low cost, good endurance, low resistance
SnO_2	Glasses of the toaster	Thermal stability at high temperature, chemical and mechanical endurance, low cost
ITO, SnO_2	Touch panels	Low cost, good endurance
Ag, ITO	Electromagnetism screening	Low resistance
Ag/ZnO	Concealed safety circuits of the display cabinets	Good endurance, UV protection

Chapter 2

Literature Review

2.1 Properties of ZnO

Most of the group II-VI binary compound semiconductors crystallize in either cubic zinc blende or hexagonal wurtzite structure where each anion is surrounded by four cations at the corners of a tetrahedron, and vice versa. This tetrahedral coordination is typical of sp^3 covalent bonding orbital, but these materials also have a substantial ionic character that tends to increase the band gap beyond the one expected from the covalent bonding. ZnO is an II-VI compound semiconductor which ionicity resides at the borderline between the covalent and ionic semiconductors.

The crystal structures composed by ZnO are wurtzite, zinc blende, and rocksalt. Under ambient conditions, the thermodynamically stable phase is the wurtzite symmetry. The zinc blende ZnO structure can be stabilized only by growth on cubic substrates, and the rocksalt structure may be obtained at relatively high pressures, as in the case of GaN.

The wurtzite structure has a hexagonal unit cell with two lattice parameters a and c in the ratio of $c/a = (8/3)^{1/2} = 1.633$. The structure is composed of two interpenetrating hexagonal close-packed sub-lattice, each of which consists of one type of atom displaced with respect to each other along the threefold c-axis by the amount of $u = 3/8 = 0.375$. The internal parameter u is defined as the length of the bond parallel to the c-axis divided by the c lattice parameter. The basal plane lattice parameter is always depicted by a; the axial lattice parameter, perpendicular to the basal plane, is described by c. Every sub-lattice includes four atoms per unit cell, and every atom of group II atom is surrounded by four atoms of the group VI atom, or vice versa, which are coordinated at the edges of a tetrahedron.

As in all solids, the atoms in a semiconductor at nonzero temperature are in unending motion, oscillating about their equilibrium states. Thermal expansion, specific heat, and pyroelectricity are among the standard material properties that define the linear relationships between mechanical, electrical, and thermal variables. These thermal properties and thermal conductivity depend on the ambient temperature, and the final temperature limit to study these effects is the melting temperature, which is about 1975K for ZnO.

As a direct and large band gap material, ZnO is attracting much attention for a variety of electronic and optoelectronic applications. Owing to the large energy band gap of ZnO, so it has lots of advantages such as high-temperature and high-power operation, lower noise generation, higher breakdown voltages, and ability to sustain large electric fields. The electron transport in semiconductors can be considered for low and high electric fields. At adequate low electric fields, the energy gated by the electrons from the applied electric field is small compared to the thermal energy of electrons and therefore the energy distribution of electrons is unaffected by such a low electric field. Because of the scattering rates calculating the electron mobility depend on the electron distribution function, electron mobility remains independent of the applied electric field, and ohmic law is obeyed. When the electric field is increased to a point where the energy gated by electrons from the external field is no longer negligible compared to the thermal energy of the electron, the electron distribution function changes momentously from its equilibrium value. These electrons become hot electrons characterized by an electron temperature larger than the lattice temperature.

2.2 Deposition methods of TCO films

The methods of deposition TCO films have distinct classification. In this paper, we categorize them in physical and chemical type that representing the source of the TCO films is solid and liquid. Following the exposition will discuss them in detail.

2.2.1 Magnetron sputtering

The sputtering method is working in the glow discharging region, which has higher energy and density of electrons. We put the substrate at anode and set the target at cathode in the Ar ambient, and then the cations which accelerated by the electrical field bombard the target. At this time, the TCO films atoms is leaved out of the target and going to the substrate to form the TCO films. The reason of the cations which is driving to target is the potential of plasma always higher than chamber, target and substrate. Moreover, target connect with cathode will increase the potential difference between plasma and target. If we set a magnet under the target, there were an external magnetic filed to increase the plasma density, so the cations which bombard the target will increase simultaneously. When the low conductivity materials or insulators were to be the deposition substrate, it is difficult to discharge with the DC power. So, we have to use the RF power which the frequency needs to reach the grade of megahertz (usually 13.56MHz) to be the power supply. Using the self bias phenomenon in the RF discharge, it can make the target potential will always in negative values to ensure the bombardment will almost continuously which is same capability as the DC discharge.

So far, the sputtering technique is the most common in deposition the TCO films, including electrodes of flat display and energy efficiency windows. The generally properties of sputtering are described following:

(1) Widely scope of the process films such as metal, alloy and insulator.
(2) The films thickness can control by the apply power and process times.
(3) The stable, uniform and large area films can be obtained.
(4) Because of higher bombardment energy, so it can deposit the excellent adhesion and crystallization films.
(5) Long target lifetime, so it can operate at continuous and automatic long time process.

There is another magnetron sputtering method which getting high density plasma by RF-DC couple manner. In general RF magnetron sputtering, the self bias of the target can change with the RF frequency and power, and it controls the ion energy of bombarding to the target. When the RF frequency increased, the self bias of the target will decreased, the RF power increased, the self bias of the target will also increased. However, in the RF-DC couple magnetron sputtering system, the RF power is mainly to generate high density plasma, and the DC power is to adjust the electric potential of the target, by doing that is easy to control the deposition conditions.

2.2.2 Vacuum evaporation

Vacuum evaporation is a method which evaporating the metal or metal oxide source in the 10^{-3}~10^{-2}Pa pressure, and then deposited on the heating substrate. The ways of evaporating the source material involved resistively heated, electron beam heated and ratio frequency (RF) heated. Among them, the resistively heated is common used under 1500^{0}C, its source is putted in the boat or basket and using the resistance to heat. Inversely, the regularly used above 1500^{0}C is the electron beam heated method which is putted the source materials in the crucible and then heated them by electron beam direct illuminating, electron bean focusing illuminating, electron beam crooked focusing illuminating and electron beam crooked de-focusing illuminating.

In contrast with the magnetron sputtering, the kinetic energy of the deposited film atoms is lower than the sputtering method even at the highest temperature region, so it needs to more substrate temperature. But this property may not a disadvantage surely. For example, when deposition the window layer of LED which is deposited on the finished epitaxial layer, if we use the sputtering method to deposit this film, the high energy particles may be destroyed the epitaxial layer, so the vacuum evaporation method is more convenient in this case.

In order to improve the low reaction ability of the vacuum evaporation method, researchers invent a method which is generating high density plasma between the source and substrate to activate the source material and oxygen called activated reactive evaporation (ARE). The generation of high density plasma nearby the substrate is putted a RF coil or a tungsten filament by the side of substrate and applying current to activate it to release hot electrons, letting them to move to the anode side by biasing voltage. Besides, we can enhance the reaction by installing a magnetron coil to hamper the plasma.

The familiar properties of activated reactive evaporation are expounded below:

(1) Extremely high deposition rates, variety of coating compositions.

(2) Precise control of stoichometry.

(3) Better adhesion.

(4) Denser microstructure than direct evaporation.

(5) High substrate temperature.

(6) Addition of an extra electrode, slightly complicated compared to evaporation.

(7) Substrate must generally be rotated for uniform coating.

2.2.3 Pulsed laser deposition

Pulsed laser deposition is a technology where a high energy density focusing pulsed laser beam is struck a target of the material that is to be deposited. The target is vaporized which deposits it as a thin film on substrate. This method can be applied on many materials, so it can deposit lots of thin films. But the growth rate of PLD is extremely slow; therefore, it is not a mass production technology. This process can occur in ultra high vacuum or in the presence of a ambient gas, such as oxygen which is commonly used when depositing oxides to fully oxygenate the deposited films.

The PLD basic machinery is simple relative to many other deposition techniques, the physical phenomena between laser and target interaction and the film growth are quite complex. When the laser pulse is absorbed by the target, the absorption energy is converted to electronic excitation and thermal energy resulting in evaporation and plasma formation. The ejected varieties full of the surrounding vacuum including atoms, molecules, electrons, ions, clusters, particulates and molten globules, before depositing on the typically hot substrate.

There are a number of advantages of PLD over other thin film deposition methods, these include:

(1) The largest advantage is that it is versatile. This method can be applied on many thin films including metal, oxides, semiconductors and even polymer. It is unlike MBE and CVD, where different source of precursors are required for each element of the desired compound.

(2) It can be maintained the target composition in the deposited thin films. Because of the very short duration and high energy of the laser pulse, target material immediately toward the substrate, every component of the phase has an analogous deposition rate, so the thin films composition is almost unchanged.

(3) The energy associated with the high ionic content in laser ablation plumes and high particle velocities appear to aid crystal growth and lower the substrate temperature required for epitaxy.

(4) PLD is clean, low cost and capable of producing simply by switching several different targets.

There are also a heaps of advantages of PLD, these include:

(1) PLD brings difficulty to controlling thickness uniformity across the sample, but this problem can be overcome, to some extent, by scanning the laser beam on a larger size target.

(2) The plume of ablated material is highly forward directed, which causes poor conformal step coverage. It also makes thickness monitoring difficult.

(3) There is an intrinsic splashing associated with laser ablation itself, which produces droplets or big particles of the target material on the substrate surface. From an industrial perspective, this is particularly serious as it will result in device failure

2.2.4 Spray pyrolysis

Deposition TCO thin films by the pyrolysis method has been used for a long time. The deposition material can use solid or liquid source, according to our previous statement of the definition of the deposition method, it may be categorized to the physical type, but it is similar to the CVD method, so we still categorizing it in chemical manner.

Spray pyrolysis is the most in common uses in the pyrolysis manners. In spray pyrolysis, the precursor solution is pulverized as affine mist via a spray nozzle and a carrier gas at high pressure. The so produced mist condenses on a preheated substrate, and is instantly pyrolysed (spray pyrolysis). The process can be conducted in one or more pulses to obtain uniform films. Spray pyrolysis is suitable for substrate with complex geometry, and can be used for a variety of oxide materials. Although the first impression of spray pyrolysis is simple to do, but it concerns at least seven parameters, including heater temperature, carrier gas flow rate, gap distance, solution drop size, solution component, solution flow rate and substrate velocity through the heater

When the solution drops leave from nozzle to the substrate, occurs different reaction with increasing the substrate temperature. From Figure 2-6, in process A, the solution drop sprinkled on the substrate, vaporizes, then leaves a dry precipitate in which decomposition occurs; in process B, the solvent evaporates before the solution drop arrives at the surface and the precipitate bombards upon the surface where decomposition occurs; in process C, the solvent vaporizes as the solution drop accesses the substrate, then the solid melts and vaporizes, its vapor diffuses to the substrate to undergo a heterogeneous reaction there; in process D, at the hugest temperatures, the metallic compound vaporizes before it arrives the substrate and the chemical reaction takes place in the vapor phase.

Apparently, we hope not to happen to the process A and D, because it will cause rough and viscosity thin films. So, select the appropriate substrate temperature and make the uniform and equal size of droplet will help the reaction perfectly.

The advantages of spray pyrolysis are summarized below:

(1) The spray pyrolysis can be easy and cheap.

(2) Substrate with complex geometries can be coated.

(3) Leads to uniform and high quality coatings.

(4) Low crystallization temperatures.

(5) Porosity can be easily tailored.

2.2.5 Dip coating

Dip coating is a conventional way of deposition thin films for research purpose. Uniform films can be applied onto planar substrate. For industrial processes, spin coating is used more often. Dip coating is putted the substrate in the deposition solution first, and then pull up the substrate in a regular speed, after that the successful thin film will obtained by drying and annealing. This deposition thin film way is one of the most common used in sol-gel method.

There are a lot of properties of dip coating manner:

(1) It can be deposited on the irregular surface or double-faced substrate.

(2) Few nanometers of thin films can be acquired.

(3) Simple operation, but usually unstable.

(4) Unfit to high viscosity fluid.

(5) The edge of substrate will gathered deposition solution to cause un-uniform films.

The dip coating process can be separated into five procedures:

(1) The substrate is immersed in the solution of the coating material at a constant speed.

(2) The substrate has remained inside the solution for a while and is started to been pulled up.

(3) The thin layer deposits itself on the substrate while it is pulled up. The withdrawing is carried out at a constant speed to avoid any vibration. The speed determines the thickness of the coating layer.

(4) Excess fluid will drain from the substrate surface.

(5) The solvent evaporates from the fluid, forming the thin film. For volatile solvents, such as alcohols, evaporation starts already during the deposition and drainage steps.

2.2.6 Atomic layer deposition (ALD)

Atomic layer deposition (ALD) also called atomic layer epitaxy (ALE) or chemical beam deposition where is reacted on the thin film surface. The reaction can be categorized to two chemical reactions, A and B. The product of reaction A is the reactant of reaction B, and vice versa. Therefore, if only introduce the precursor gases each other, deposition reaction will proceeding alternate continually in ABAB… form. ALD is a method of applying thin films such as compounds and elements to various substrates with atomic scale precision. Similar in chemistry to chemical vapor deposition (CVD), except that the ALD reaction breaks the CVD reaction into two half-reactions, keeping the precursor materials separate during the reaction. ALD film growth is self-limited and based on surface reactions, which makes achieving atomic scale deposition control possible. By keeping the precursors separate throughout the coating process, atomic layer thickness control of film grown can be obtained as fine as atomic/molecular scale per monolayer.

The two reactions of ALD is reacted between gas phase molecule precursor and surface functional group, it can simply express below:

Reaction A: $A^* + P_A \rightarrow F_A + B^* + V_A(\uparrow)$ (Eq. 2-1)

Reaction B: $B^* + P_B \rightarrow F_B + A^* + V_B(\uparrow)$ (Eq. 2-2)

In above expression, * is the functional group, P the precursor, F the composition of thin films and V the volatile molecules. Introduce P_A in the chamber will occur reaction A, formation a new layer F_A, functional group B* and volatile molecule V_A; V_A pump out by the vacuum system, and B* is the demand functional group of reaction B. Reaction A will proceeding continually until the substrate surface cover the F_A and B* absolutely. After reaction A, it wills not reacting continually if there are surplus P_A, so ALD film growth is self-limited. Due to the characteristics of self-limiting and surface reactions, ALD film growth makes atomic scale deposition control possible. By keeping the precursors separate throughout the coating process, atomic layer control of film growth can be obtained as fine as ~0.1 Å per monolayer. Separation of the precursors is accomplished by pulse purge gas (typically nitrogen or argon) after each precursor pulse to remove excess precursor from the process chamber and prevent parasitic CVD deposition on the substrate. Besides, compare with CVD, ALD can grow thin films at lower temperature phenomenon.

There are many merits of ALD:

(1) Film thickness depends only on the number of reaction cycles, which makes the thickness control accurate and simple.

(2) Unlike CVD, there is less need of reactant flux homogeneity, which gives large area capability, excellent conformality and reproducibility, and simplifies the use of solid precursors.

(3) Relatively insensitive to dust (films grows underneath dust particles).

(4) The growth of different multilayer structures is straight forward.

(5) Its process has the following properties, wide range of film materials available, high density and low impurity level. Also, lower deposition temperature can be used in order not to affect sensitive substrates.

But, there are also some limitations of ALD:

(1) The major limitation of ALD is its slowness; usually only a fraction of a monolayer is deposited in one cycle.

(2) Although the selection of film materials grown by ALD is wide, but many technologically important materials such as Si, Ge and Si_3N_4, cannot currently be deposited by ALD in a cost-effective way.

(3) ALD is a chemical technique and thus there is always a risk of residues being left from the precursors. The impurity content of the films depends on the completeness of the reactions. In typical oxide processes where metal halides of alkyl compounds are used together with water as precursors, impurities found in the films are at the 0.1-1 atom % level.

2.2.7 Chemical vapor deposition

Chemical vapor deposition (CVD) is a deposition manner where chemical precursors are transited in the vapor phase to decompose on a heated substrate to form a film. The films may be polycrystalline, amorphous or epitaxial depending on the source materials and reactor conditions. CVD has become the major method of film deposition for the semiconductor industry due to its high throughput, high purity, and low cost of operation. CVD is also commonly used in optoelectronics applications, optical coatings and coatings of wear resistant parts.

CVD has many advantages over physical vapor deposition (PVD) processes such as molecular beam evaporation and sputtering. Firstly, the pressures used in CVD allow coating of three dimensional structures with large aspect ratios. Since evaporation processes are very directional, PVD processes are typically line of sight depositions that may not give complete coverage due to shadowing from tall structures. Secondly, high precursor flow rates in CVD give deposition rates several times higher than PVD. Also, the CVD reactor is relatively simple and can be scaled to fit several substrates. Ultra-high vacuum is not needed for CVD and changes or additions of precursors are an easy work. Furthermore, varying evaporation rates make stoichiometry hard to control in physical deposition. While for CVD stoichiometry is more easily controlled by monitoring flow rates of precursors. Other advantages of CVD include growth of high purity films and the ability to fabricate abrupt junctions.

However, some disadvantages of CVD that make PVD more attractive for some applications. High deposition temperatures for some CVD processes (usually higher than 600^0C) are often unsuitable for structures already fabricated on substrates. Although with some materials, use of plasma-enhanced CVD or metal-organic precursors may reduce deposition temperatures. Another disadvantage is that CVD precursors are often dangerous or poisonous and the by-products of these precursors may also be noxious. Therefore extra steps have to be taken in the managing of the precursors and in the treatment of the reactor exhaust. Also, many precursors for CVD, especially the metal-organics, are relatively expensive. Finally, the CVD process contains a large number of parameters that must be accurately and reproducibly optimized to produce good films.

A regular CVD process includes complex flow kinetics since gases are flowing into the reactor, reacting on the substrate surface, and then by-products are drained out of the reactor. The sequence of circumstances during a CVD reaction is shown in Figure 2-10 and as follows:

(1) Precursor gases introduce into the chamber by pressurized gas lines.

(2) Mass transit of precursors from the main flow regime to the substrate surface through the boundary layer.

(3) Absorption of precursors on the substrate surface and the substrate is heated simultaneously.

(4) Chemical reaction on the substrate surface.

(5) The atoms of formation of thin films diffuse on the substrate surface to growth places.

(6) Desorption of by-products of the reactions.

(7) Mass transit of by-products to the main flow regime.

Gas flow in a CVD reactor is generally laminar, although in some cases heating of the chamber walls will create convection currents. The complete problem of gas flow through the system is very complex. Assuming we have laminar flow the gas velocity at the chamber walls will be zero. Between the wall and the bulk gas velocity there is a boundary layer. The boundary layer thickness increases with lowered gas velocity and the distance from the tube inlet. Reactant gases flowing in the bulk must diffuse through the boundary layer to reach the substrate surface. Often, the susceptor is tilted to partially compensate for the increasing boundary-layer thickness and concentration profile.

During CVD, the deposition rate of the film is limited by either surface reaction kinetics, mass transport of precursors to the substrate surface, or the feed rate of the precursors. Surface reaction controls the rate when deposition occurs at low temperatures where the reaction occurs slowly and also governs at low pressures where the boundary layer is thin and reactants easily diffuse to the surface. Since reactants easily diffuse through the boundary layer, the amount of reactant at the substrate surface is independent of reactor pressure. Therefore, it is the reactions and motions of the precursors absorbed on the surface which will calculate the overall deposition rate of the film. A symbol of surface reaction limited growth would be dependence of the deposition rate on substrate orientation, since the orientation would surely not affect the thermodynamics or mass transit of the system.

A deposition limited by mass transit is controlled by the diffusion of reactants through the boundary layer and diffusion of by-products out of the boundary layer. Mass transit limits reactions when the temperature and pressure are high. These conditions increase the thickness of the boundary layer and make it harder for gases to diffuse out. In addition, decomposition of the reactants is typically quicker since the substrate is at a higher temperature. When mass transit limits the growth, either increasing the gas velocity or rotating the substrate during growth will decrease the boundary layer and increase the growth rate.

2.3 Atmospheric-pressure plasma system

2.3.1 Corona discharge

A corona is a process by which a current develops between two high-potential electrodes in air, by ionizing that fluid to create a plasma around one electrode, and by using the ions generated in plasma processes as the charge carriers to the other electrode.

Corona discharge usually involves two asymmetric electrodes, one highly curved such as the tip of a needle or a narrow wire, and another one of low curvature such as a plate or the ground. The high curvature assures a high potential gradient around one electrode, for the generation of the plasma.

Coronas may be positive, or negative. This is calculated by the polarity of the voltage on the high curvature electrode. If the curved electrode is positive associated to the flat electrode, it will have a positive corona, and vice visa. The physics of positive and negative coronas are obviously different. This asymmetry structure is a result of the great difference in mass between electrons and positively charged ions, and so only the electron having the ability to undergo a significant degree of ionizing inelastic collision at common temperatures and pressures.

2.3.2 Dielectric barrier discharge (DBD)

Dielectric barrier discharges involve a specific class of high voltage, ac, gaseous discharges that typically operate in the near atmospheric pressure range. Their defining feature is the presence of dielectric layers that make it impossible for charges generated in the gas to reach the conducting electrode surfaces. With each half cycle of the driving oscillation, the voltage applied across the gas exceeds that required for breakdown, and the formation of narrow discharge filaments initiates the conduction of electrons toward the more positive electrode. As charge accumulates on the dielectric layer at the end of each filament, the voltage drop across the filament is reduced until it falls below the discharge sustaining level, therefore the discharge is quenched. The low charge mobility on the dielectric not only contributes to this self arresting of filaments but also limits the lateral region over which the gap voltage is diminished, thereby allowing parallel filaments to form in close proximity to one another. Thus, the entire gas filled space between parallel electrodes can become, on average, uniformly covered by transient discharge filaments, each roughly 0.1mm in diameter and lasting only about 10ns.

The DBD’s unique combination of non-equilibrium and quasi-continuous behavior has provided the basis for a broad range of applications and fundamental studies. Its use in industrial ozone reactors has generated interest in optimizing conditions for specific chemical reactions. To this end, experimental DBD studies have explored different gas mixtures, electrical characteristics, and geometries. Related work has focused on maximizing the ultraviolet radiation from excimer molecules produced in DBD’s. Several researchers have modeled single filament dynamics in order to account for the many reactions involving electrons, ions, neutral atoms, and photons. These efforts have been moderately successful in explaining and predicting the chemical and radiative properties of various DBD systems. On another research effort, it has been seen that the transverse spatial distribution of discharge filaments in

2D, parallel plate DBD's can take the form of stable, large-scale patterns reminiscent of those associated with magnetic domains. These patterns have been modeled with some success using methods that apply generally to pattern formation in nonlinear dynamical systems. Thus, the dynamical interactions between filaments, as well as the chemical and electronic interactions within filaments have proven interesting.

2.3.3 Atmospheric pressure plasma jet

Atmospheric pressure plasma jet is a non-thermal glow discharge plasma where operating at atmospheric pressure. The non-thermal plasma generates highly reactive ions, electrons and free radicals. The reactive species are directed onto a surface where the desired chemistry occurs. The electrons are quite hot, however the overall gas temperature remains quite cold, typically 50-300°C.

2.3.4 Arc Plasma

A plasma arc operates on principles similar to an arc-welding machine, where an electrical arc is struck between two electrodes. The high energy arc creates high temperatures ranging from 3000°C to 7000 °C. The plasma is highly ionized gas which is enclosed in a chamber. Waste material is fed into the chamber and the intense heat of the plasma breaks down organic molecules into their elemental atoms. In a carefully controlled process, these atoms recombine into harmless gases such as carbon dioxide. Solids such as glass and metals are melted to form materials, similar to hardened lava, in which toxic metals are encapsulated. With plasma arc technology there is no burning or incineration and no formation of ash. There are two main types of plasma arc processes: plasma arc melter and plasma torch.

Plasma arc melters have very high destruction efficiency. They are very robust; they can treat any waste with minimal or no pretreatment; and they produce a stable waste form. The arc melter uses carbon electrodes to strike an arc in a bath of molten slag. The consumable carbon electrodes are continuously inserted into the chamber, eliminating the need to shut down for electrode replacement or maintenance. The high temperatures produced by the arc convert the organic waste into light organics and primary elements.

Combustible gas is cleaned in the off-gas system and oxidized to CO_2 and H_2O in ceramic bed oxidizers. The potential for air pollution is low due to the use of electrical heating in the absence of free oxygen. The inorganic portion of the waste is retained in a stable, leach-resistant slag.

In plasma torch systems, an arc is struck between a copper electrode and either a bath of molten slag or another electrode of opposite polarity. As with plasma arc systems, plasma torch systems have very high destruction efficiency; they are very robust; and they can treat any waste or medium with minimal or no pre-treatment. The inorganic portion of the waste is retained in a stable, leach-resistant slag. The air pollution control system is larger than for the plasma arc system, due to the need to stabilize torch gas.

Table 2-1 Comparison of ALD and CVD

ALD	CVD
Highly reactive precursors	Less reactive precursors
Precursors react separately on the substrate	Precursors react at the same time on the substrate
Precursors must not decompose at process temperature	Precursors can decompose at process temperature
Uniformity ensured by the saturation mechanism	Uniformity requires uniform flux of reactant and temperature
Thickness control by counting the number of reaction cycles	Thickness control by precise process control and monitoring
Surplus precursor dosing acceptable	Precursor dosing important

Table 2-2 Thin film deposition methods compared

Method	ALD	MBE	CVD	Sputter	Evaporation	PLD
Thickness uniformity	good	fair	good	good	fair	fair
Film density	good	good	good	good	poor	good
Step coverage	good	poor	varies	poor	poor	poor
Interface quality	good	good	varies	poor	good	varies
Number of materials	fair	good	poor	good	fair	poor
Low temperature deposition	good	good	varies	good	good	good
Deposition rate	fair	poor	good	good	good	good
Industrial applicability	good	fair	good	good	good	poor

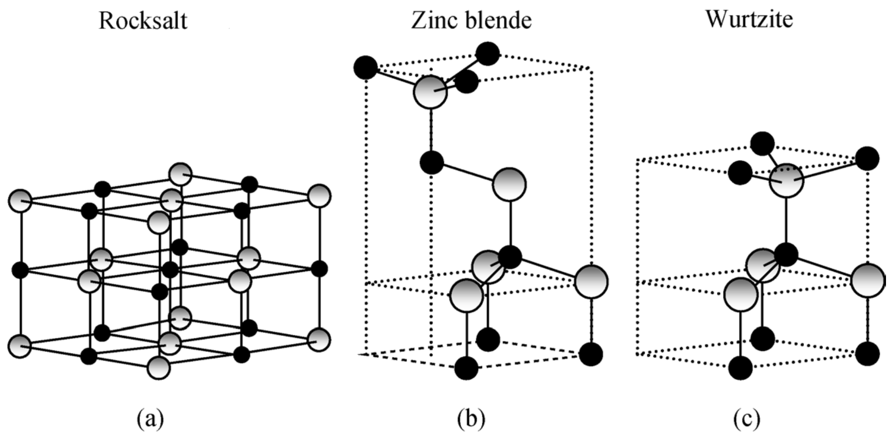

Figure 2-1 ZnO crystal structures: (a) cubic rocksalt (b) cubic zinc blende (c) hexagonal wurzite. Shaded gray and black spheres denote Zn and O atoms, respectively [64-66].

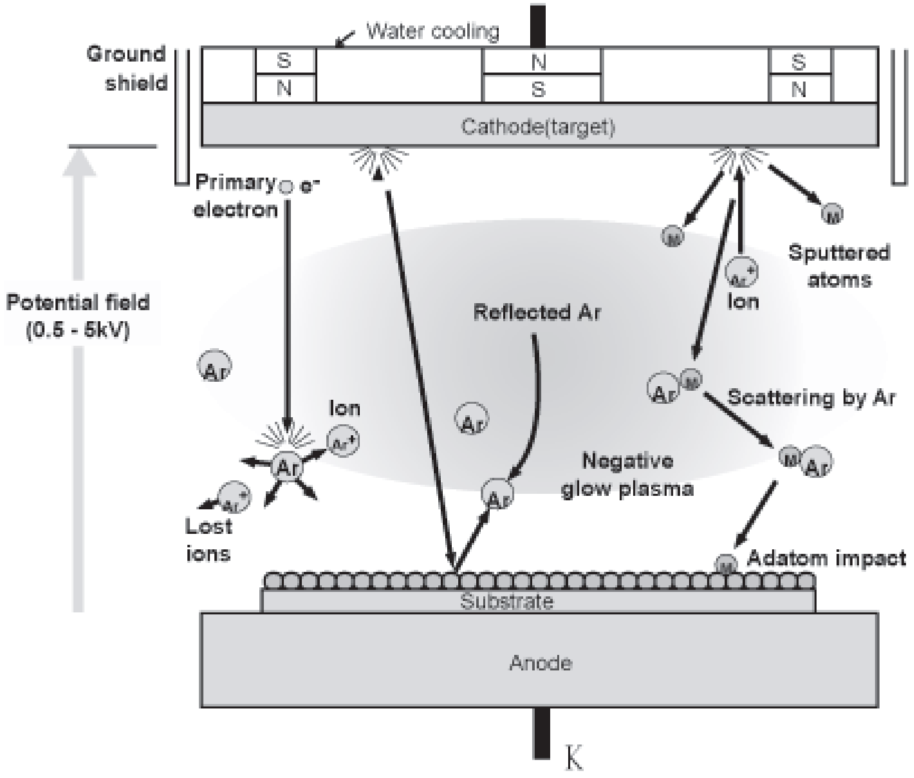

Figure 2-2 Schematic illustration of magnetron sputtering [67].

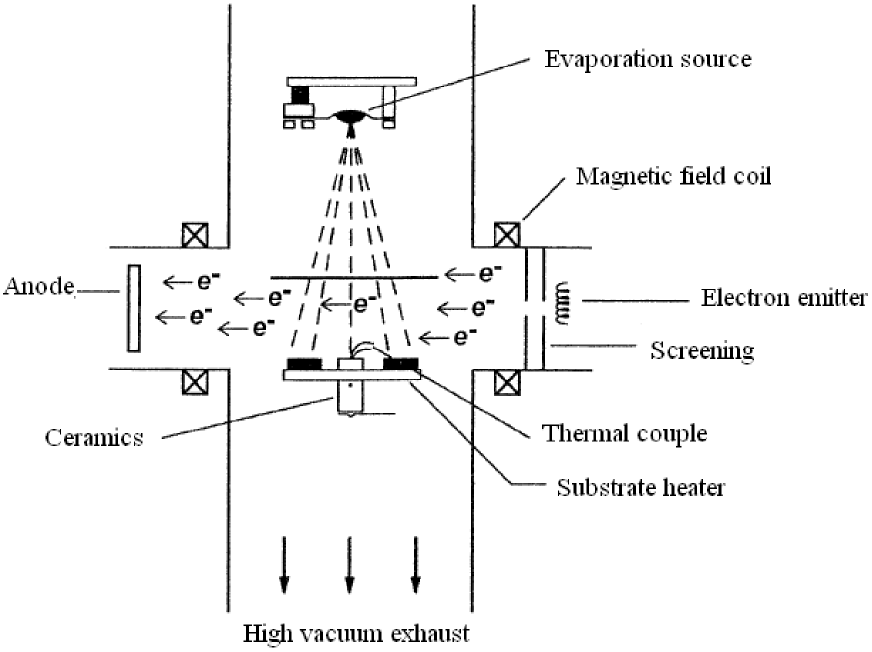

Figure 2-3 Schematic illustration of ARE which is used the hot electron emitter [68].

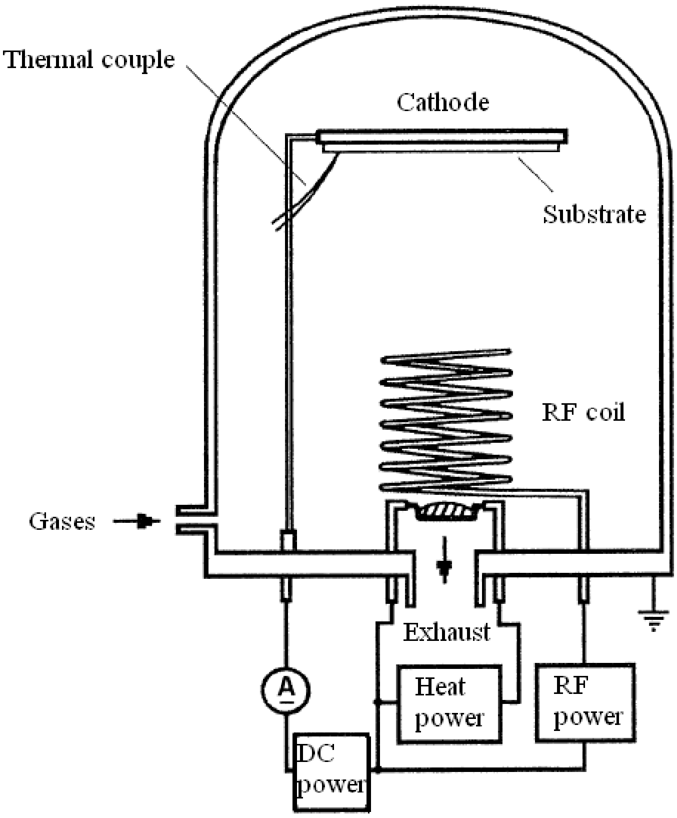

Figure 2-4 Schematic illustration of ARE which is used the RF discharge [69].

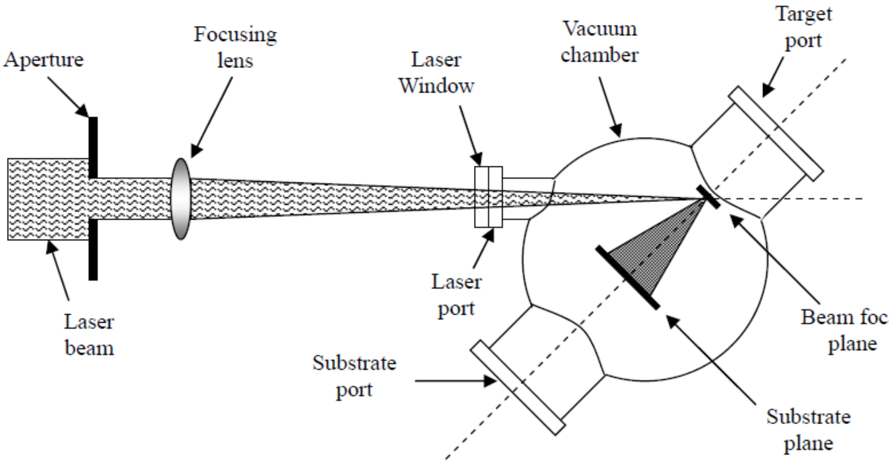

Figure 2-5 Schematic illustration of a Pulsed laser deposition system [70].

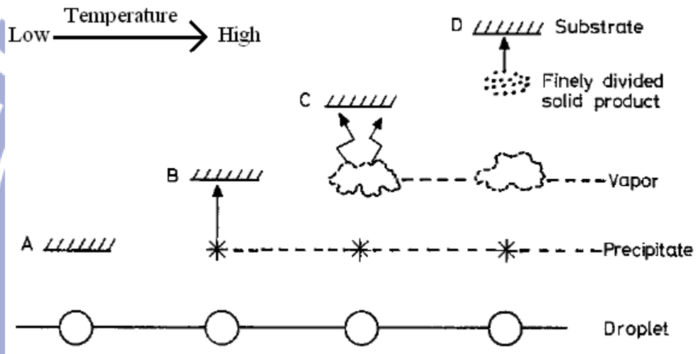

Figure 2-6 Description of the deposition process with raising the substrate temperature [71].

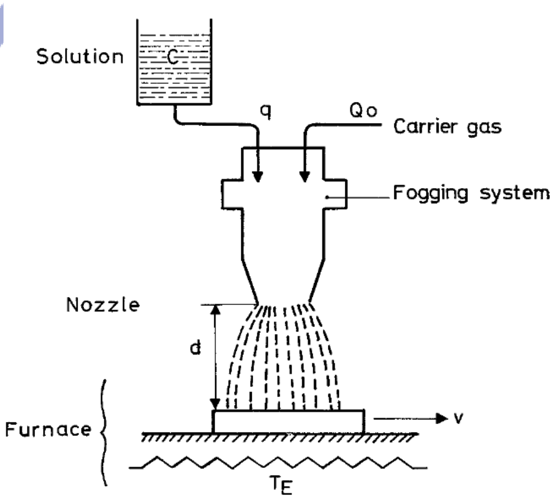

Figure 2-7 Schematic illustration of equipment for spray pyrolysis deposition [71].

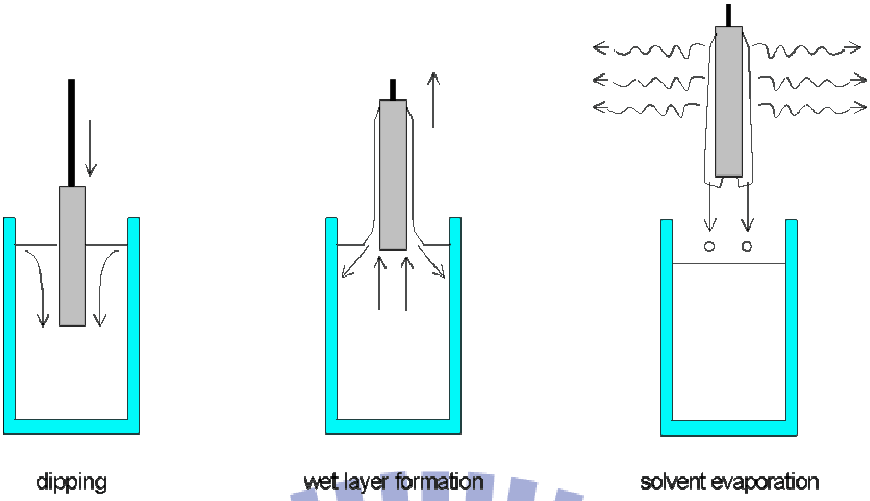

Figure 2-8 Steps of the dip coating process: dipping of the substrate into the coating solution, wet layer formation by withdrawing the substrate and gelation of the layer by solvent evaporation [72].

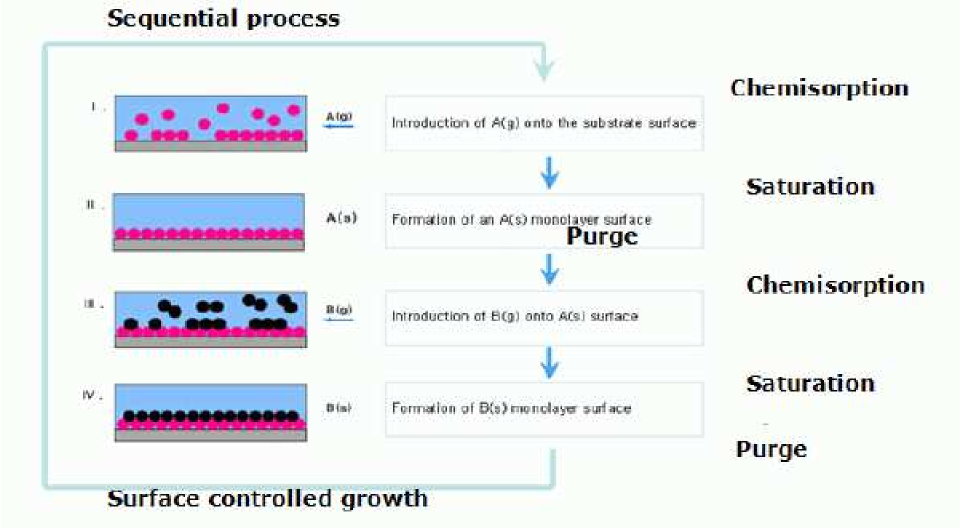

Figure 2-9 Schematic illustration of principle for ALD [73].

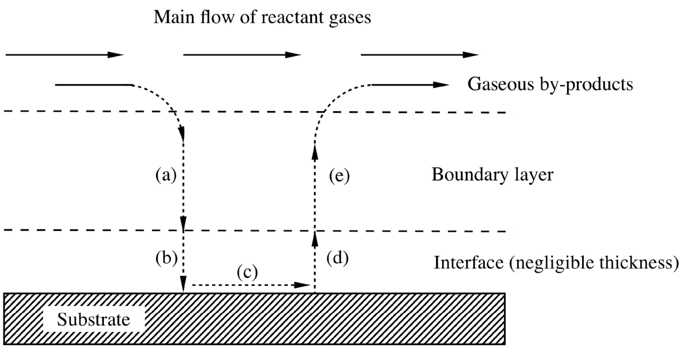

Figure 2-10 Sequence of events during CVD: (a) diffusion of reactants through boundary layer, (b) absorption of reactants on substrate surface, (c) chemical reaction takes place, (d) desorption of absorbed species, and (e) diffusion out of by-products through boundary layer [74].

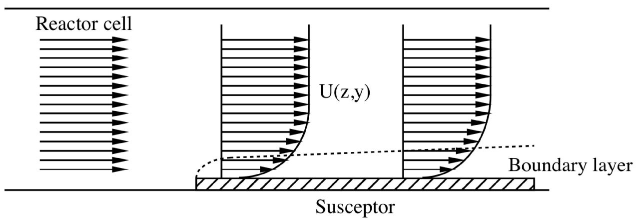

Figure 2-11 Development of boundary layer in a horizontal reactor [75].

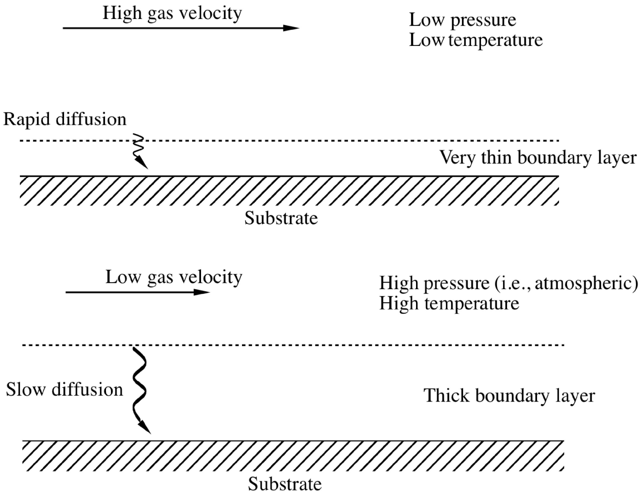

Figure 2-12 Surface reaction and mass transit limited growth in CVD [74].

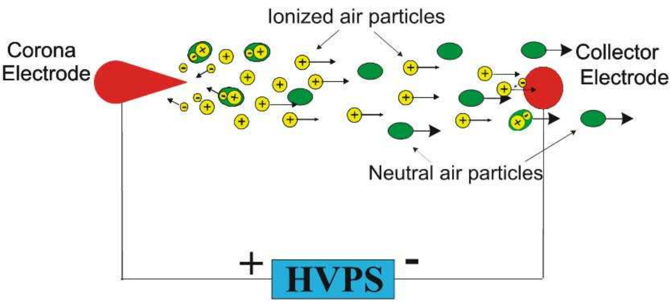

Figure 2-13 Schematic the principle of corona discharge [77].

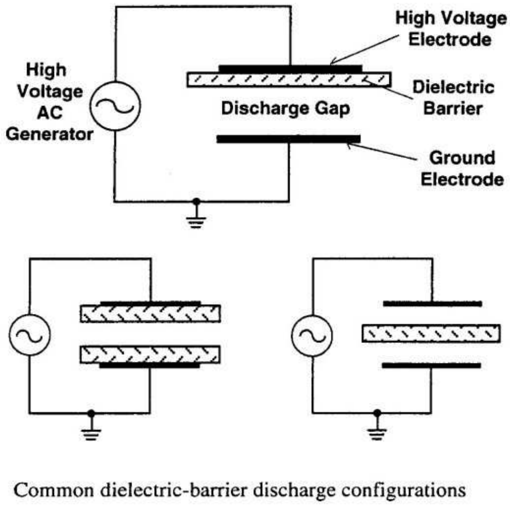

Figure 2-14 Schematic illustration of the DBD configurations [78].

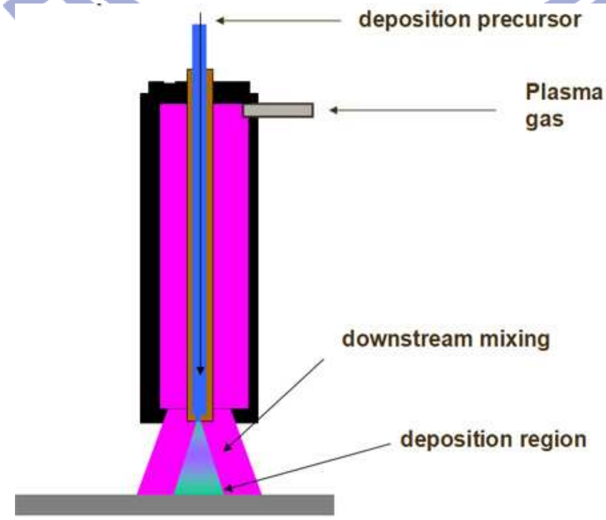

Figure 2-15 Schematic illustration of the AP plasma jet structures [79].

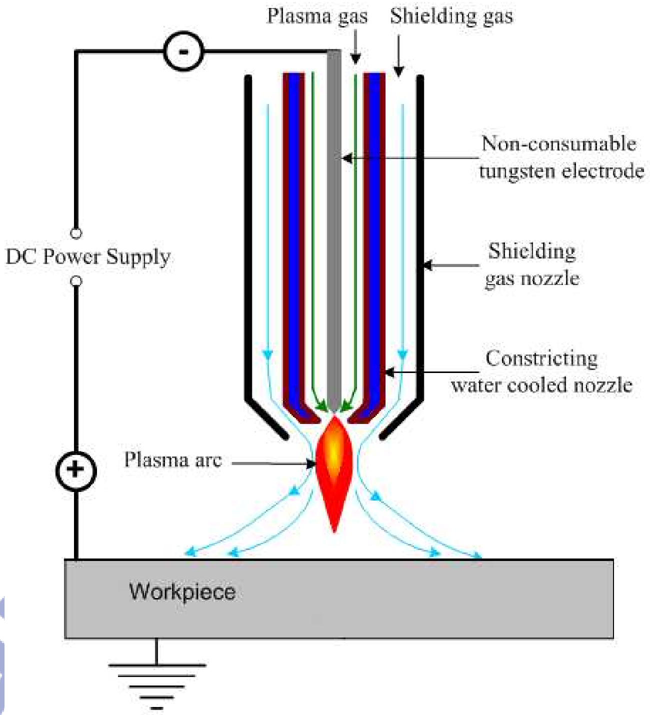

Figure 2-16 Schematic illustration of the arc plasma [80].

Table 2-3 Density of charge species in the plasma discharge [81].

Source	Plasma density (cm^{-3})
Low pressure discharge	10^{8}-10^{13}
Arc and plasma torch	10^{16}-10^{19}
Corona discharge	10^{9}-10^{13}
Dielectric barrier discharge	10^{12}-10^{15}
Capacitive discharge	10^{11}-10^{12}

Chapter 3

Experiments

3.1 Experimental procedures

3.1.1 Transparent conductive oxide thin films investigation procedures

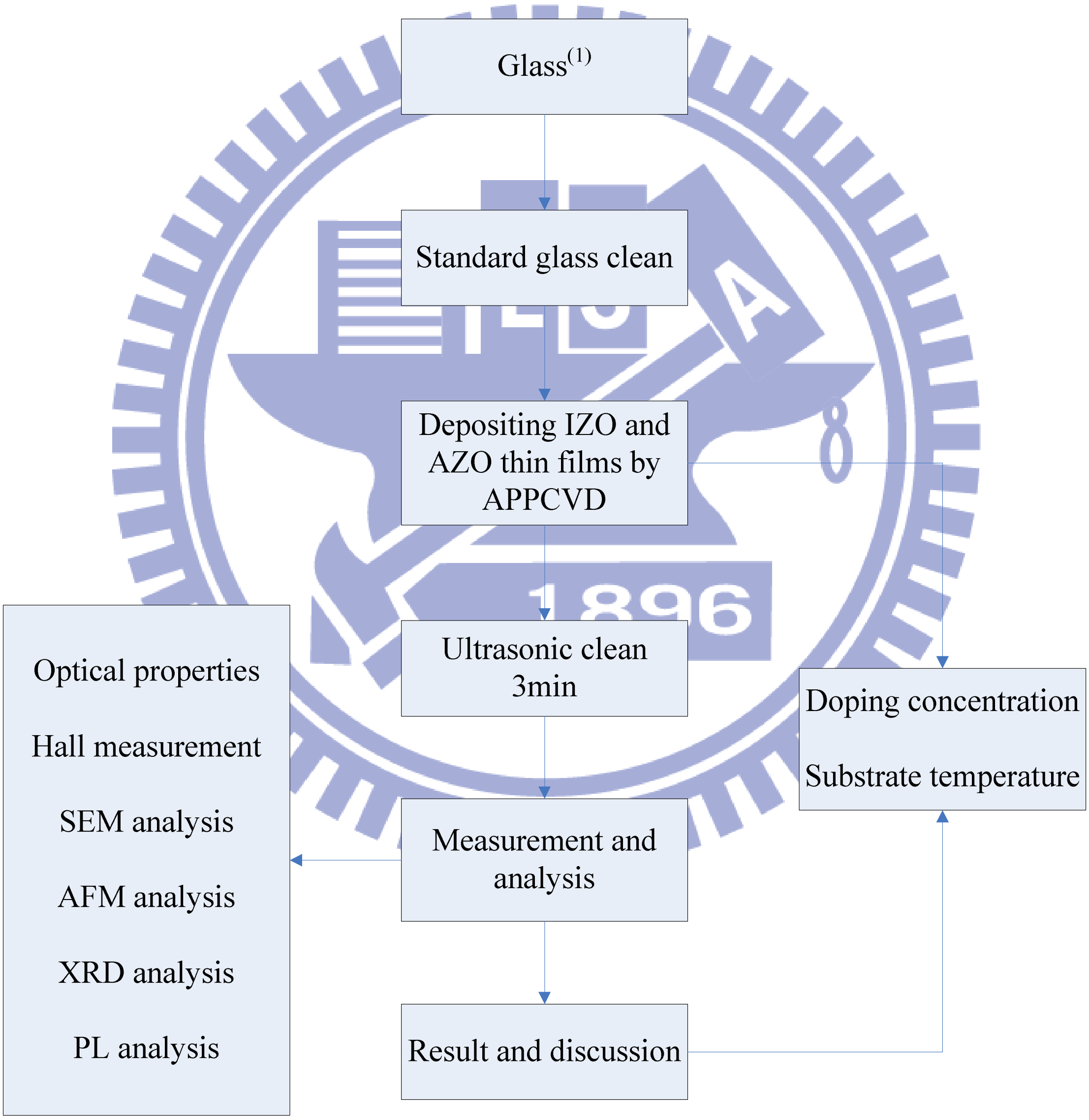

Figure 3-1 Schematic illustration of TCO thin films investigation.

3.1.2 Thermal stability investigation of TCO thin films procedure

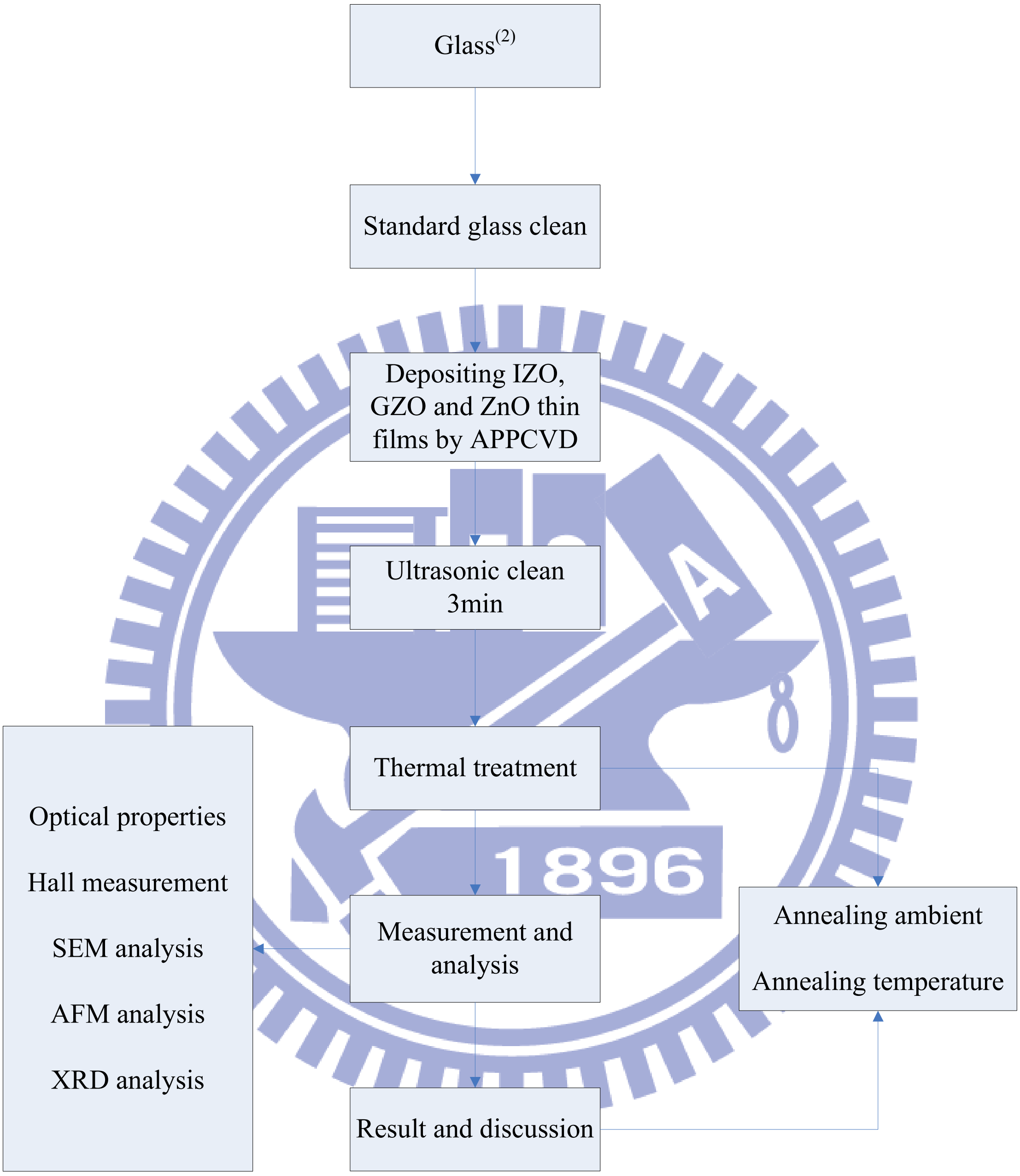

Figure 3-2 Schematic illustration of thermal stability investigation of TCO thin films.

3.1.3 Standard glass clean procedure

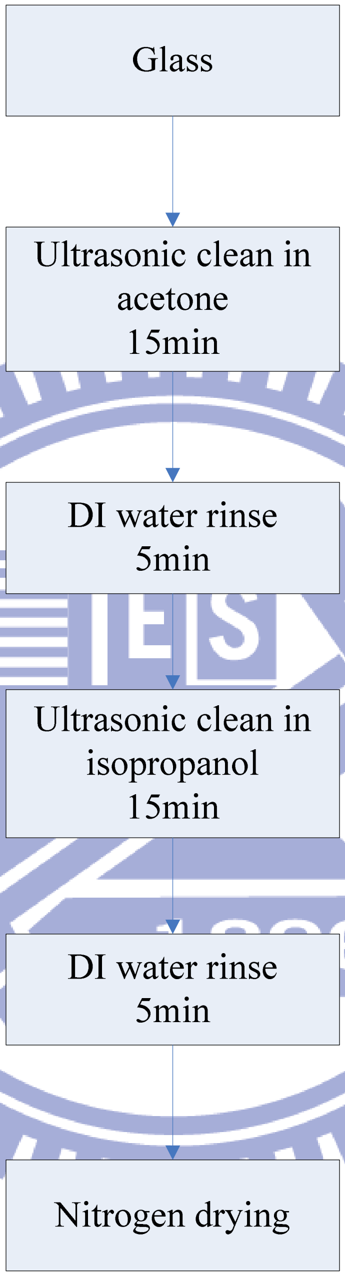

Figure 3-3 Schematic illustration of standard glass clean procedure.

Note: (1) The type of glass is FL (normal float) which is not heat-resistant glass.

(2) The type of glass is AN100 which is heat-resistant glass for the following high temperature treatment.

Table 3-1 Composition and characteristics of FL glasses

			FL glasses
Composition	SiO_2	[wt%]	70~73
	Al_2O_3	[wt%]	1.7~1.9
	RO (CaO + MgO)	[wt%]	11.5~13.0
	R_2O (Na_2O + K_2O)	[wt%]	13.0~14.0
	Fe_2O_3	[wt%]	0.05~0.15
Softening Point		[°C]	720~730
Annealing Point		[°C]	≒550
Strain Point		[°C]	≒510
Specific Gravity			≒2.5
Coefficient of linear expansion		[$\times10^{-6}$/°C (K)]	8.5~9.0
Mohs' hardness			≒6.5
Young's Modulus		[MPa]	≒7.16×10^{4}
Poisson's Ratio			≒0.23
Refractive index		(at 589.3nm)	≒1.52
Reflectivity		[%]	≒4
Water resistance		[mg]	≦0.5
Transmittance at 5mm		[%]	≧88

Table 3-2 Characteristics of AN100 glasses

	AN100
Density (g/cm^3)	2.51
Thermal shrinkage (ppm)	8
Strain point (^{o}C)	About 670
Young's modulus (kg/mm^2)	7900

3.2 Experimental equipments and parameters

The AZO, GZO and IZO films are deposited by the APPCVD systems as shown in Figure 3-4. First, we prepare the glasses which the area is 5mm×5mm, then purge it with standard clean process and segment them into the area of 2.5mm×2.5mm. Second, the films precursors are prepared by 1M $Zn(NO_3)_2$ and 0.1M $A(NO_3)_2$ ("A" represents the Al, Ga and In) which are mixed by atomic percentage. Next, we put them in a bottle with an ultrasonic which its frequency is 2.45MHz and used as the precursors to deposit thin films. Third, we apply nitrogen as the carrier gas and main gas to deliver the precursors into the inner nozzle and convey the reactants to the substrate surface with spiral airstream which is decomposed by arc plasma.

The APPCVD systems have lots of parameters including dopant concentration, substrate temperature, gap distance, scan times, power, carrier gas flow rate, main gas flow rate, different carrier gas kinds and $Zn(NO_3)_2$ concentration. All the parameters are shown in Table 3-2. Among above parameters, we choose the dopant concentration and substrate temperature to be the main topic of our research. Another parameter will unalter and maintain the optimum condition which is investigated by the anteriorly researchers. The variation of parameters is also shown in Table 3-2 which is described in the parenthesis.

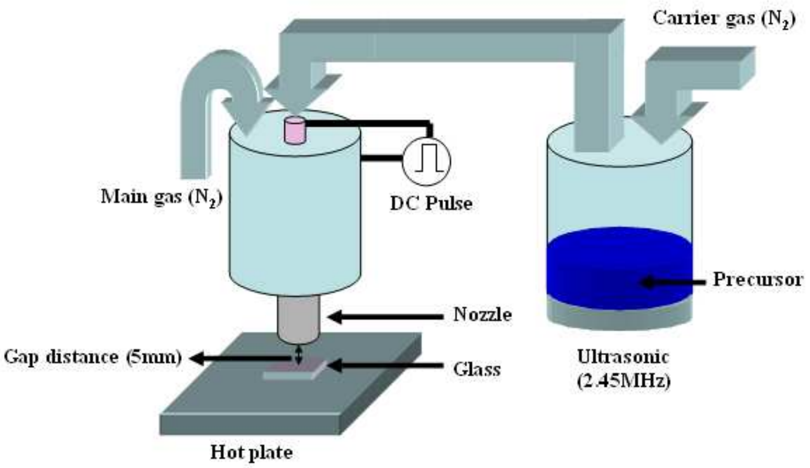

Figure 3-4 Schematic illustration of TCO thin films prepared with APPCVD.

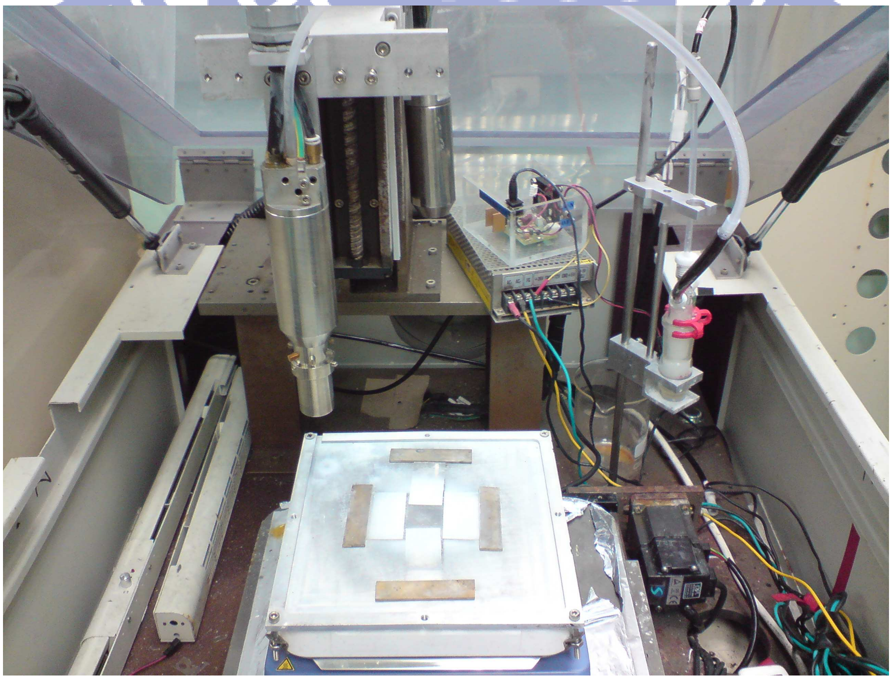

Figure 3-5 APPCVD system of ITRI.

Table 3-3 Parameters of TCO thin films

Parameter	Value
Doping concentration (at%)	0, 2, 4, 6, 8, 10, 12 and 20
Substrate temperature (^{0}C)	100, 200 and 300
Gap distance (mm)	5
Scan times	10
Power (Watt)	~625
Carrier gas flow rate (sccm)	30
Main gas flow rate (SLM)	35
Carrier gas	nitrogen
$Zn(NO_3)_2$ concentration (M)	0.2
Nozzle speed (mm/s)	20
Ultrasonic frequency (MHz)	2.45

In order to investigate the thermal stability of zinc oxide based thin films such as GZO, IZO and ZnO, we put above-mentioned samples in the backend atmosphere anneal furnace at different ambient gases and annealing temperatures to observe the variation and stability of them. According to the previously experiments, we can conclude the AZO thin film which is deposited by APPCVD systems is very unstable, so the APPCVD systems are unsuitable to deposit AZO thin films. Therefore, we only investigate the GZO and IZO in the thermal stability experiments.

The GZO and IZO thin films are prepared by the above experiment procedure which used the optimum parameter, but the power supply voltage is changed from 250 volt to 280 volt which is attributed to the reason of the power transformer decayed. And the zinc oxide is also deposited by APPCVD systems with the same conditions to GZO and IZO thin films, all the experiment and variation parameters are shown in Table 3-3.

Table 3-4 Parameters of thermal stability experiments

Parameter	GZO	IZO	ZnO
Doping concentration (at%)	8	8	0
Substrate temperature (^{0}C)	100		
Gap distance (mm)	5		
Scan times	10		
Power (Watt)	~825		
Carrier gas flow rate (sccm)	30		
Main gas flow rate (SLM)	35		
Carrier gas	Nitrogen		
$Zn(NO_3)_2$ concentration (M)	0.2		
Nozzle speed (mm/s)	20		
Ultrasonic frequency (MHz)	2.45		
Annealing gases	Nitrogen and Oxygen		
Annealing temperatures (^{0}C)	200, 300, 400 and 500		

3.3 Characterization analysis equipments

3.3.1 Scanning Electron microscope (SEM)

SEM stands for scanning electron microscope. The SEM is a microscope that uses electrons instead of light to form an image. Since their development in the 1950, scanning electron microscopes have developed new areas of study in the medical and physical science communities. SEM uses a focused beam of high energy electrons to generate a variety of signals at the surface of solid samples. The signals that derive from electron and sample interactions reveal information about the sample including external morphology, chemical composition, and crystalline structure and orientation of materials making up the sample. The SEM has allowed researchers to inspect a much larger variety of samples.

Accelerated electrons in an SEM carry significant amounts of kinetic energy, and this energy is dissipated as a variety of signals produced by electron and sample interactions when the incident electrons are decelerated in the solid sample. These signals include secondary electrons, backscattered electrons, diffracted backscattered electrons, photons and heat. Secondary electrons and backscattered electrons are commonly used for imaging samples. Secondary electrons are most valuable for showing morphology and topography on samples and backscattered electrons are most valuable for illustrating contrasts in composition in multiphase samples. X-ray generation is produced by inelastic collisions of the incident electrons with electrons in discrete orbital of atoms in the sample. As the excited electrons return to lower energy states, they yield X-rays that are of a fixed wavelength. Thus, characteristic X-rays are produced for each element in a mineral that is excited by the electron beam. SEM analysis is considered to be non-destructive; that is, x-rays generated by electron interactions do not lead to volume loss of the sample, so it is possible to analyze the same materials repeatedly.

The scanning electron microscope has many advantages over traditional microscopes. We describe it following:

(1) It has a large depth of field, which allows more of a specimen to be in focus at one time.

(2) SEM also has much higher resolution, so closely spaced specimens can be magnified at much higher levels.

(3) Because the SEM uses electromagnets rather than lenses, the researcher has much more control in the degree of magnification.

3.3.2 Atomic Force Microscope (AFM)

Atomic force microscopy is a manner of measuring surface morphology on a scale from angstroms to 100 microns. The technique involves imaging a sample through the use of a probe or tip, with a radius of 20 nm. The tip is held several nanometers above the surface using a feedback mechanism that measures surface tip interactions. Variations in tip height are recorded while the tip is scanned repeatedly across the sample, producing a topographic image of the surface.

In addition to basic AFM, the instrument in the Microscopy Suite is capable of producing images in a number of other modes, including tapping, magnetic force, electrical force and pulsed force. In tapping mode, the tip is oscillated above the sample surface, and data may be collected from interactions with surface morphology, stiffness and adhesion. This result in an expanded number of image contrast methods compared to basic AFM. Magnetic force mode imaging utilizes a magnetic tip to enable the visualization of magnetic domains on the sample. In electrical force mode imaging a charged tip is used to locate and record variations in surface charge. In pulsed force mode, the sample is oscillated beneath the tip, and a series of pseudo force distance curves are generated. This permits the separation of sample topography, stiffness, and adhesion values, producing three independent images, or three individual sets of data, simultaneously.

3.3.3 X-Ray diffraction (XRD)

X-ray diffraction is a very important method to characterize the structure of crystalline material. The technique can typically be used for the lattice parameters analysis of single crystals, or the phase, texture or even stress analysis of polycrystalline materials. The technique is widely used in research and development applications and its use for production or quality control issues is also growing, benefiting from developments in hardware and software for high throughput capability.

Most of the applications of X-ray diffractometry require a beam with well defined spatial and spectral characteristics. X-ray optics is a critical component for obtaining the required beam specifications at the sample. Multilayer X-ray optics is now widely used in X-ray diffraction due to their balanced performance in terms of divergence, spectral purity, and flux.

3.3.4 Photoluminescence (PL)

Photoluminescence spectroscopy is a contactless, nondestructive method of probing the electronic structure of materials. Light is directed onto a specimen, where it is absorbed and imparts excess energy into the material in a process called photo-excitation. One manner this excess energy can be dissipated by the sample is through the emission of light, or luminescence. In the case of photo-excitation, this luminescence is called photoluminescence. The intensity and spectral content of this photoluminescence is a direct measure of various important material properties.

Photo-excitation causes electrons within the material to move into permissible excited states. When these electrons return to their equilibrium states, the excess energy is released and may include the emission of light or may not. The energy of the emitted light relates to the difference in energy levels between the two electron states involved in the transition between the excited state and the equilibrium state. The quantity of the emitted light is related to the relative contribution of the radiative process.

3.3.5 Four point probe

A four point probe is a common apparatus for measuring the resistivity of semiconductor samples. By passing a current through two outer probes and measuring the voltage through the inner probes allows the measurement of the substrate resistivity.

The sheet resistivity of the top emitter layer is very easy to measure experimentally using a four point probe. A current is passed through the outer probes and induces a voltage in the inner voltage probes.

Using the voltage and current readings from the probe:

$$\rho_S\left(\frac{\Omega}{Square}\right)=\frac{\pi}{\ln 2}\frac{V}{I} \qquad \text{(Eq. 3-1)}$$

Where:

$$\frac{\pi}{\ln 2}=4.53 \qquad \text{(Eq. 3-2)}$$

In typical usage the current is set to 4.53 mA so that the resistivity is simply the voltage reading in mV.

3.3.6 Hall measurement

If an electric current flows through a conductor in a magnetic field, the magnetic field exerts a transverse force on the moving charge carriers which tends to push them to one side of the conductor. This is most evident in a thin flat conductor as illustrated. A buildup of charge at the sides of the conductors will balance this magnetic influence, producing a measurable voltage between the two sides of the conductor. The presence of this measurable transverse voltage is called the Hall Effect after E. H. Hall who discovered it in 1879.

Note that the direction of the current I in the diagram is that of conventional current, so that the motion of electrons is in the opposite direction. That further confuses all the right-hand rule manipulations you have to go through to get the direction of the forces.

The Hall voltage is given by:

$$V_H = \frac{IB}{ned} \qquad \text{(Eq. 3-3)}$$

Where, n=density of mobile charges; e=electron charge

The Hall Effect can be used to measure magnetic fields with a Hall probe.

3.3.7 Spectrophotometer

A spectrophotometer is an instrument used to measure the intensity of light passing through a sample due to absorption or excitation. Spectrophotometers are used by researchers to determine the absorbance of a sample, ultimately allowing for the determination of color, concentration, or other pertinent information. A wide array of spectrophotometers exists, providing varying wavelength, measurement, and source lamps. The use of spectrophotometers covers just about any industry, from beverage manufacturers to Biochemists. Cole-Parmer is a leading supplier of spectrophotometers including visible, UV visible, atomic absorption, and infrared.

3.3.8 Haze measurement

Haze is the scattering of light by a film that results in a cloudy appearance or poorer clarity of objects when viewed through the film. More technically, haze is the percentage of light transmitted through a film that is deflected more than 2.5° from the direction of the incoming beam. This property is used to describe transparent and translucent films, not opaque films.

Haze is greatly influenced by material selections and product design. Resin characteristics, such as crystallinity and molecular weight distribution, have a key impact. Copolymers are generally hazier than homopolymers. Additives and coatings usually contribute to increased haze. All other things being equal, thicker films will be hazier than thinner films. Additional variables, like process temperatures in the different stages of film-making, can further affect haze, so they are tightly controlled.

As represented in Figure 3-8, a unidirectional light beam is directed onto the film specimen. After it enters an integrating sphere, a photo detector measures the total light transmitted by the film and the amount of transmitted light that is scattered more than 2.5°. Haze is the percentage of total transmitted light that is scattered by more than 2.5°.

3.3.9 Figure of merit

In order to investigate the performance of transparent conductive oxides such as IZO, GZO and AZO which are describing in this paper, the figure of merit (F_H) measured as a parameter of representing the usability of TCO thin films. The figure of merit invented by Haacke was considered. F_H is one of the significant indices for umpiring the effectiveness of a process parameter. F_H is defined as below:

$$F_H\left({square}/{\Omega}\right) = {T^{10}}/{R_S} \qquad \text{(Eq. 3-4)}$$

Where T is the optical transmittance at a particular wavelength (λ=550nm) and RS represents the sheet resistance. The higher value of FH means the better quality of the transparent conductive thin films. We can note that, the figure of merit for commercial ITO thin films was 5.9×10^{-2} square/Ω. In this essay, we will determine the important parameter to compare our TCO thin films with the commercial ITO.

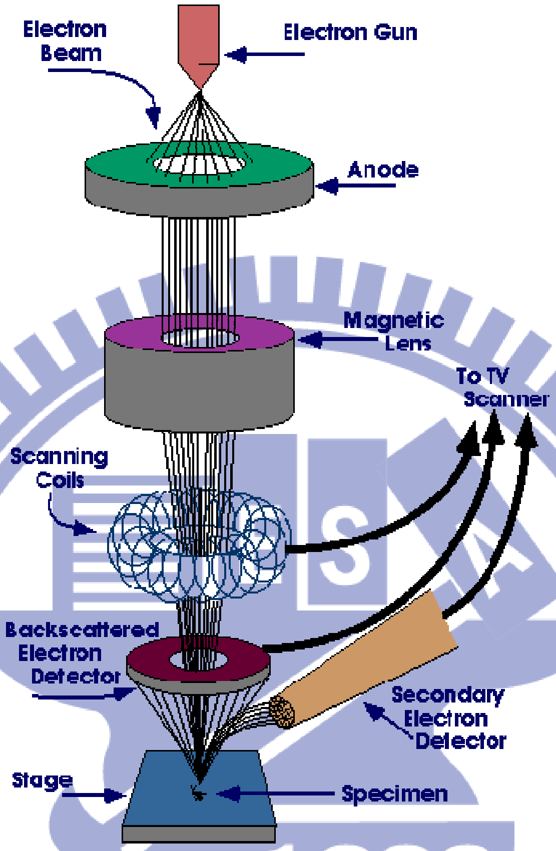

Figure 3-6 Schematic illustration of SEM instrument.

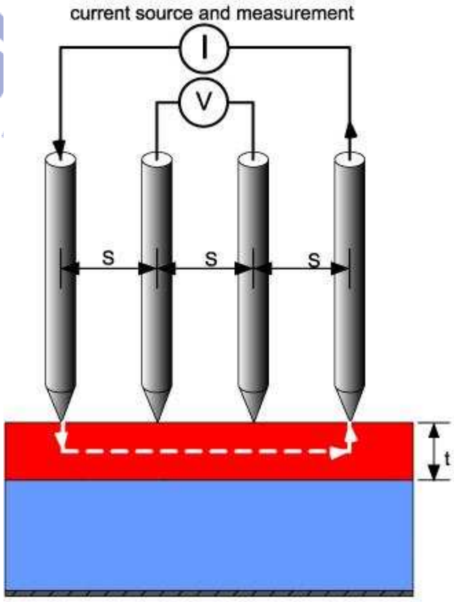

Figure 3-7 Schematic illustration of four point probe principle.

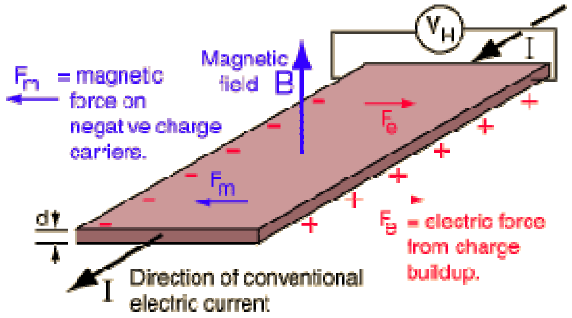

Figure 3-8 Schematic illustration of Hall Effect principle.

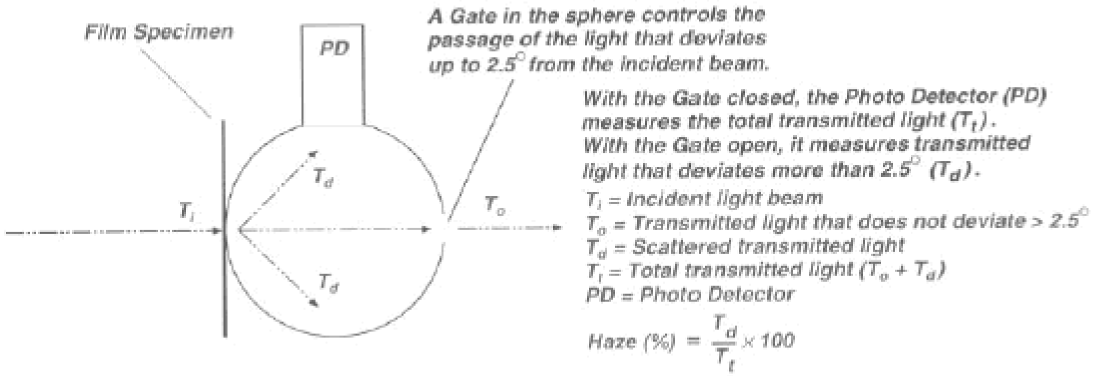

Figure 3-9 Schematic illustration of haze measurement principle.

Table 3-5 Characterization analysis equipments

Instrument	Company and type
SEM	Hitachi S-4700I
AFM	Veeco Dimension 3100
XRD	PANalytical X'Pert Pro
ESCA	PerkinElmer PHI1600
Four point probe	Mitsubishi chemical Loresta-GP MCP-T610
Hall measurement	ECOPIA HMS-3000
Spectrophotometer	VASCO V-570
Haze measurement	BYK-Gardner haze gard plus

Chapter 4

Results and Discussion

In this chapter, we will discuss and explain the opto-electrical characterizations of AZO and IZO thin films by the analysis of SEM, Hall measurement, XRD and PL etc. Next, we will compare some aspects of the TCO thin films, including AZO, GZO and IZO. After the above discussion, we chose the IZO and GZO thin films to investigate the thermal stability in high temperature ambient. Maybe some people will ask why we don’t choose the AZO thin films, aluminum has lots of advantages such as low process cost, abundant in the earth, small ionic radius and when doping to the zinc oxide will not distort the crystal arrangement to decrease the strain in TCO thin films. But in our APPCVD systems, the high activity of aluminum makes it unstable and difficult to control the process conditions and thin film characterizations specifically, so we will not choose the AZO thin films to investigate the thermal stability. Moreover, we also deposit the ZnO thin films by our APPCVD systems in contrast to the IZO and GZO thin films to show the stability after doping the indium or gallium dopants.

4.1 Electrical and optical characterization

4.1.1 Surface morphology

Figure 4-1 and Figure 4-2 show the SEM images of different aluminum and indium doping concentration. First, we can see lots of particles on the AZO thin films, it maybe due to the high activity of aluminum. From the view of CVD process, the precursor from the nozzle may be nucleation in the gas phase and then formation the particles fall on the thin film surface. The CVD process is the precursor will deliver by the main gas to the thin film surface and then migrates on the surface, finally nucleation on the surface to form the TCO thin films. Therefore, the SEM images of AZO have many particles on the surface.

Second, the SEM images of IZO show the needle-like geometry with the increasing of the indium doping concentration; the needle-like geometry will be more obvious. Different from the AZO thin films, the SEM images of IZO show a few particles on the surface, and the reason is low activity of indium element which is the same of above discussion. Now we will introduce the SEM images of GZO thin films which is studying by my classmate, the SEM images of GZO is different from the AZO and IZO thin films, so we will realize the different doping element will cause distinct surface morphology.

Figure 4-3 and Figure 4-4 also show the SEM images of AZO and IZO which represent the different substrate temperature at the deposition process, respectively. The surface morphology is almost the same with our above discussion in different doping concentration.

We also use the AFM to analyze the surface morphology which is shown in Figure 4-5 and Figure 4-6 represented the IZO of different indium doping concentration and different substrate temperature. The analysis of AFM is similar to the SEM images in our experiments.

4.1.2 Structure properties

Figure 4-7 shows the GIXRD patterns with different Al doping concentration. The XRD patterns show the films are nanocrystalline and the (002) peak has a higher intensity than the (101) peak, this is a powerful indication for a preferential orientation of the ZnO crystallite with the c-axis normal to the film plane. The other weaker orientations observed in the X-ray diffraction pattern were (100), (101), (102), (110), (103) and (112) which shows our AZO films deposited by APPCVD systems were polycrystalline. The (002) peak intensity decreases at the doping concentration with 2at% and reaches to the maximum value at 6at%, then decreased for the higher doping levels. This is due to the few precursors reach on the substrate surface then formation the AZO thin films, and the other precursors may be nucleation at the gas phase then formation the particles falling on the surface and do not contribution the AZO thin films at the 2at%. Afterward, the doping Al^{3+} ions replace the Zn^{2+} ions in the ZnO lattice at the doping concentration with 6at%. However at higher Al doping concentration, apart from replace the Zn^{2+} ions; Al^{3+} ions may occupy the interstitial position in the ZnO lattice.

Figure 4-8 also shows the GIXRD patterns of different In doping concentration. XRD patterns show the same result with the AZO patterns. The polycrystalline IZO thin films was observed and the strong (002) peak of hexagonal (wurtzite) ZnO, indicating an oriented growth along the c-axis perpendicular to the substrate surface. Now, we pay attention to the FWHM values increase from 0.447° to 1.139° with increasing the In doping concentration. Using the Debye-Scherrer equation (shown below), the crystallite size of IZO films decrease from 78.44nm to 10.4nm (shown in Figure 4-9), which means that the IZO thin films will become amorphous phase when increasing the doping concentration. And the same phenomenon occurs in the case of GZO thin films (shown in Figure 4-10). But it is not observed in AZO thin films apparently (shown in Figure 4-11), this evidence may be due to the lots of particles on the thin films surface cause to the XRD analysis inexactly.

$$D = \frac{0.9\lambda}{\beta \cos\theta} \qquad \text{(Eq. 4-1)}$$

Where D is the diameter of the crystallites forming the film, λ is the wavelength, β is the FWHM in radians and θ is Bragg’s angle.

Now, we also observed the 2-theta value of (002) peak decreases with increasing the In doping concentration. We can use the Bragg diffraction condition (shown below) to explain it. According to the Bragg condition, when the theta value decreases, it means the d-spacing value will increase. Our experimental result reveals the same tendency with the Bragg condition theory; we can interpret the evidence by the ionic radius. The ionic radius of zinc ion is 0.088nm and the ionic radius of indium is 0.094nm, when indium replaces the zinc at the substitutional site, the ZnO lattice will sustain the tensile strain and then the distance of the lattice plane (d value) will increased (shown in Figure 4-17). On the other hand, we consider the AZO thin films which have the opposite evidence to the IZO thin films. The ionic radius of aluminum is 0.0535nm which is smaller than the zinc ion, so the aluminum replace the zinc at the substitutional site, the ZnO lattice will sustain the compressive strain and then the distance of the lattice plan will decreased (shown in Figure 4-18). And now, we introduce the GZO thin films in this case to emphasize our contention. The ionic radius of gallium is 0.076nm which is also smaller than the zinc ion, so the same evidence will occur in the case of GZO thin films (shown in Figure 4-16). So, the different element doping to the ZnO will cause the 2-theta value increased or decreased depend on their ionic radius compared with the zinc ion.

$$2d\sin\theta = n\lambda \qquad \text{(Eq. 4-2)}$$

Where n is an integer determined by the order given, and λ is the wavelength.

Figure 4-19 and Figure 4-20 show the GIXRD patterns with different substrate temperature of AZO and IZO thin films. These XRD pattern show the same facts with our above discussion. They are polycrystalline phase and grown along the c-axis normal to the substrate surface. We can observe the XRD patterns of IZO which is unchanged obviously with different substrate temperature. The XRD patterns of AZO which the (002) peak and other peaks decreasing and increasing with higher substrate temperature respectively. This is due to more particles formation at high substrate temperature, and the orientation of particles is random, so the result is reasonable.

4.1.3 Electrical properties

The electrical characterizations of IZO with different In concentration shows in Figure 4-21. The resistivity is well-known inverse proportional to the mobility and carrier concentration. Therefore, when the mobility multiplies by the carrier concentration which gets the maximum value, the resistivity shall be the minimum value. First, we consider the carrier concentration which is function of In doping concentration. The carrier concentration as a function of the [In]/[Zn]+[In] ratio in the starting solution shows a increase as the [In]/[Zn]+[In] rate is increased, and then reaching a maximum value at particular [In]/[Zn]+[In] ratio (8at%), further decrease in the carrier concentration values is observed when the [In]/[Zn]+[In] rate increases. In the case of low [In]/[Zn]+[In] ratio, the carrier concentration is consequent the increase the In atoms that are incorporated into the lattice ZnO in the zinc substitutional site, until reaching to the maximum values that the In atoms can solute in the ZnO lattice. For higher [In]/[Zn]+[In] ratio in solution, the In atoms don’t occupy the extra zinc substitutional site, and a separation of In in an oxide form take place in the interstitials or grain boundaries, then inducing the decrease the carrier concentration and mobility and a subsequent ascend in the electrical resistivity. Furthermore, in the case of high [In]/[Zn]+[In] ratio, more In atoms will participate in the arrangement of the ZnO lattice, causing difficult to arrange the wurtzite structure then degrading the crystallinity of the ZnO thin films.

Second, we proceed discussion with the mobility which also as a function of the [In]/[Zn]＋[In] ratio in the starting solution .The mobility as a function of the [In]/[Zn]＋[In] ratio can interpret by the grain barrier limited transport which is a theory of the carrier transport in polycrystalline thin films whose first described comprehensively by Seto [82]. Polycrystalline films have some electronic defect in the band gap of semiconductors. These defects are charged by the free carrier at the interface of the grains. In our TCO thin films which are n-type material will generate a depletion area on the both side of the grain boundary barrier led to an energetic barrier for the electrons. Seto claim the barrier is a delta-shaped density of electron trap state in the band gap, and the barrier height is depend on the charge carrier trap density at the grain boundaries, the barrier width decreasing with increasing the carrier concentration. When the barrier width becomes narrow, the carrier can via the quantum mechanical tunneling path through the barrier. Back to our experimental result, for low [In]/[Zn]＋[In] ratio the mobility increasing is due to the narrowing of the barrier width which is occupied by the carrier, and then permitting more free carrier can path through the gain boundaries to increase the mobility, until the barrier width is narrow enough to ignore (we assume the trap density is unchanged) . For higher [In]/[Zn]＋[In] ratio the mobility is not depend on the grain boundary barrier, contrarily depend on the bulk grain of the polycrystalline films. The resistivity is from 5.84E-3 to 1.71E-3 which means the 2at% to the 8at% doping concentration. The minimum value of resistivity is found in films deposited at [In]/[Zn]+[In] = 8at%.

$$\frac{1}{\mu}=\frac{1}{\mu_i}+\frac{1}{\mu_l}+\frac{1}{\mu_g}+\frac{1}{\mu_n} \qquad \text{(Eq. 4-3)}$$

Where μ represents the mobility of polycrystalline films, μ_i is the mobility of ionized impurity scattering, μ_l is the mobility of lattice phonon scattering, μ_g is the mobility of grain boundary scattering, μ_n is the mobility of neutral impurity scattering.

Figure 4-22 shows the hall measurement of IZO thin films with different substrate temperatures. We can observe the carrier concentration and the mobility increasing with the substrate temperature up to 200^{o}C. This is due to the better activation of the In doping atoms in ZnO lattice at the 200 ^{o}C, so the carrier concentration will increased then driving to the mobility to a larger value. When the substrate temperature increases to the 300 ^{o}C, the oxygen atoms whose from air may incorporate into the IZO thin films. It will repair the oxygen vacancies or other shallow donors, causing the decrease of carrier concentration.

Figure 4-23 shows the electrical properties of AZO thin films with different Al doping concentration. We can observe the carrier concentration increasing continuously even at the 20at%. According to above discussion, the high activity of aluminum make the AZO thin films difficult to control the process condition, so even the doping concentration reaches to the 20at% but we can believe that some precursor nucleated at the gas phase and the actual doping concentration is smaller than the experimental value. The mobility decreases with increasing the doping concentration; we can interpret it by the reason of lots of particles fall on the surface, decreasing the mobility with increasing the doping concentration. Figure 4-24 exhibits the electrical characterizations of AZO thin films with different substrate temperature. We can see that the carrier concentration and mobility decrease with increasing the substrate temperature. It can be explained by the annealing effect, the oxygen atoms from the air will be incorporated in the AZO films with increasing the substrate temperature, then repairing the oxygen vacancies to decrease the carrier concentration. Equally, the oxygen atoms incorporated in the ZnO films will also destroying the crystal arrangement then decreasing the mobility subsequently.

4.1.4 Optical properties

The optical properties of IZO thin films with different In doping concentration show in the Figure 4-25. All films with different doping concentration are highly transparent in the visible region. The average transparency of IZO thin films is 75~86% in the region of 400~800nm, pondering the oscillations perceived in the spectrum due to interference effects. We observed the different wavelength of the absorption edge with distinct doping concentration which is mainly due to the different carrier concentration. When the carrier concentration increases to a certain value to make the IZO be a degenerate semiconductor. The bottom of the conduction band will accumulate degenerated electrons and this results in a shift of quasi-Fermi level of electrons in the conduction band, causing the electron suffer larger energy gap to transition from valence band to conduction band then the effective band gap increases subsequently. This phenomenon is well-known the Burstein-Moss shift [83] which is commonly used in the heavily doped semiconductors. The energy band gap of the IZO thin films estimate by the slope of the linear region which extract from the plot of $(\alpha h\nu)^2$ versus hν. From the Burstein-Moss shift theory, the tendency of carrier concentration may be similar to the trend of band gap. Figure 4-26 shows the same tendency of carrier concentration and band gap energy in our experiment.

Figure 4-27 shows the optical studies of IZO with different substrate temperature. We observe the wavelength shift of absorption edge increasing with increasing the substrate temperature, but it is different from the trend of hall measurement and band gap extraction which is shown in Figure 4-28. The reason may be attributed to the thinner of thickness at 100°C than the other temperatures. According to the transmittance equation (shown below), when the absorption coefficient is large enough to degrade the transmittance at the absorption edge, the thickness of thin films is too thin to make transmittance decreasing slowly down. Therefore, the absorption edge of 100°C will small than the 200°C which is shown in Figure 4-27.

$$T = (1 - R^2)e^{-\alpha d} \qquad \text{(Eq. 4-4)}$$

Where R represents the reflection coefficient, α is the absorption coefficient, d is the thickness of thin films.

Figure 4-29 shows the optical properties of AZO thin films with different doping concentration. The average transmittance is in the range of 60~70% which is procured by numerous particles fall on the surface then decreasing the optical transmittance. We also observed the shift of absorption edge which obey the Burstein-Moss effect and similar to the hall measurement of carrier concentration shown in Figure 4-30. The optical characterizations with different substrate temperature of AZO thin films are shown in Figure 4-31, too. The average transmittance is about 65~75% and the absorption edge shift which conform to the hall measurement shows in the Figure 4-32.

In order to determine the quality of TCO thin films, we introduce a parameter which is defined by our above statement in the section of 3.3.11. Figure 4-33 shows the variation of the figure of merit for different doping concentration IZO films. As the doping concentration increases, the figure of merit increases for light doping and decreases for heavily doping. The highest figure of merit obtained is 7.49E-3 (Ω^{-1}) for 10at% IZO thin films, and the range of 8~12at% shows fine quality in IZO films. Even though the 10at% exhibits the best figure of merit, but we will chose the 8at% one to be the best condition at the consideration of cost factor. Figure 4-34 also shows the variation of figure of merit for different doping concentration AZO films. It has the same tendency with the IZO thin films, and the largest figure of merit obtained is 6.22E-4 for 12at% AZO films which smaller than the average value of IZO films. So, the AZO thin films exhibit bad performance for optoelectronic devices in the deposition methods of APPCVD system. Moreover, we can introduce the GZO thin films which also prepared by the APPCVD system. The same tendency shows in GZO films with IZO and AZO thin films, the value of figure of merit obtained is 6.76E-3 for 8at% GZO films which is similar to the IZO films (6.28E-3). Even though the resistivity of IZO is larger than the GZO, but the transmittance at visible range of IZO is higher than GZO, so they exhibit similar in the value of figure of merit. We can employ them individually in different purpose which will get the best performance.

4.1.5 Photoluminescence spectra

To further research the defect states in IZO films, room temperature photoluminescence spectra were introduced to inspect the IZO thin films. Figure 4-35 shows the room temperature PL spectra with different doping concentration in IZO films. As shown in the figure, the intensity of near band edge emission depends on the In concentration, and it decreases with the increase of doping concentration. We can interpret that such phenomenon is due to nonradiative Auger recombination processes which is reported by Tsang et al. [84]. In Auger recombination process, the degenerate electrons depend on the doping level of material. They release their energy by an electron recombination which instantly absorbed by another electron, and then the energy is dispelled by phonons. In semiconductor thin films, quantum wells and quantum dots, Auger recombination process has been a major reason of nonradiative recombination. Our experimental results, the IZO thin films is a wide band gap material, and the carrier concentration is above 10E20 which over the Mott density (10E18 cm^{-3}). So, the Auger recombination will be more important in our prepared IZO thin films. Furthermore, except for the above-mentioned reason, the impurity clusters or impurity-defect complexes will limit the radiative efficiency of IZO thin films at higher In doping concentration [85]. Moreover, we also observed that the FWHM of NBE emission peak increase with increasing the doping concentration shown in Figure 4-36 which is similar to the result of XRD analysis, representing the crystallinity decreases subsequently.

Except for the near band edge emission, we also observed a very broad intensity in ZnO where centre at about 2.5eV which is shown in Figure 4-36 and called blue-green emission. The reason of this phenomenon has not been completely understand. It has been explained in lots of statements, including the emission is associated with copper impurities at a substitutional site, the blue-green emission may be attributed to oxygen vacancies and porosity of the films, the emission may be related to a transition within a self-activated center formed by a doubly ionized zinc vacancy and the ionized interstitial zinc, the reason of this emission is due to the electronic transition from the bottom of the conduction band to the antisite defect (O_{Zn}) oxygen zinc level. Using the full-potential linear muffin-tin orbital method, the energy states of the ZnO films were be calculated [86]. According to the defect levels between conduction band and valence band of ZnO films, the O_{Zn} level is 2.38eV, which is similar to the energy of blue-green emission of PL obtained in our experiment (2.48eV). The analytic consequence of blue-green emission of PL spectra is identical to our deposition condition where is prepared at air ambient contained abound oxygen, so the O_{Zn} defects will easily generated at this environment. However, the blue-green emission is not observed in our indium doped ZnO, even though the reason is still unknown, but we can guess that it may be due to the defect levels eliminated by the doping elements, or the nonradiative emission at the grain boundaries dominates the PL spectra, or the emission spectra are occurred out of our analytic range.

Figure 4-37 shows the room temperature PL spectra with different substrate temperature in IZO films. At low substrate temperature, the film precursor do not have enough energy to migration and nucleation, so the quality of IZO thin films will be reduced then the defects increased subsequently. When the substrate temperature reaches to 200°C, the NBE emission and deep level emission decreased which is due to the more energy to supply precursor migration and nucleation on the substrate surface. At high substrate temperature, we observed the deep level emission shifts to the lower photon energy which indicated the V_O and O_i dominate the transition between the conduction band and valence band, and it means that oxygen release out of the IZO thin films.

4.2 Thermal stability

4.2.1 Surface morphology

Figure 4-38, Figure 4-39 and Figure 4-40 show the top view in SEM analysis with different annealing condition of IZO, GZO and ZnO respectively. We can't observe obvious variation of these SEM images, representing the annealing treatment will not change the surface morphology apparently. Also, we analyze the surface structure of these thin films with AFM analysis which shown in Figure 4-41, Figure 4-42 and Figure 4-43 respectively. Similar to the SEM images, the AFM analysis show unapparent variation of our heat treatment.

4.2.2 Structure properties

The XRD patterns with different annealing temperature in oxygen and nitrogen ambient of IZO thin films are shown in Figure 4-44 and Figure 4-45 respectively. The XRD patterns of IZO thin films exhibit unobvious change, indicating the annealing treatment will not degrade the structure quality of our deposited IZO thin films. The same situation is also emerged in our deposited GZO thin films which the XRD patterns are shown in Figure 4-46 and 4-47. Nevertheless, the (002) peak intensity of ZnO films increase with higher annealing temperature which shown in Figure 4-48 and Figure 4-49, and more obvious in nitrogen ambient which is the reason of less oxygen chemical absorption. So, the heat treatment not only degrades the structure characteristic of IZO and GZO films, but also increasing the (002) peak of ZnO films.

However, the (002) peak position of IZO, GZO and ZnO films are altered to a higher value which shown in below tables (also shown in

Figure 4-50~4-55). It may be due to the O_2 chemisorption on the surface of IZO, GZO and ZnO films after annealing, and resulted in the distortion of crystallites.

Same of the above discussion, we also use the Sherrer equation to calculate the crystallite size of our thin films. The specific values are shown in the following tables. No apparent change of our films after annealing treatment.

Until present, the annealing treatment does not influence our IZO and GZO thin films in surface morphology and crystal structure obviously. So, the thermal stability of surface and crystal structure is exhibited in IZO and GZO films.

4.2.3 Electrical properties

Figure 4-56 and Figure 4-57 show the electrical characterizations of IZO thin films annealed for 30 minutes which were calculated from thermal stability in oxygen and nitrogen ambient gases respectively. As shown in the two figures, the IZO thin films show good thermal stability in both nitrogen and oxygen ambient. Annealing in nitrogen shows more stability than in oxygen ambient gas which is the reason of more O_2 chemisorption in the case of oxygen ambient and then will occupy the oxygen vacancies, decreasing the carrier concentration subsequently. However, the carrier concentration is dominates by In^{3+} ions occupied substitutional site of Zn^{2+} ions, also the shallow donors such as oxygen vacancies and zinc interstitial atoms will contributed free carrier. When these shallow donors occupied by the oxygen atoms, the carrier concentration will decrease slightly which is due to the shallow donors contribute less free electrons. So, the IZO thin films show good thermal stability in both nitrogen and oxygen ambient gas.

The electrical properties of GZO thin films annealed for 30 minutes in oxygen and nitrogen ambient gases which shown in Figure 4-58 and Figure 4-59 respectively. Apparently, the thermal stability of IZO films is better than GZO films that annealing below 400^{o}C either in nitrogen and oxygen ambient. Figure 4-58 shows the electrical data of GZO at 300^{o}C annealing temperature only, which is due to the higher temperature samples over the measurement limitation. So, we can't measure the specific values which are over the 300^{o}C annealing temperature in oxygen ambient of GZO thin films.

As shown in Figure 4-60, the resistivity of as-deposited ZnO films is 3.195E-2 Ω cm. Nevertheless, after heat treatment in oxygen ambient, the resistivity of ZnO films increased by six orders of magnitude at 400^{o}C annealing. In contrast with the above discussion IZO and GZO thin films, the thermal stability of resistivity in IZO and GZO is better than that in ZnO films. In the case of ZnO films, the free electrons are mainly from shallow donors who associated with oxygen vacancies and zinc interstitial atoms. The increase in resistivity after heat treatment can be explained by the decreasing of carrier concentration which is attributed to the chemisorption on the ZnO surface by oxygen atoms. The chemisorped oxygen atoms will eliminate shallow donors which primordial from native defects such as oxygen vacancies and zinc interstitial atoms, then the carrier concentration will decrease remarkably. According to the previous investigation, the chemisoption of oxygen atoms in ZnO thin films is notable above 200^{o}C which is also exhibited in our experiment as shown in Figure 4-60. It can be concluded that the chemisorption of oxygen atoms has a few effect on IZO and GZO thin films than ZnO films.

4.2.4 Optical properties

The optical characterizations with different annealing temperature of IZO and GZO thin films in oxygen and nitrogen are shown in Figure 4-62~4-65. In the case of IZO thin films, the average transmittance does not vary obviously in visible light range. The absorption edge moves to higher wavelength with increasing the annealing temperature either in oxygen and nitrogen ambient which is due to the Burstein-Moss shift. The same evidence also occurs in the GZO thin films, but we observe that the average transmittance in visible light decreases with increasing the annealing temperature. We also quote the hall measurement to compare with the optical properties. The absorption edge moves to higher wavelength which means the decease of carrier concentration. The hall measurement is conformed to the optical properties which are shown in Figure 4-66~4-69 of IZO and GZO thin films.

Immediately, we will introduce a parameter that is call plasma wavelength to explain the optical properties of IZO and GZO thin films. The electrons on the plasma surface will leave out of plasma which caused by certain disturbance, the attraction of ions will prevent electrons then pull back them subsequently. Due to the inertia of electrons, the electrons will over the original position caused by the force of ionic attraction. Then, it will be a collective longitudinal simple harmonic motion which is commonly called plasma oscillation SHM. It has a particular wavelength called plasma frequency which relate to the carrier concentration. The equation of plasma frequency is shown below. Plasma frequency has a corresponding plasma wavelength, when the wavelength of incident light is greater than it, the incident light will be reflected. When the wavelength of incident light is equal to plasma wavelength, the light will be absorbed. When the wavelength of incident light is smaller than plasma wavelength, the light will be transmitted.

$$f_P = 8980N^{\frac{1}{2}} \qquad \text{(Eq. 4-5)}$$

$$f_p \times \lambda_p = C \qquad \text{(Eq. 4-6)}$$

Where N represents carrier concentration in the unit of cm^{-3}, C is light velocity.

Figure 4-70~4-73 show the optical characterizations in the range of 300-2200nm with different annealing temperature of IZO and GZO thin films in oxygen and nitrogen gases. They exhibit apparent plasma wavelength shift at infrared rays region. According to the above discussion about plasma wavelength, decreasing the carrier concentration will increase plasma wavelength immediately. So, the degrading of transmittance will move to higher wavelength which is shown in our experiment. These result also conformed to the hall measurement and absorption edge shift.

The optical properties with different annealing temperature of ZnO in oxygen and nitrogen ambient are shown in Figure 4-74 and Figure 4-75. The average transmittance and the absorption edge do not change obvious; the average transmittance at 550nm is about 84% which is due to the fewer carrier concentration of ZnO thin films.

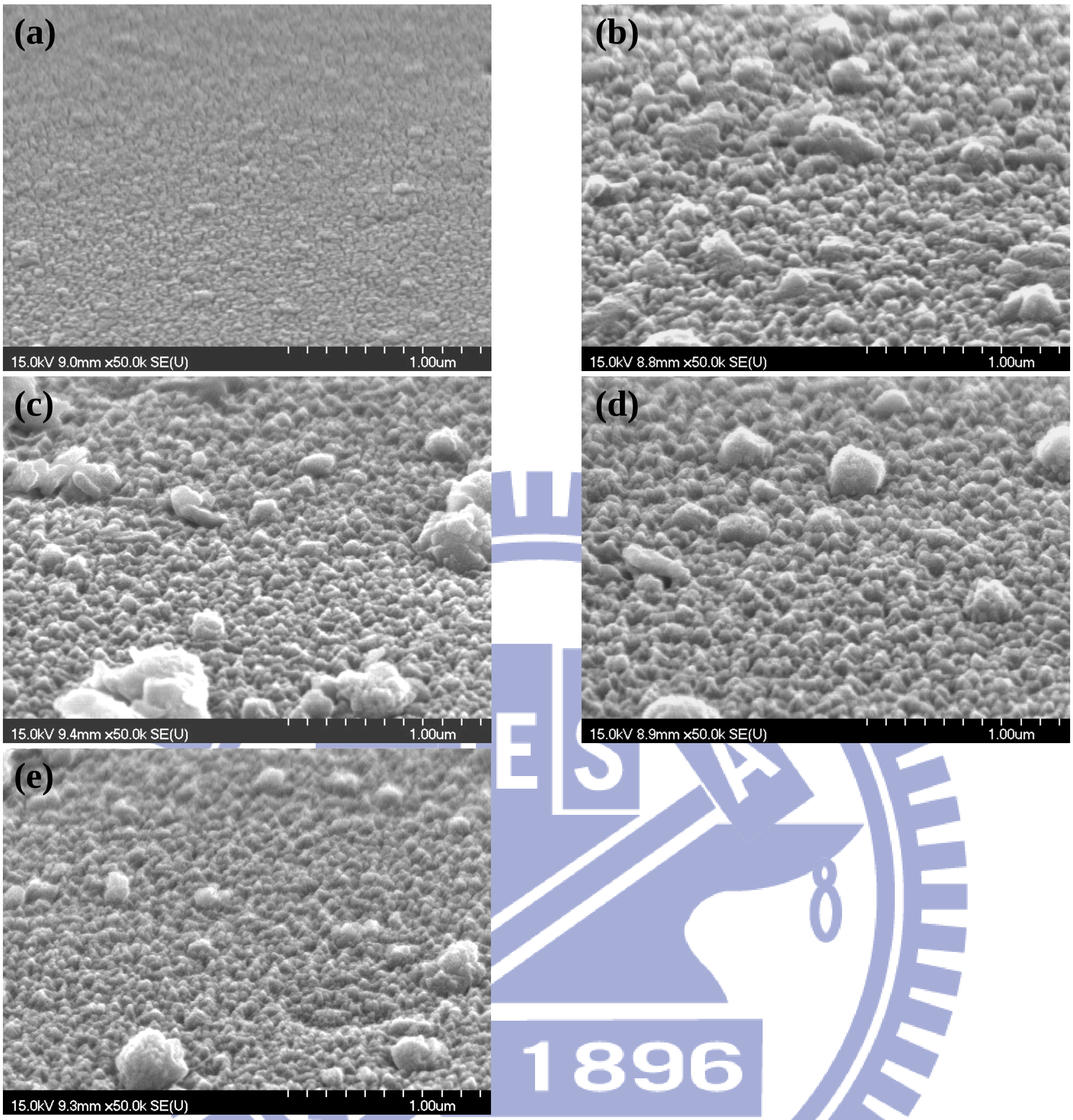

Figure 4-1 SEM images of deposited AZO thin films which is prepared with different Al concentration (a) 0at% (b) 2at% (c) 6at% (d) 12at% (e) 20at%.

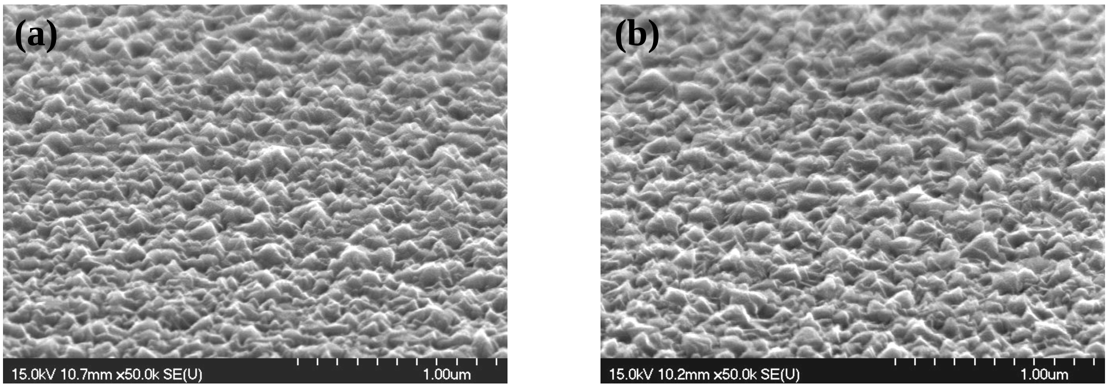

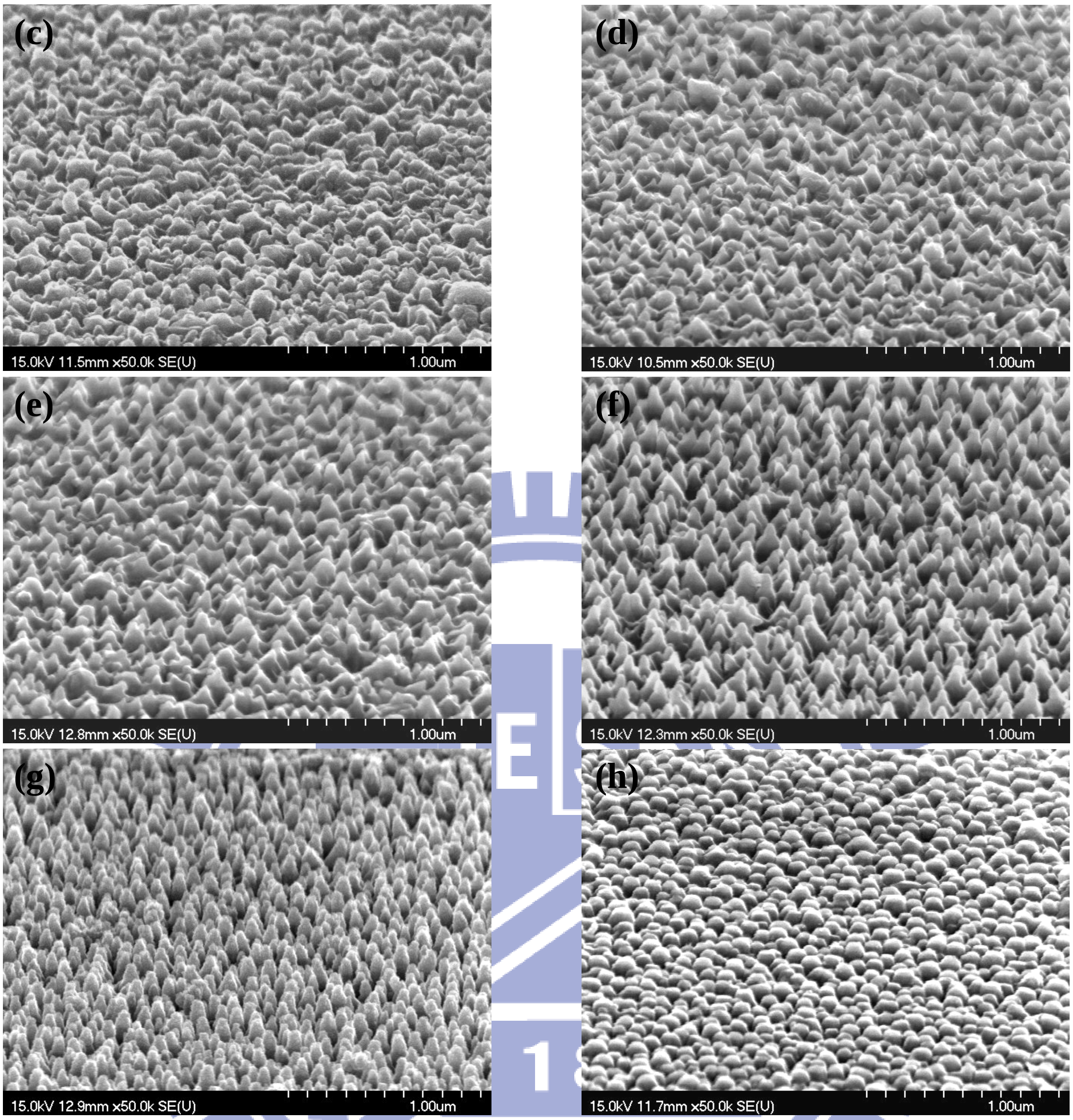

Figure 4-2 SEM images of deposited IZO thin films which is prepared with different In concentration (a) 0at% (b) 2at% (c) 4at% (d) 6at% (e) 8at% (f) 10at% (g) 12at% (h) 20at%.

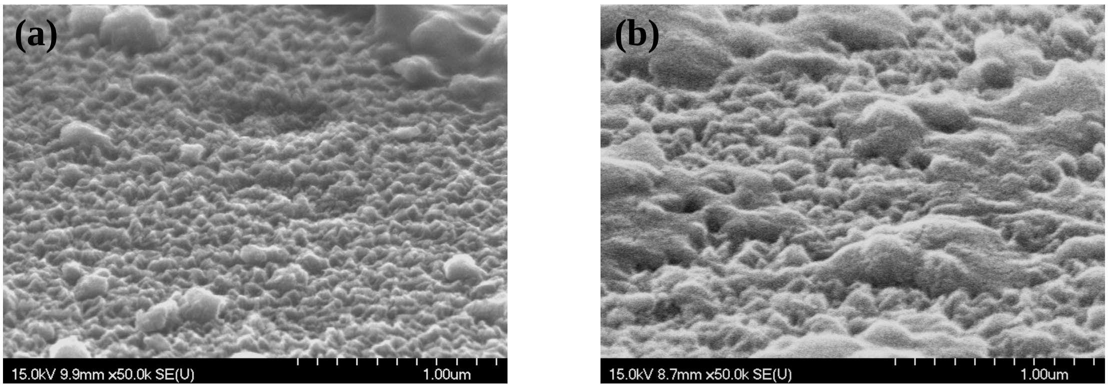

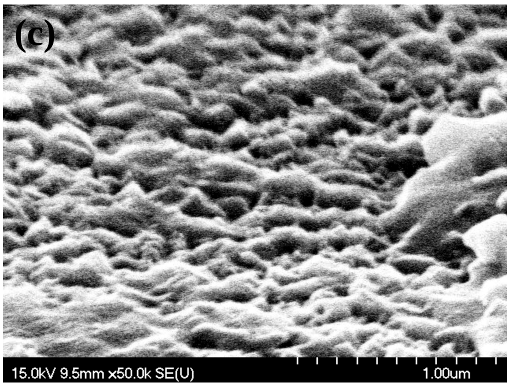

Figure 4-3 SEM images of deposited AZO thin films which is prepared with different substrate temperature (a) 100°C (b) 200°C (c) 300°C.

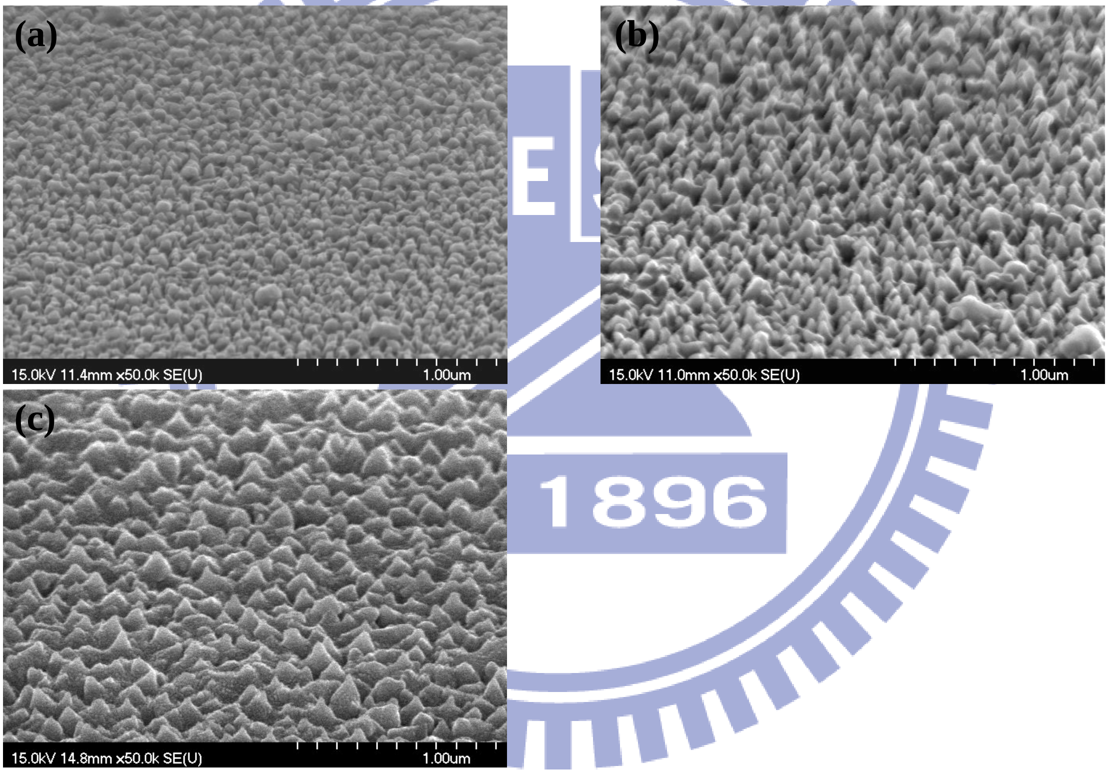

Figure 4-4 SEM images of deposited IZO thin films which is prepared with different substrate temperature (a) 100°C (b) 200°C (c) 300°C.

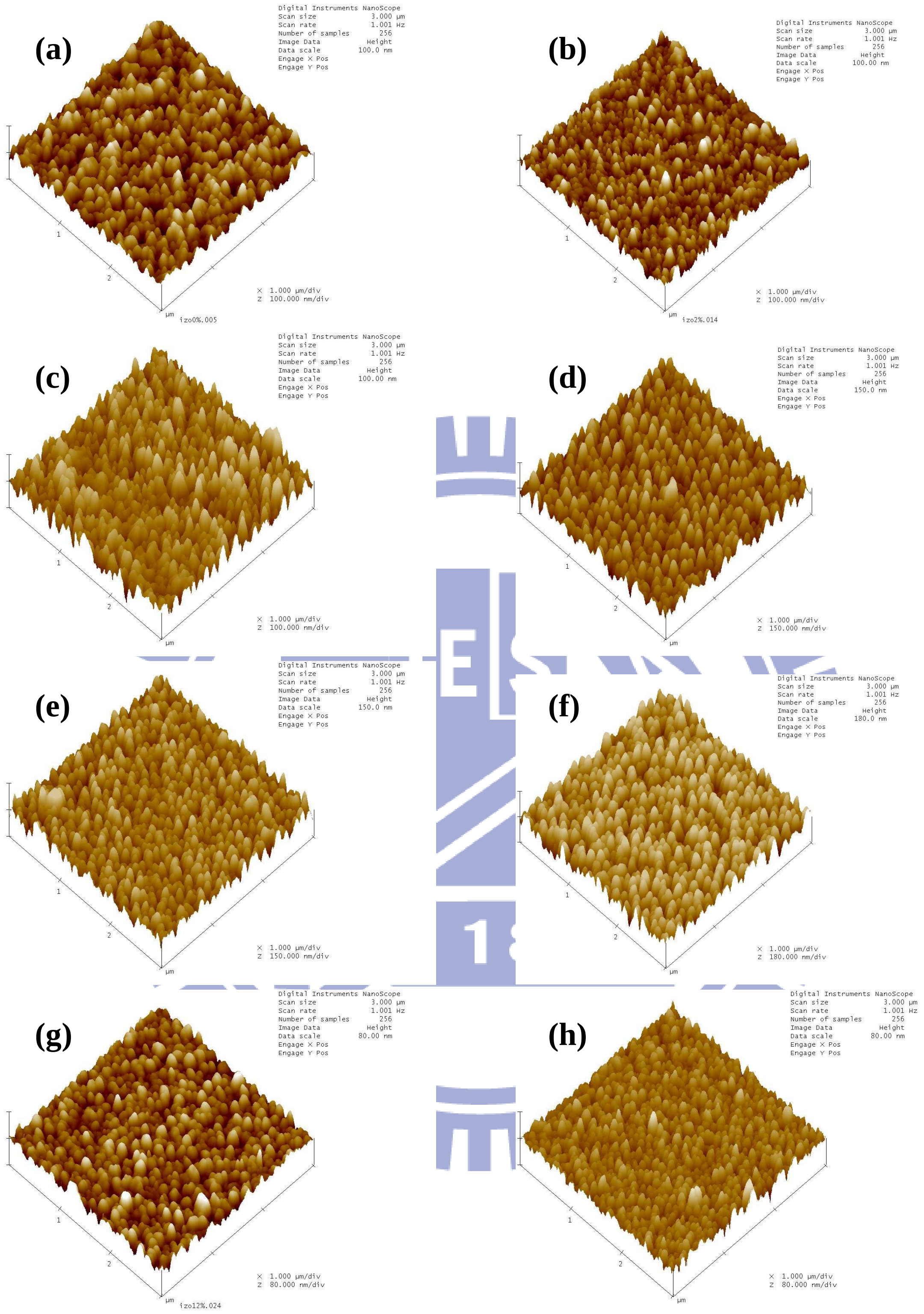

Figure 4-5 AFM images of deposited IZO thin films which is prepared with different In concentration (a) 0at% (b) 2at% (c) 4at% (d) 6at% (e) 8at% (f) 10at% (g) 12at% (h) 20at%.

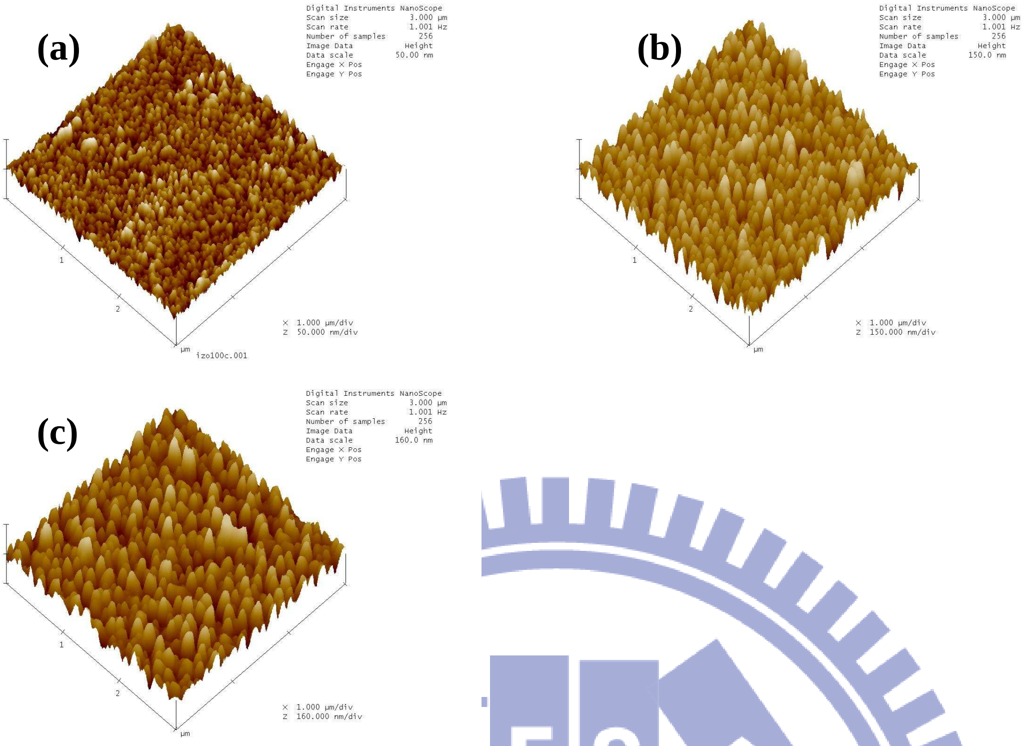

Figure 4-6 AFM images of deposited IZO thin films which is prepared with different substrate temperature (a) 100^{o}C (b) 200^{o}C (c) 300^{o}C.

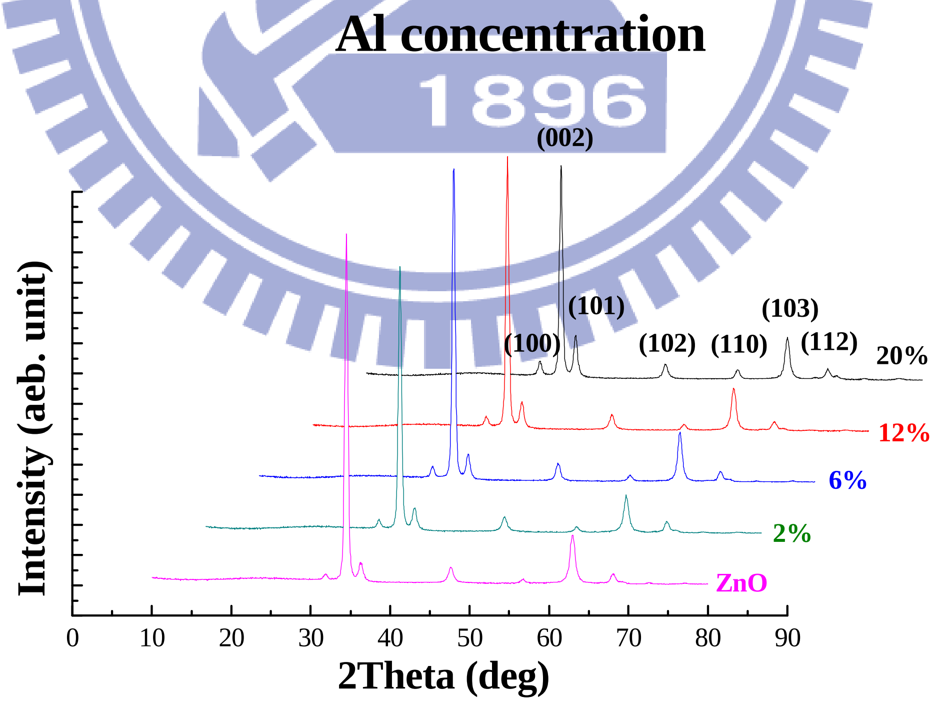

Figure 4-7 GIXRD patterns of ZnO and AZO thin films deposited with different Al concentration.

In concentration

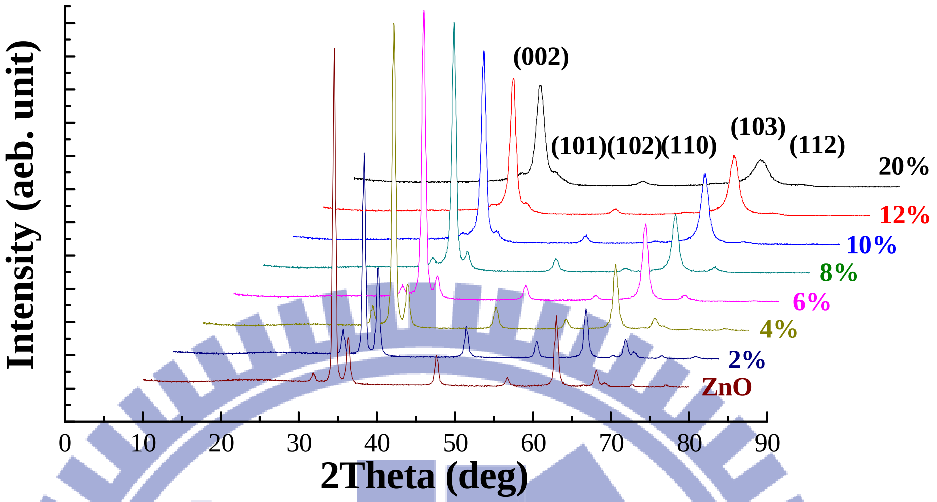

Figure 4-8 GIXRD patterns of ZnO and IZO thin films deposited with different In concentration.

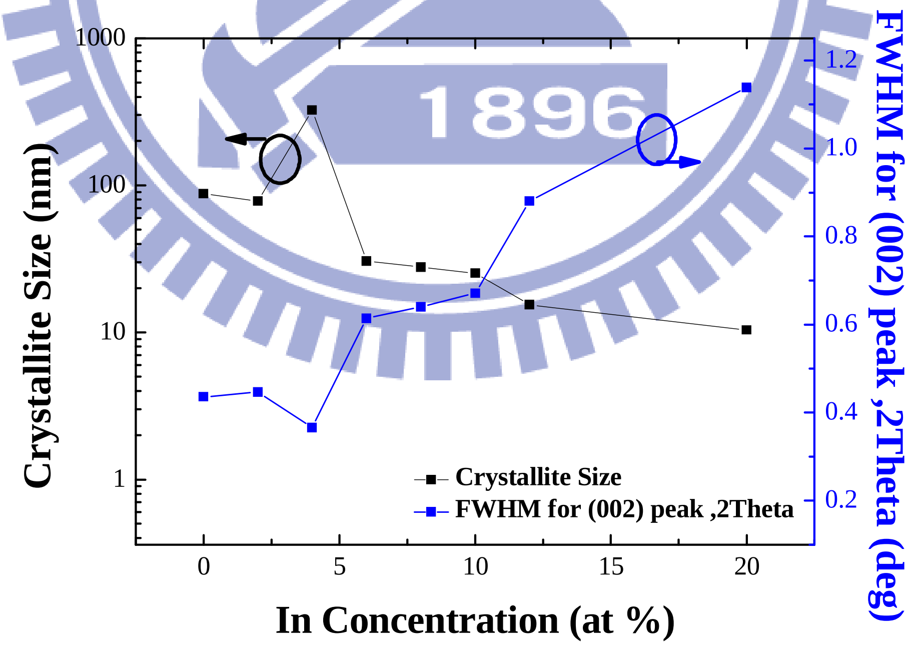

Figure 4-9 Variation of crystallite size and the FWHM for (002) peak of IZO thin films with different In concentration.

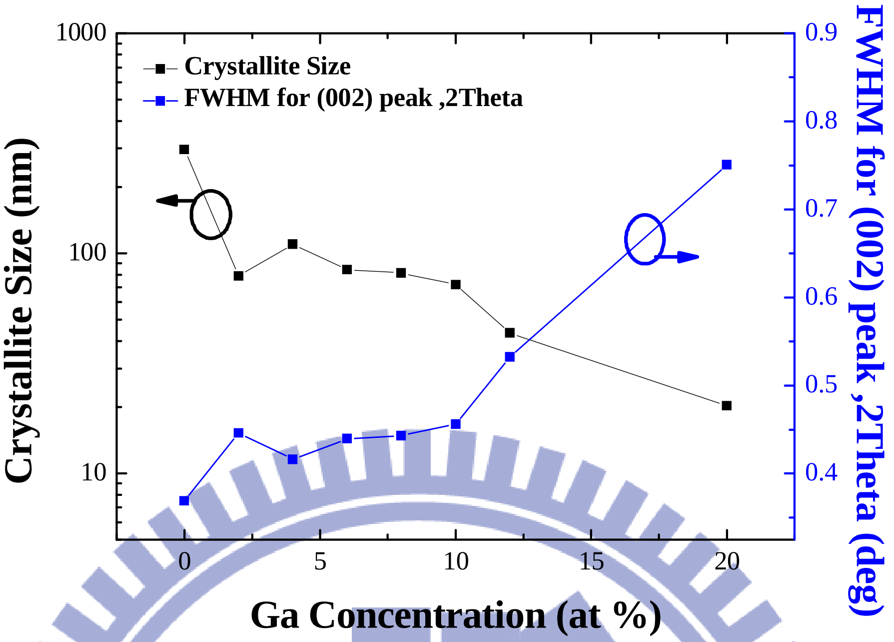

Figure 4-10 Variation of crystallite size and the FWHM for (002) peak of GZO thin films with different Ga concentration.

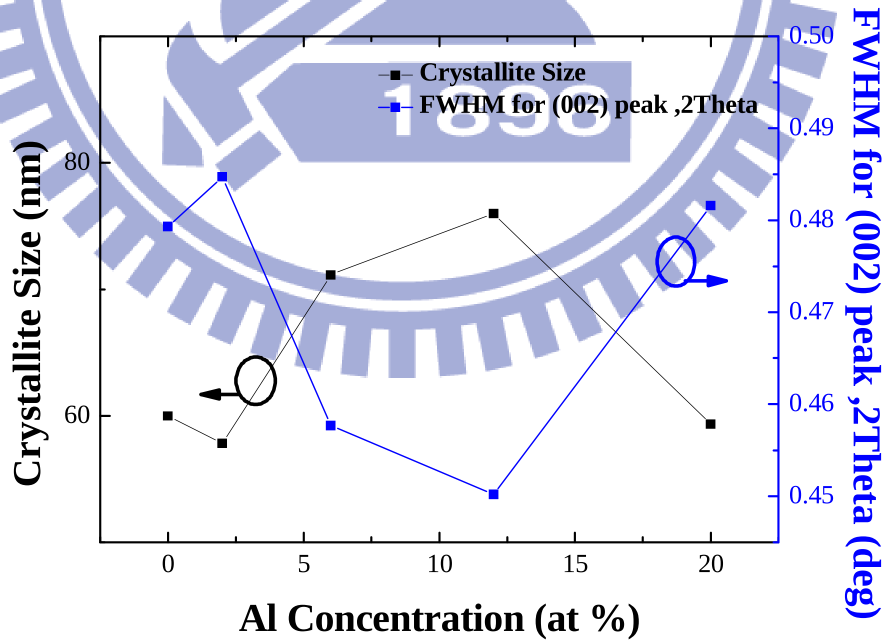

Figure 4-11 Variation of crystallite size and the FWHM for (002) peak of AZO thin films with different Al concentration.

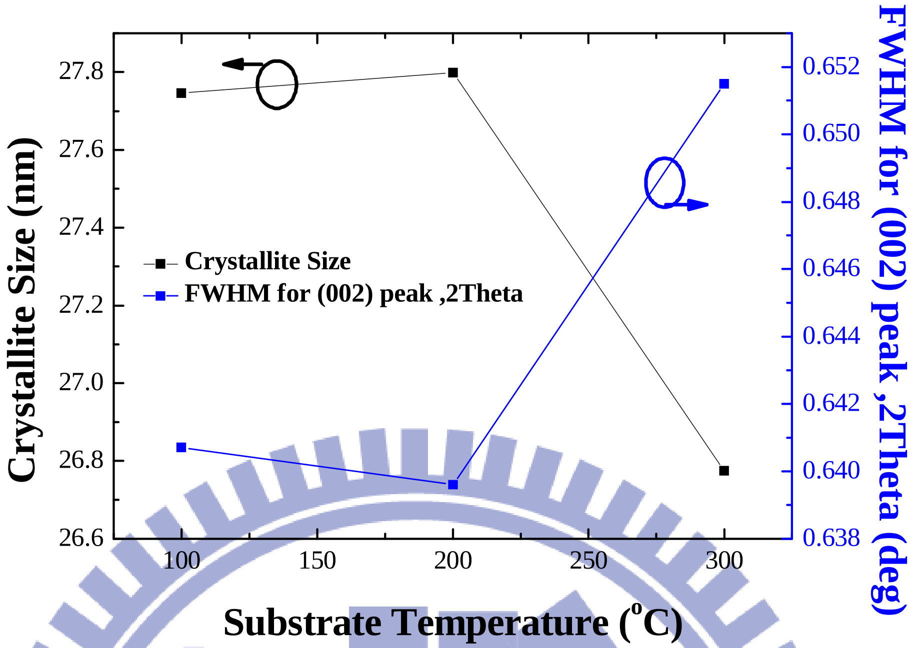

Figure 4-12 Variation of crystallite size and the FWHM for (002) peak of IZO thin films with different substrate temperature.

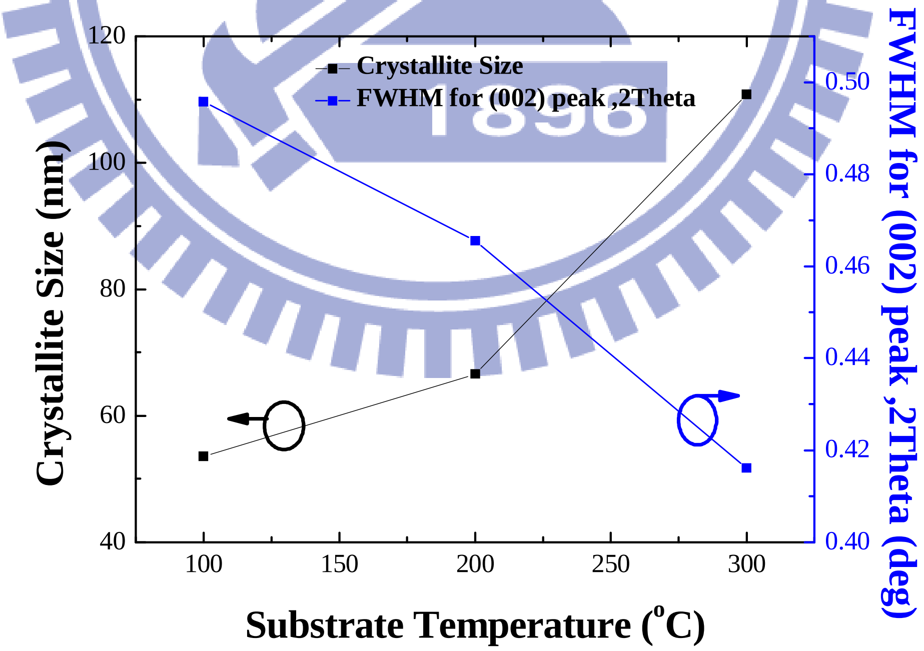

Figure 4-13 Variation of crystallite size and the FWHM for (002) peak of AZO thin films with different substrate temperature.

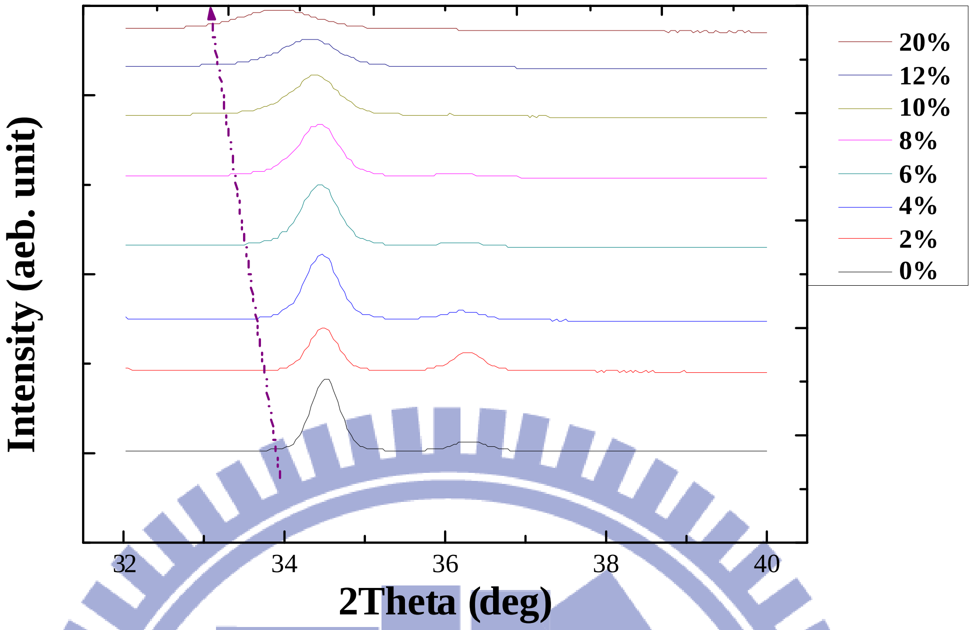

Figure 4-14 Decreasing of the (002) peak position of IZO thin films with different In concentration.

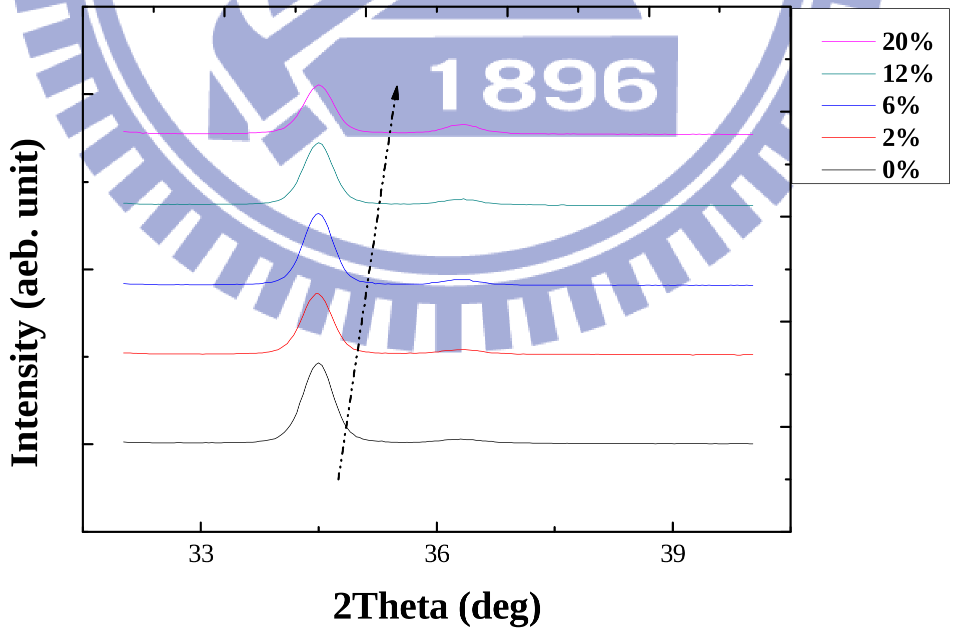

Figure 4-15 Increasing of the (002) peak position of AZO thin films with different Al concentration.

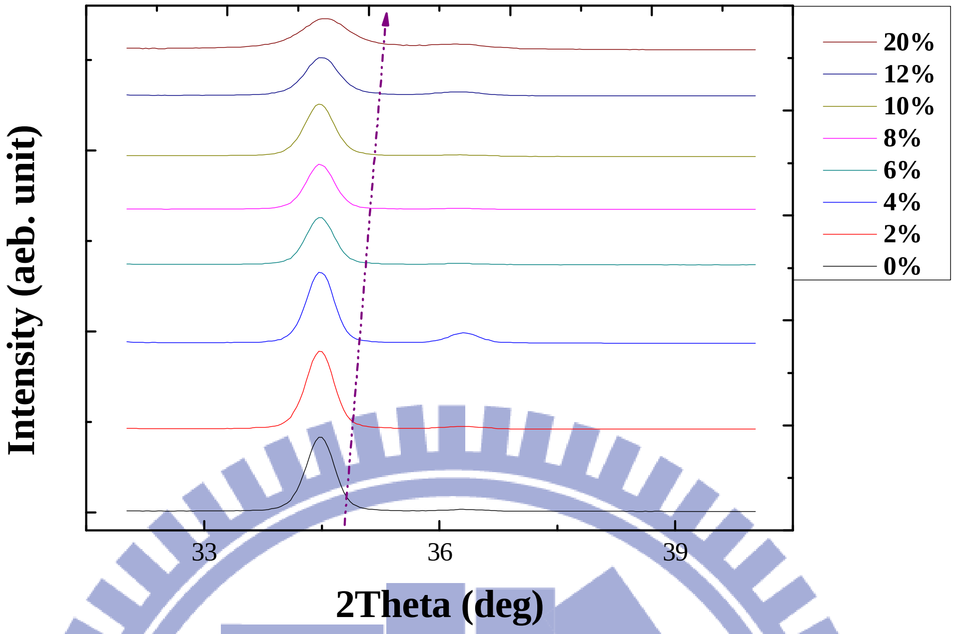

Figure 4-16 Increasing of the (002) peak position of GZO thin films with different Ga concentration.

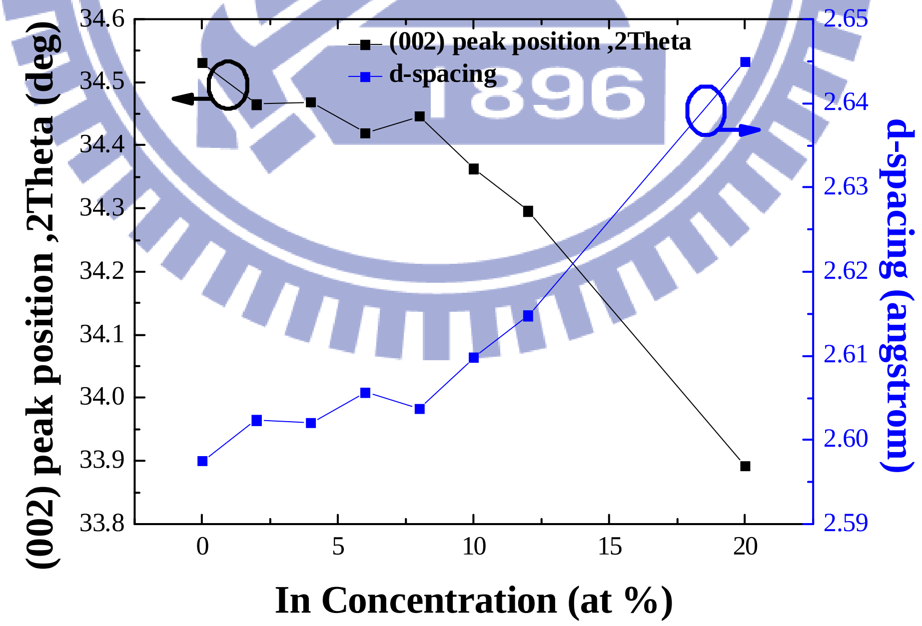

Figure 4-17 Variation of the (002) peak position and the d-spacing of IZO thin films with different In concentration.

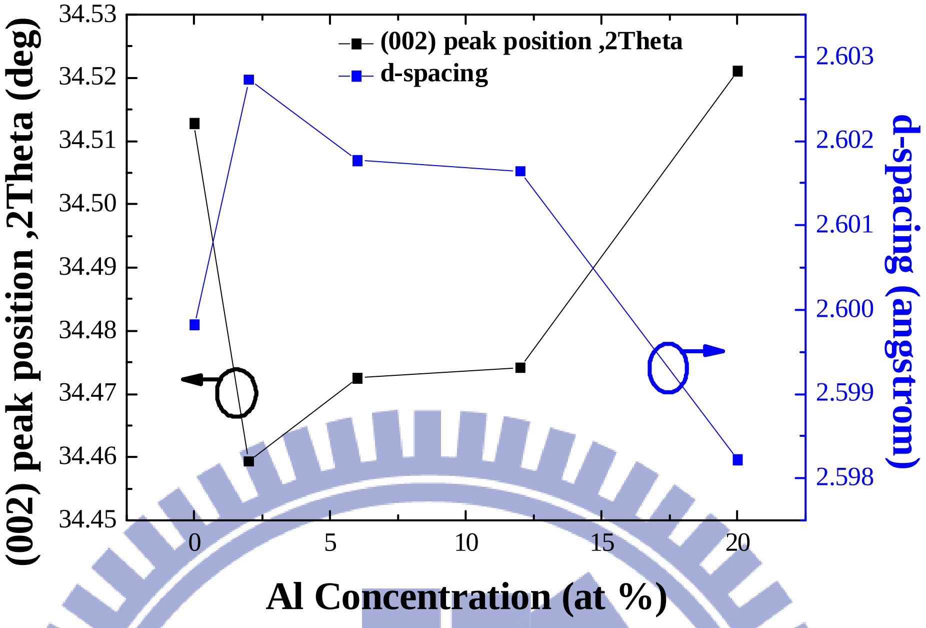

Figure 4-18 Variation of the (002) peak position and the d-spacing of AZO thin films with different Al concentration.

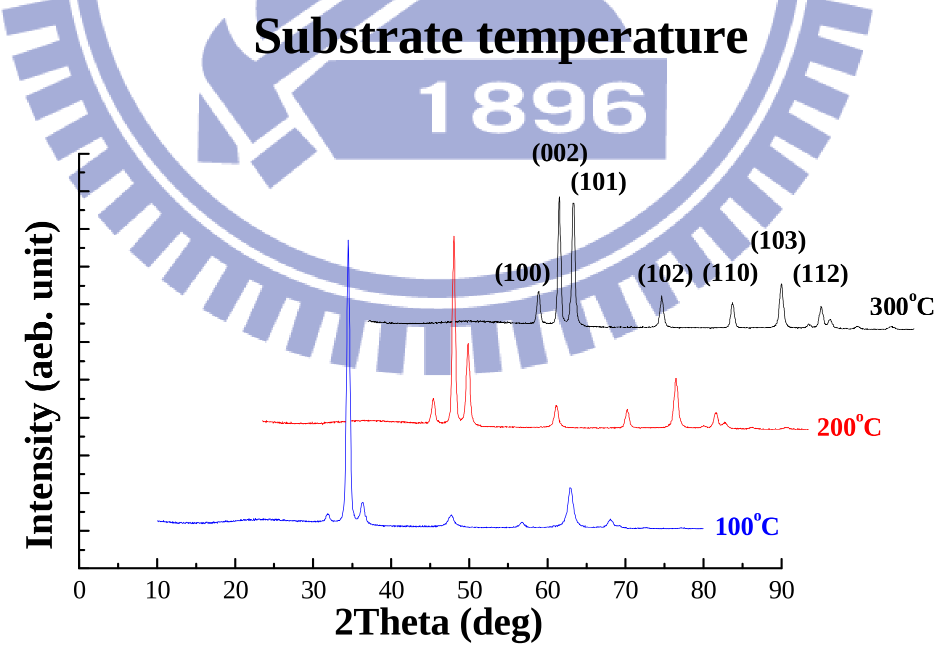

Figure 4-19 GIXRD patterns of AZO thin films deposited with different substrate temperature.

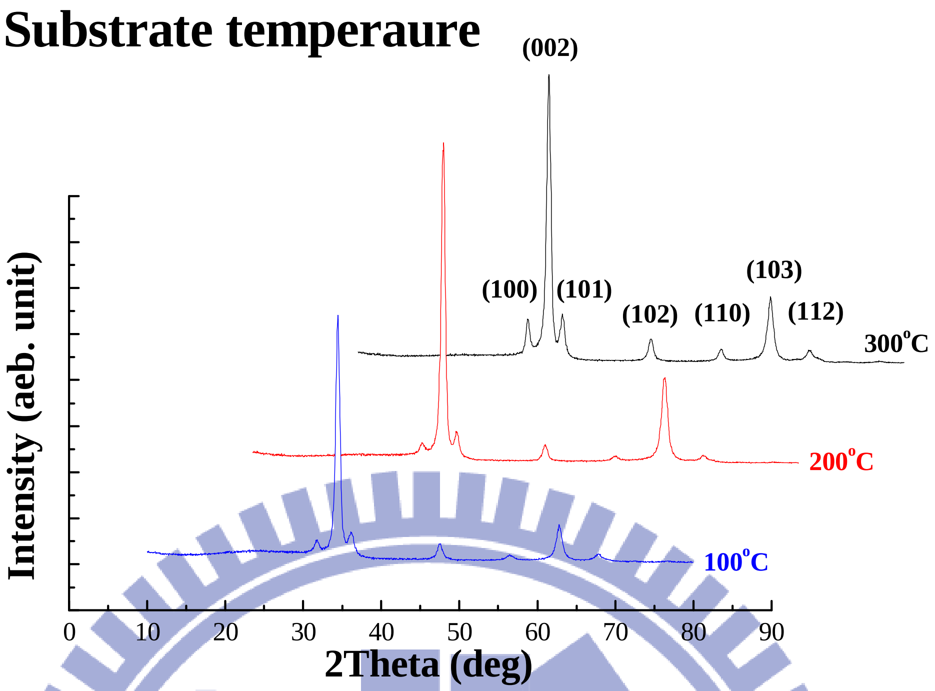

Figure 4-20 GIXRD patterns of IZO thin films deposited with different substrate temperature.

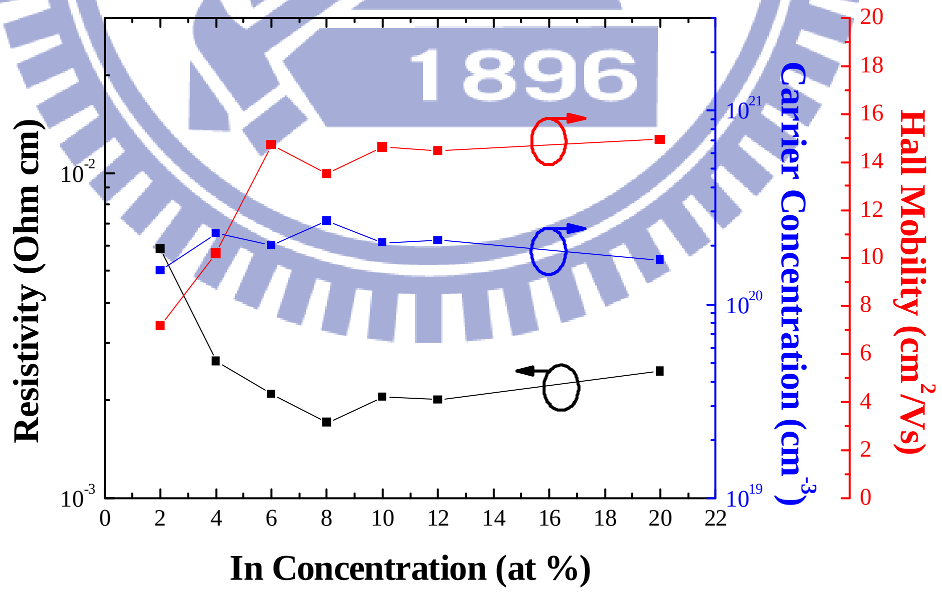

Figure 4-21 Variation of the resistivity, carrier concentration and hall mobility of IZO thin films with different In concentration.

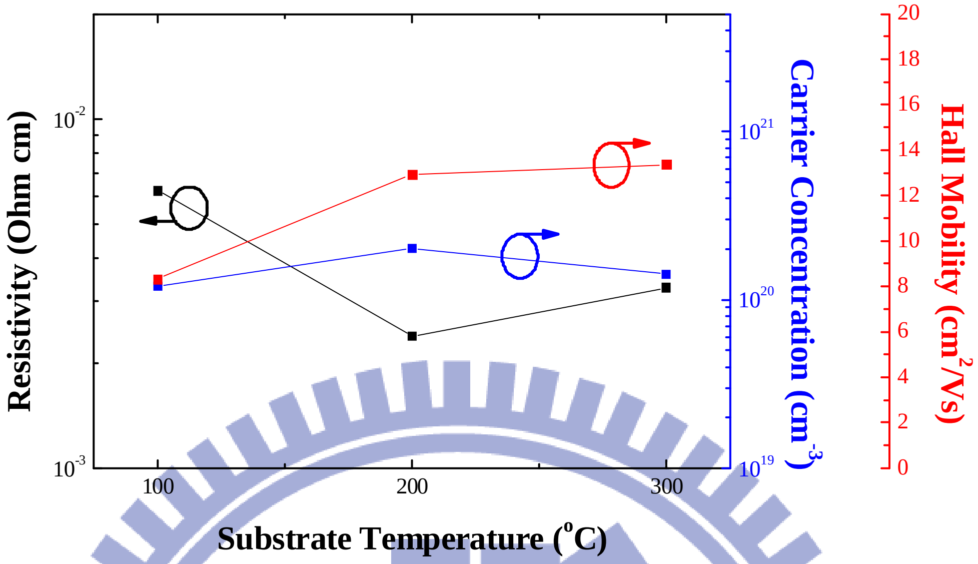

Figure 4-22 Variation of the resistivity, carrier concentration and hall mobility of IZO thin films with different substrate temperature.

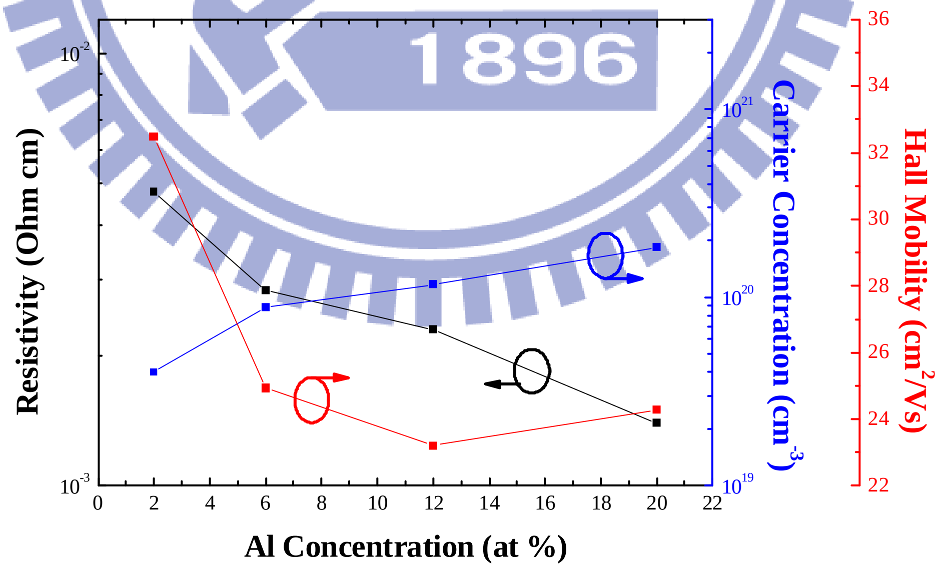

Figure 4-23 Variation of the resistivity, carrier concentration and hall mobility of AZO thin films with different Al concentration.

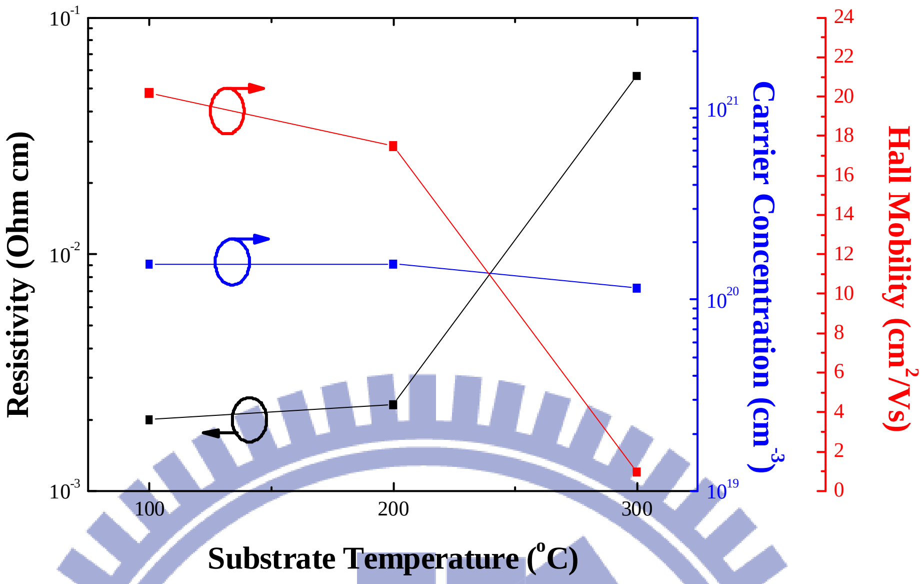

Figure 4-24 Variation of the resistivity, carrier concentration and hall mobility of AZO thin films with different substrate temperature.

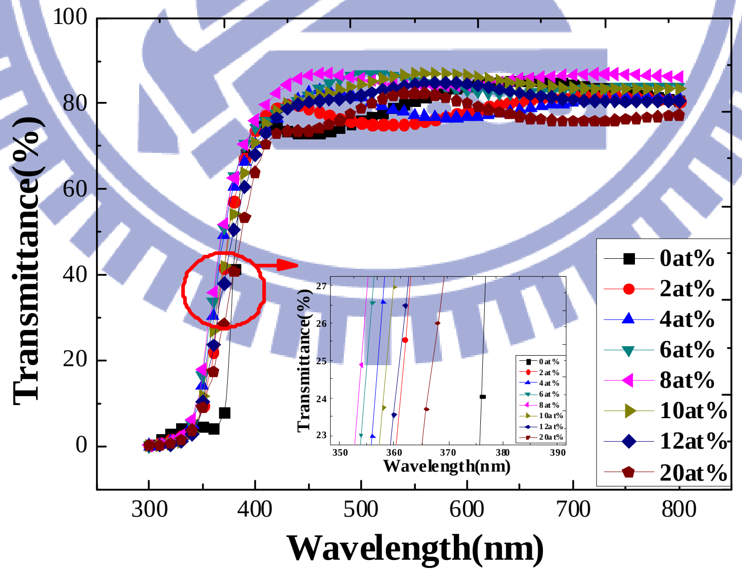

Figure 4-25 The optical transmittance spectra of ZnO and IZO thin films deposited with different In concentration.

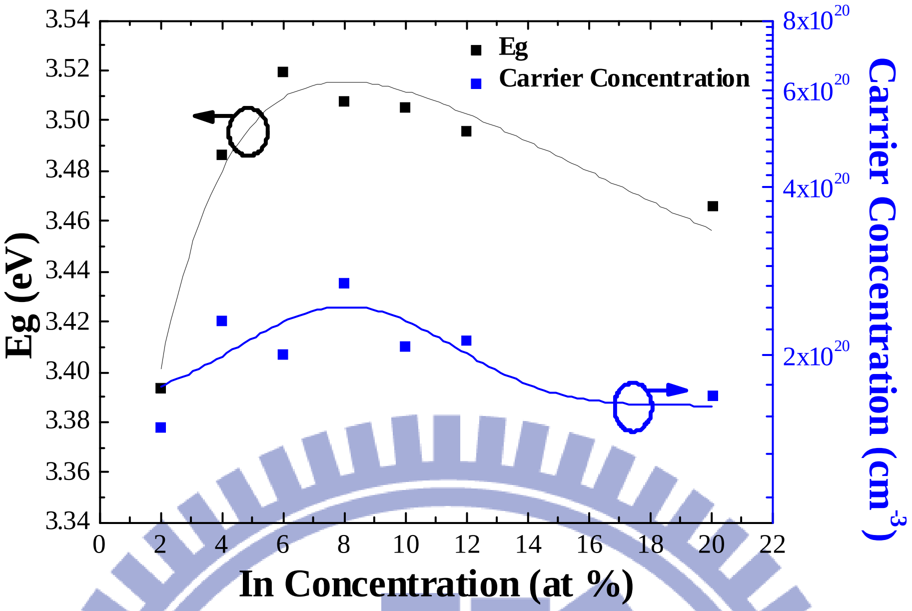

Figure 4-26 Variation of the energy band gap and carrier concentration of IZO thin films with different In concentration.

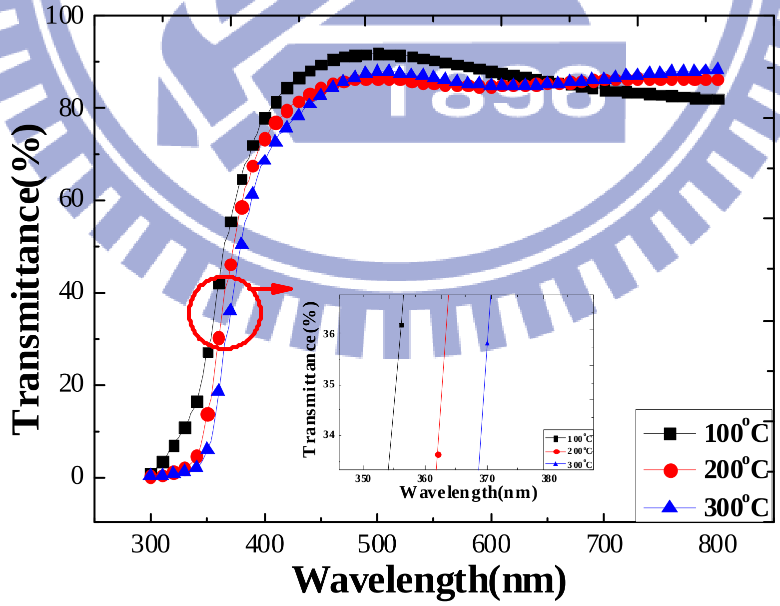

Figure 4-27 The optical transmittance spectra of IZO thin films deposited with different substrate temperature.

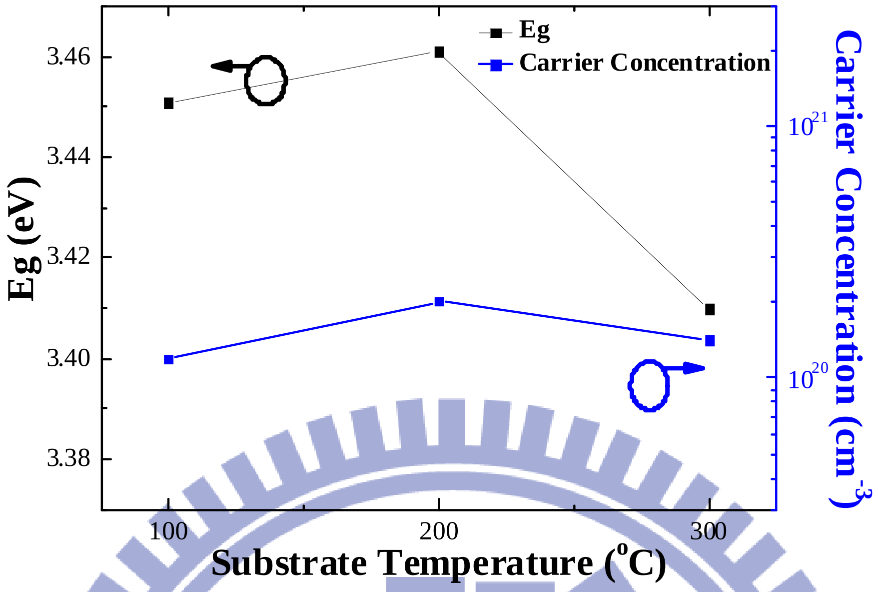

Figure 4-28 Variation of the energy band gap and carrier concentration of IZO thin films with different substrate temperature.

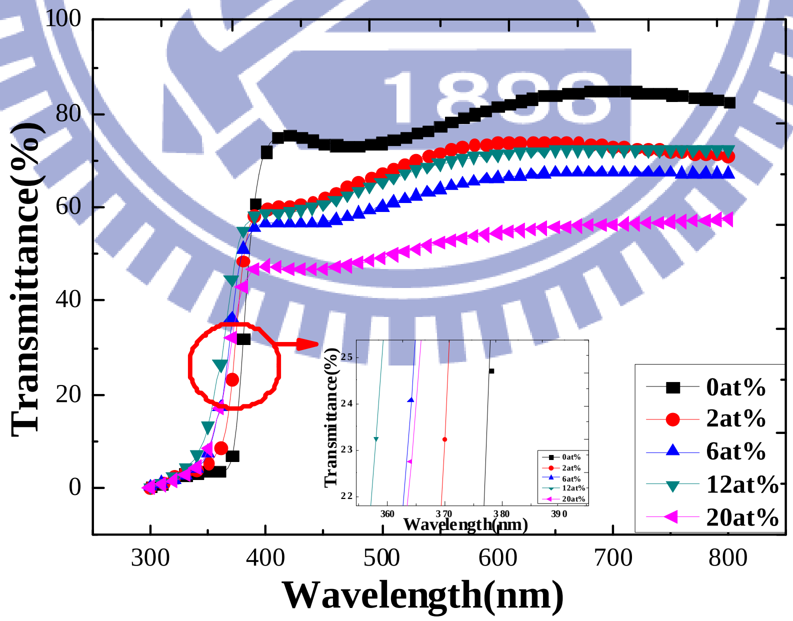

Figure 4-29 The optical transmittance spectra of ZnO and AZO thin films deposited with different Al concentration.

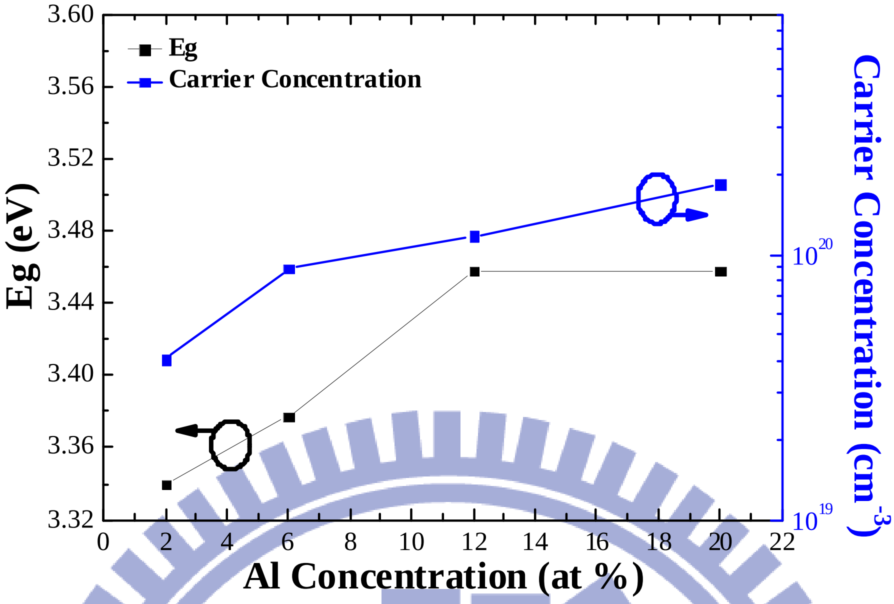

Figure 4-30 Variation of the energy band gap and carrier concentration of AZO thin films with different Al concentration.

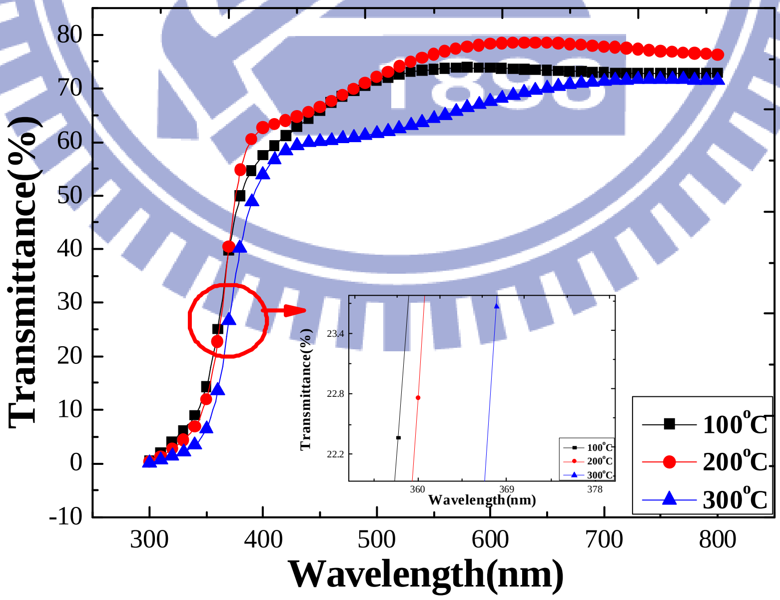

Figure 4-31 The optical transmittance spectra of AZO thin films deposited with different substrate temperature.

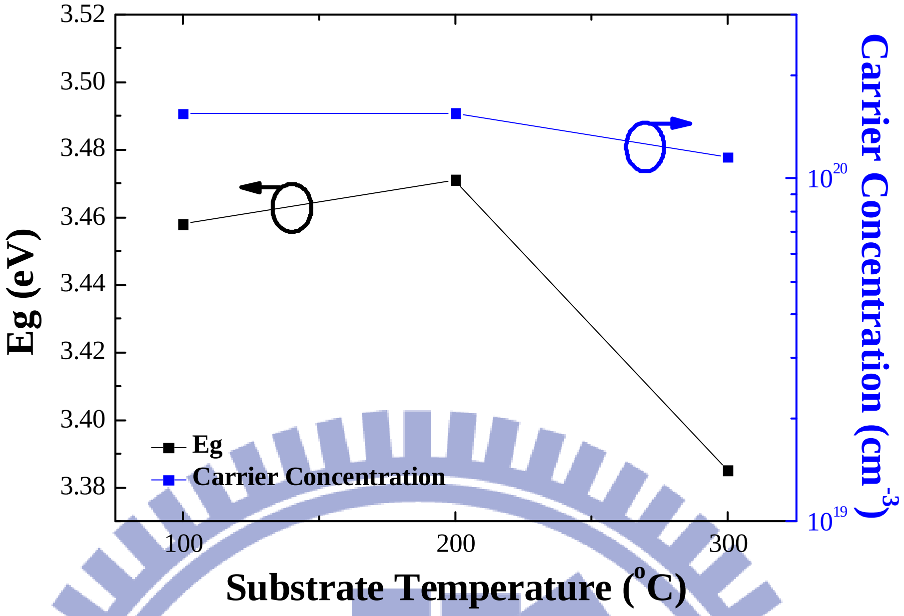

Figure 4-32 Variation of the energy band gap and carrier concentration of AZO thin films with different substrate temperature.

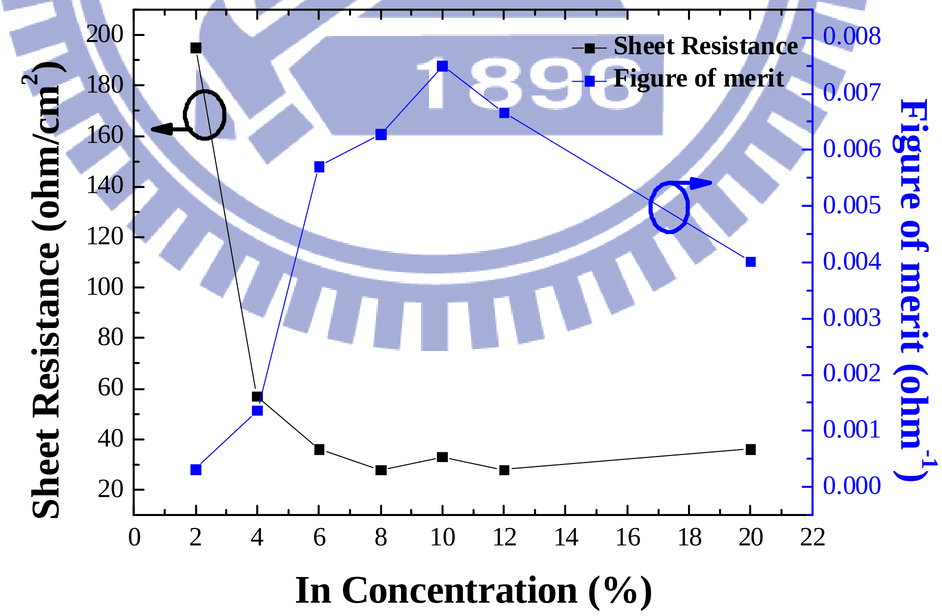

Figure 4-33 Variation of the sheet resistance and figure of merit of IZO thin films with different doping concentration.

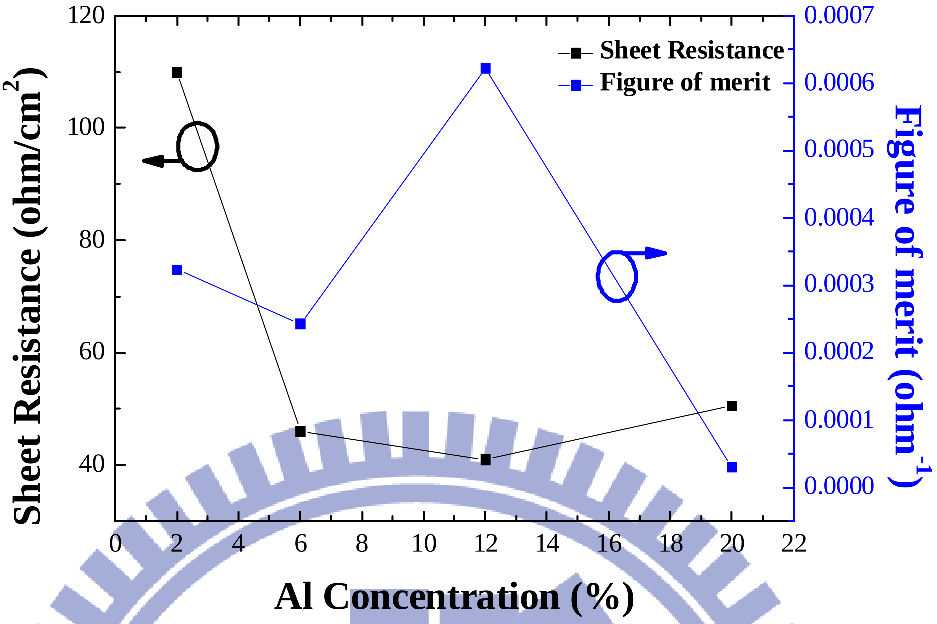

Figure 4-34 Variation of the sheet resistance and figure of merit of AZO thin films with different doping concentration.

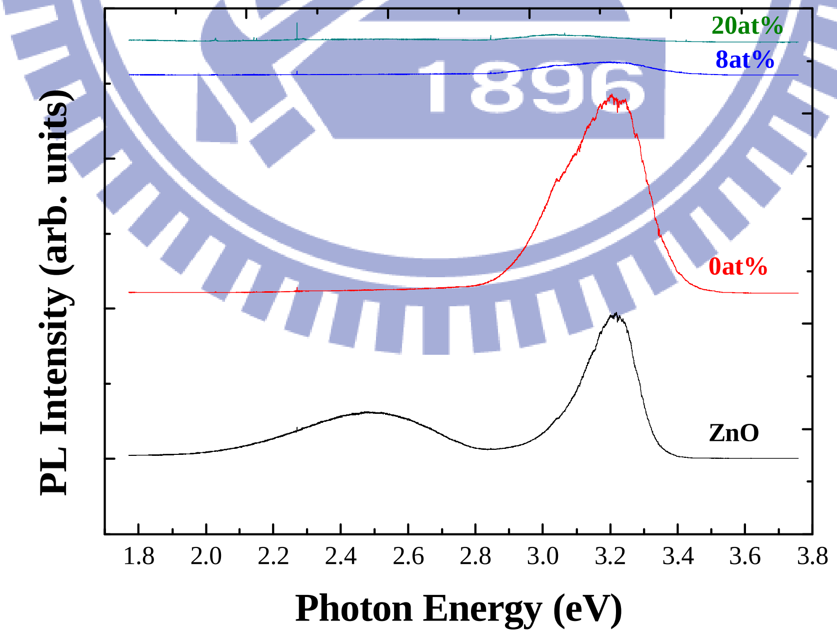

Figure 4-35 PL emission spectra of ZnO and IZO thin films with different doping concentration at 324nm excitation.

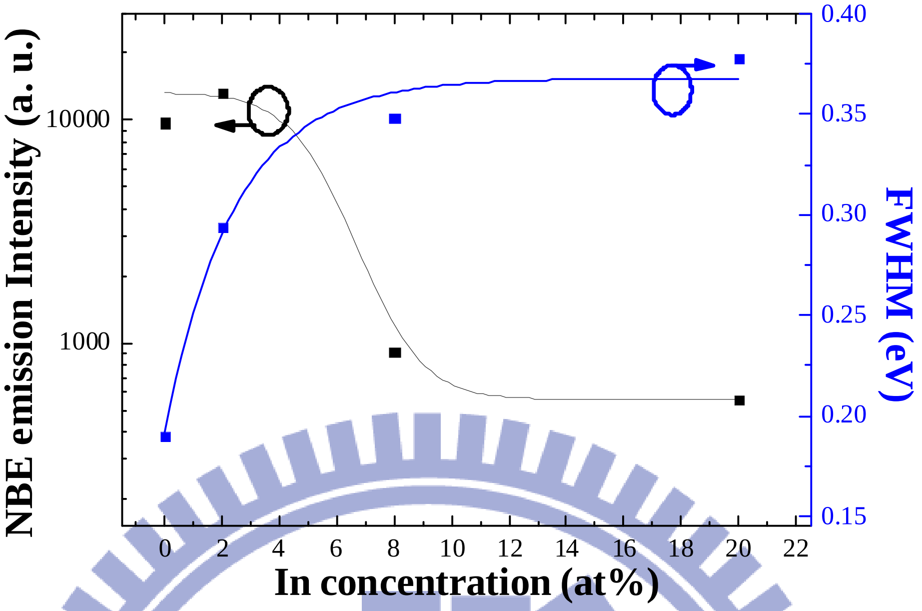

Figure 4-36 Variation of the NBE emission intensity and its FWHM value of IZO thin films with different doping concentration.

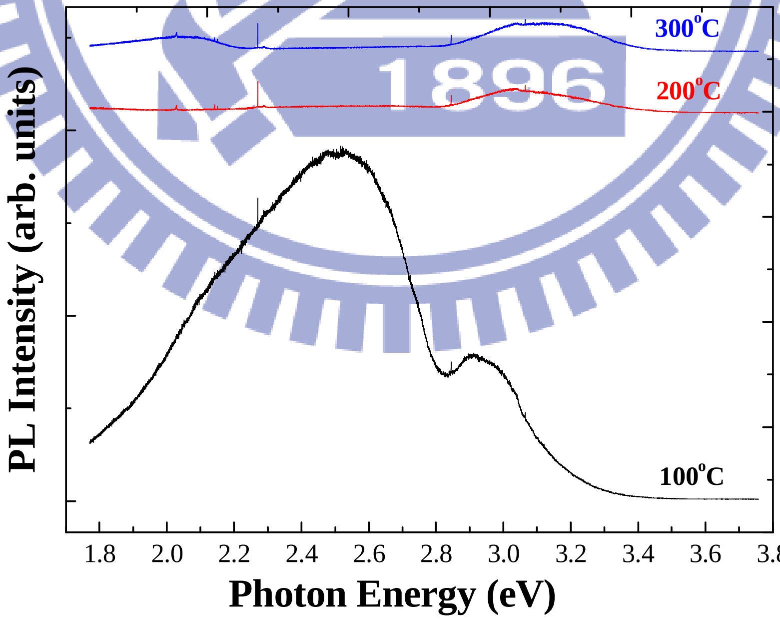

Figure 4-37 PL emission spectra of IZO thin films with different substrate temperature at 324nm excitation.

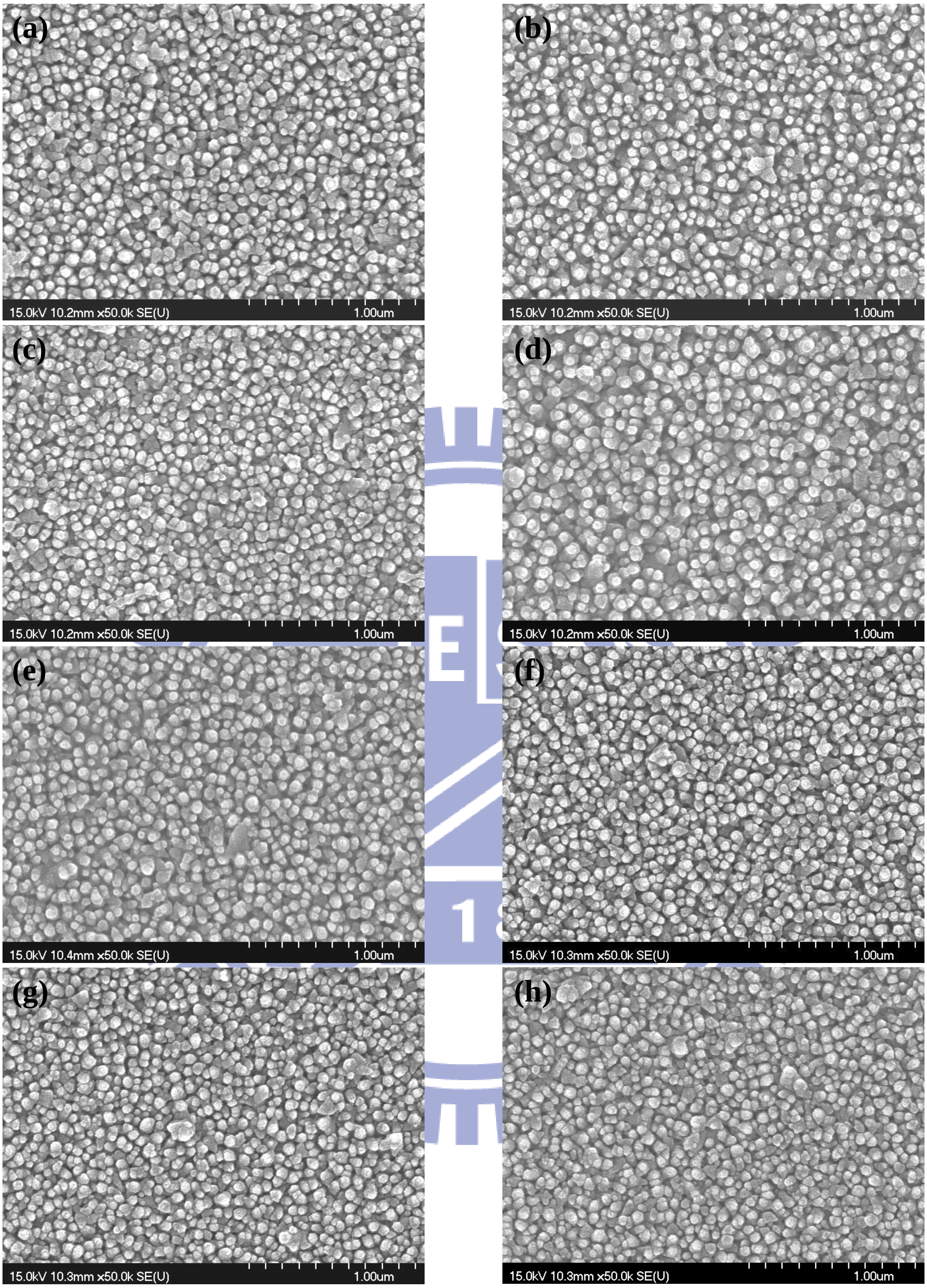
(a)
15.0kV 10.2mm x50.0k SE(U)
1.00um
(b)
15.0kV 10.2mm x50.0k SE(U)
1.00um
(c)
15.0kV 10.2mm x50.0k SE(U)
1.00um
(d)
15.0kV 10.2mm x50.0k SE(U)
1.00um
(e)
15.0kV 10.4mm x50.0k SE(U)
1.00um
(f)
15.0kV 10.3mm x50.0k SE(U)
1.00um
(g)
15.0kV 10.3mm x50.0k SE(U)
1.00um
(h)
15.0kV 10.3mm x50.0k SE(U)
1.00um

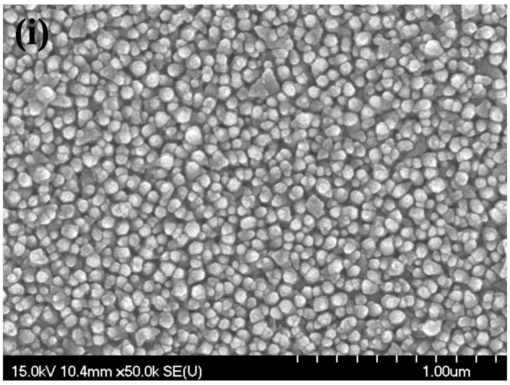

Figure 4-38 SEM images of deposited IZO thin films which is annealed with different treatment condition (a) Control; (b) 200°C (c) 300°C (d) 400°C (e) 500°C in oxygen ambient; (f) 200°C (g) 300°C (h) 400°C (i) 500°C in nitrogen ambient.

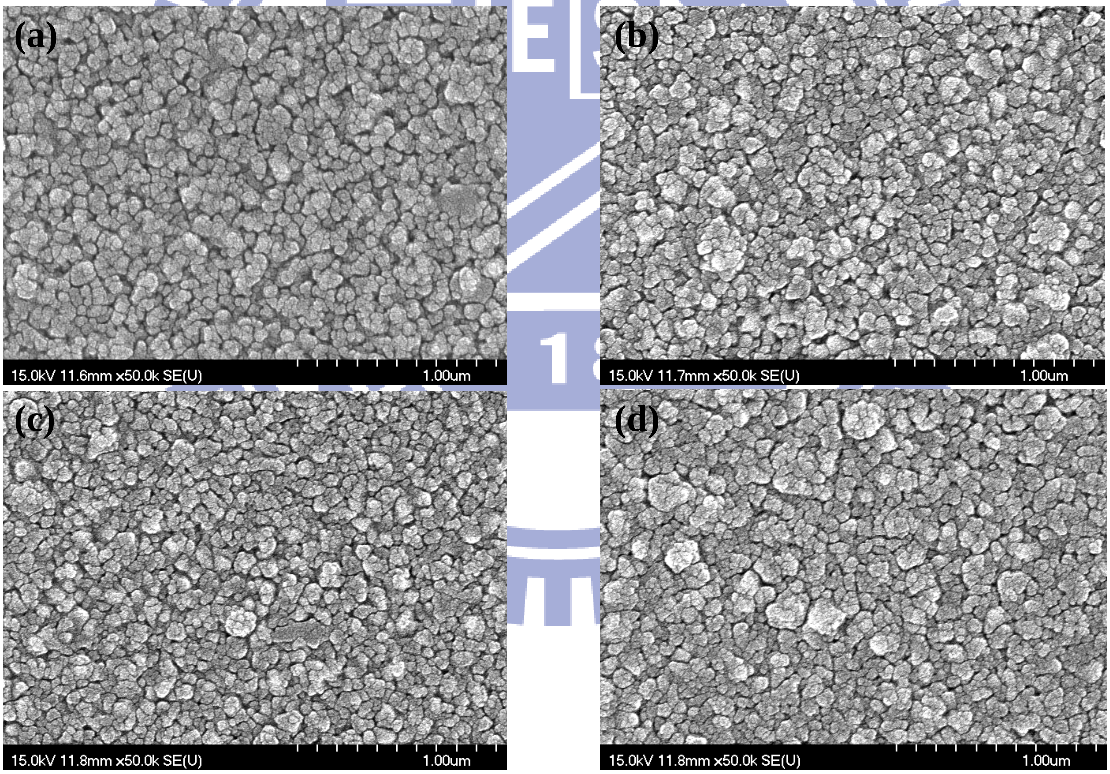

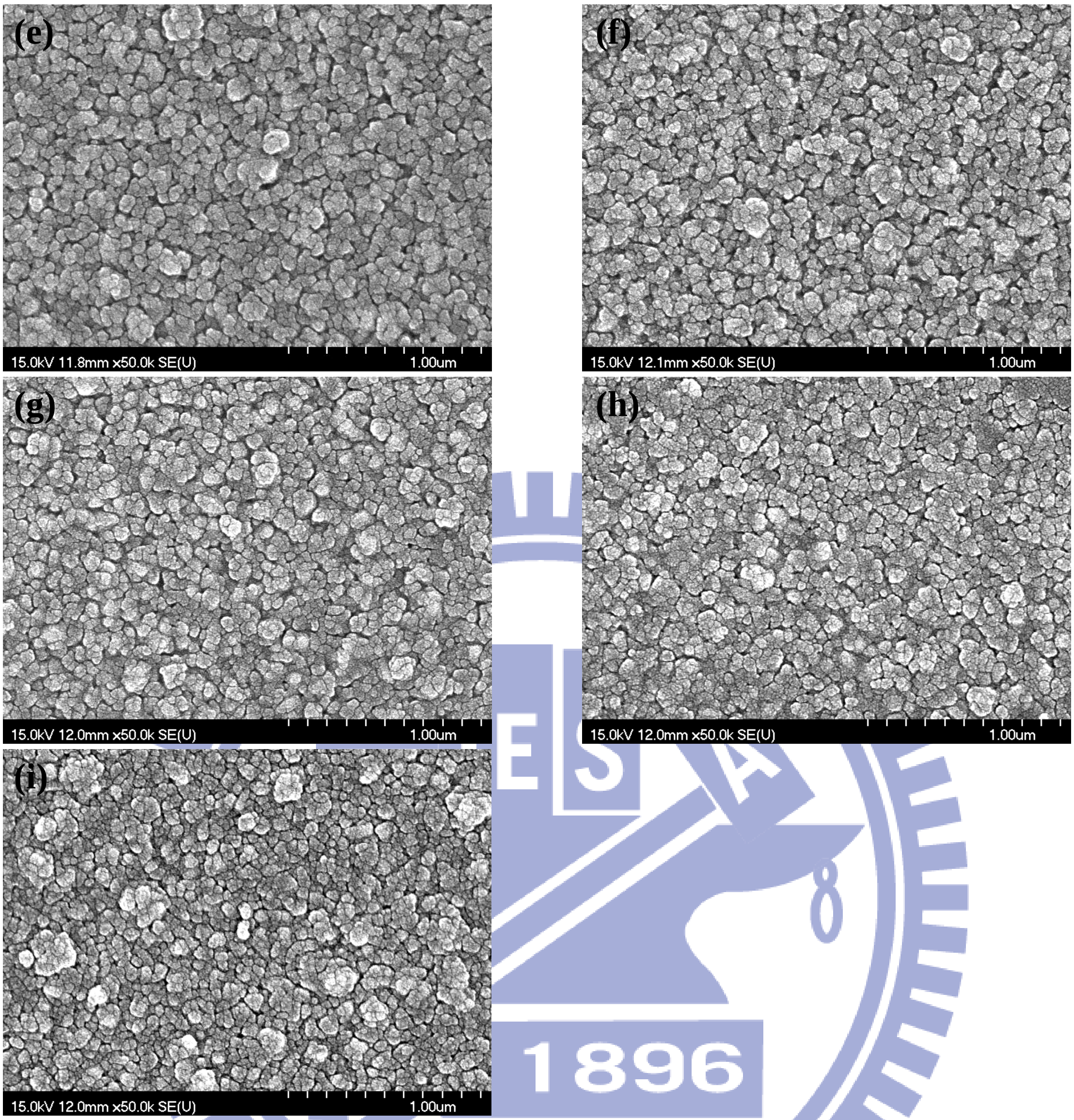

Figure 4-39 SEM images of deposited GZO thin films which is annealed with different treatment condition (a) Control; (b) 200°C (c) 300°C (d) 400°C (e) 500°C in oxygen ambient; (f) 200°C (g) 300°C (h) 400°C (i) 500°C in nitrogen ambient.

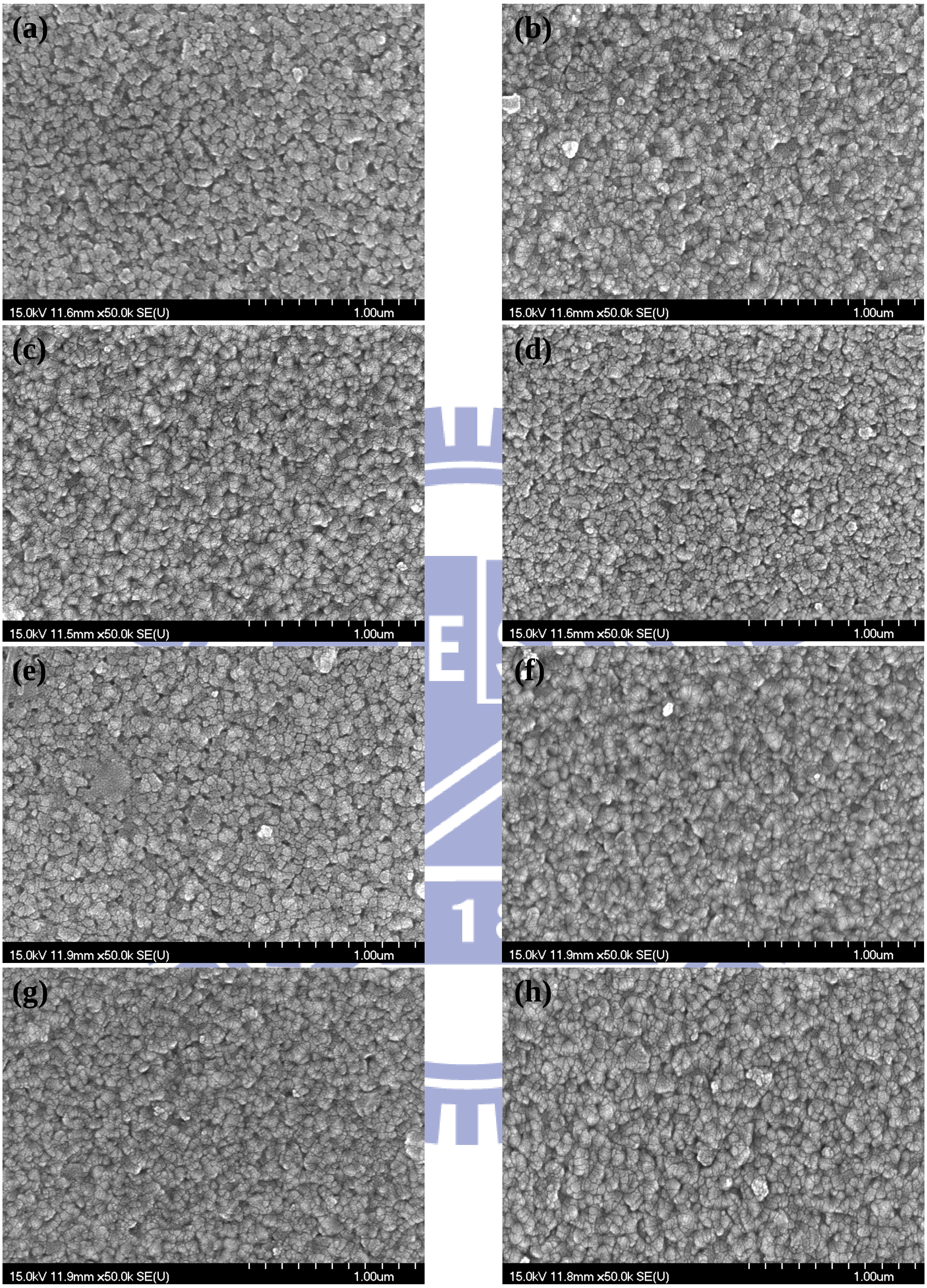
(a)
15.0kV 11.6mm x50.0k SE(U)
1.00um
(b)
15.0kV 11.6mm x50.0k SE(U)
1.00um
(c)
15.0kV 11.5mm x50.0k SE(U)
1.00um
(d)
15.0kV 11.5mm x50.0k SE(U)
1.00um
(e)
15.0kV 11.9mm x50.0k SE(U)
1.00um
(f)
15.0kV 11.9mm x50.0k SE(U)
1.00um
(g)
15.0kV 11.9mm x50.0k SE(U)
1.00um
(h)
15.0kV 11.8mm x50.0k SE(U)
1.00um

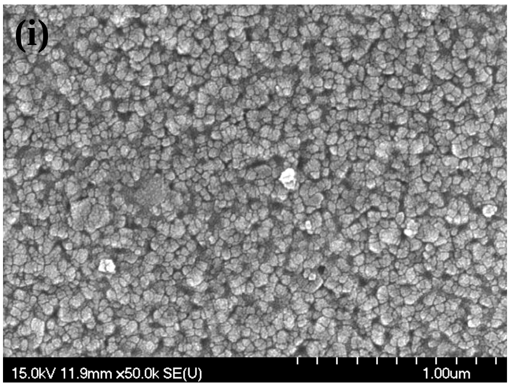

Figure 4-40 SEM images of deposited ZnO thin films which is annealed with different treatment condition (a) Control; (b) 200°C (c) 300°C (d) 400°C (e) 500°C in oxygen ambient; (f) 200°C (g) 300°C (h) 400°C (i) 500°C in nitrogen ambient.

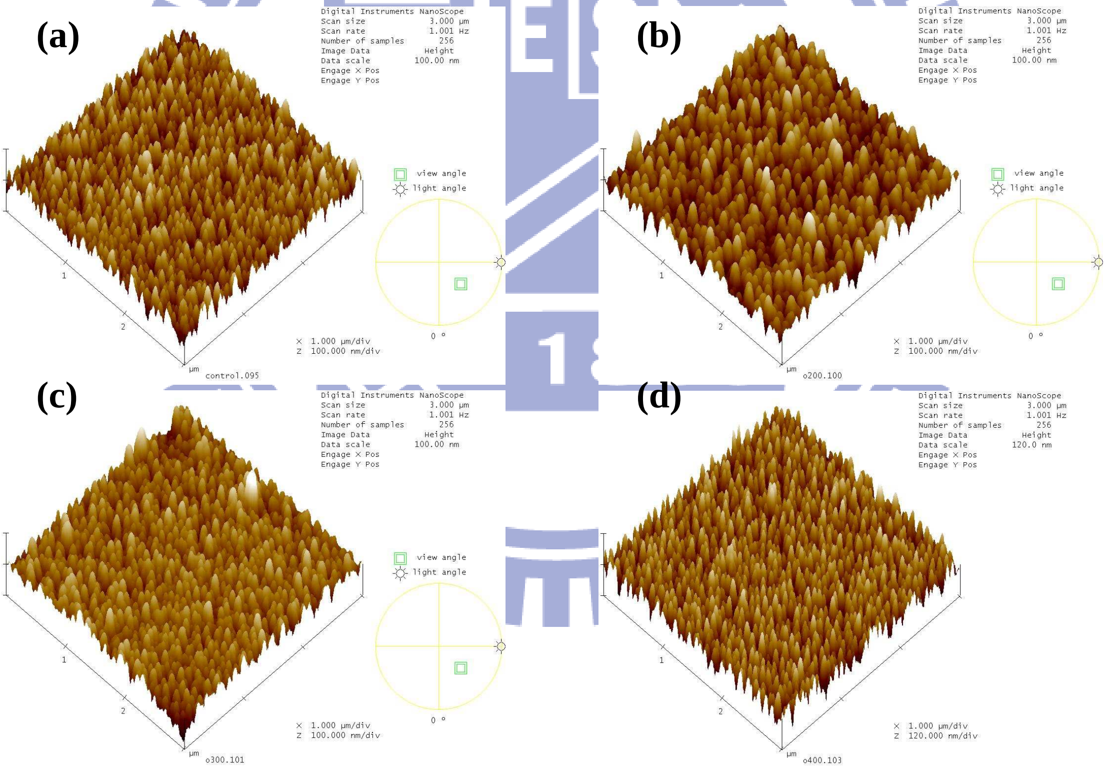

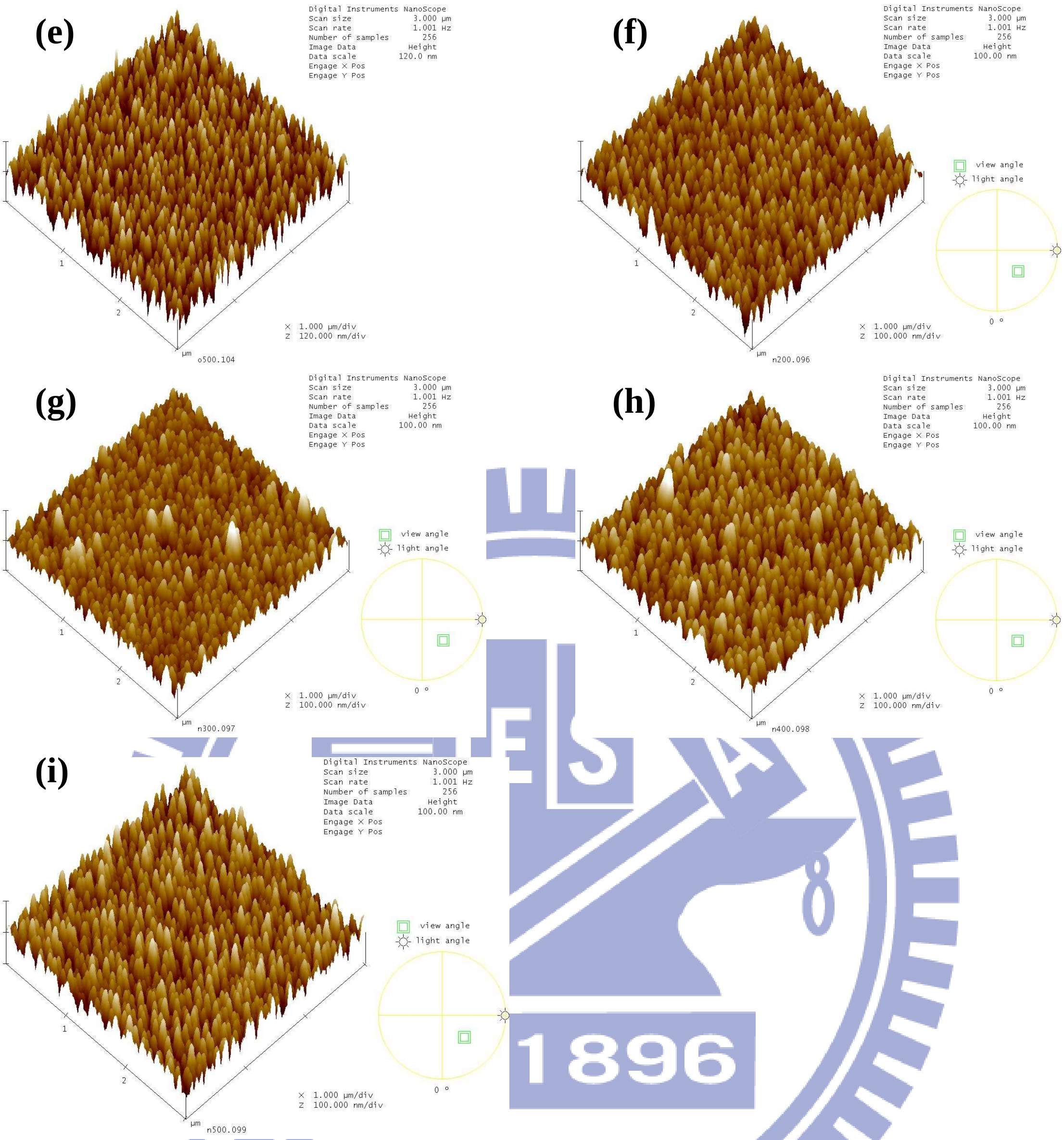

Figure 4-41 AFM images of deposited IZO thin films which is annealed with different treatment condition (a) Control; (b) 200^{o}C (c) 300^{o}C (d) 400^{o}C (e) 500^{o}C in oxygen ambient; (f) 200^{o}C (g) 300^{o}C (h) 400^{o}C (i) 500^{o}C in nitrogen ambient.

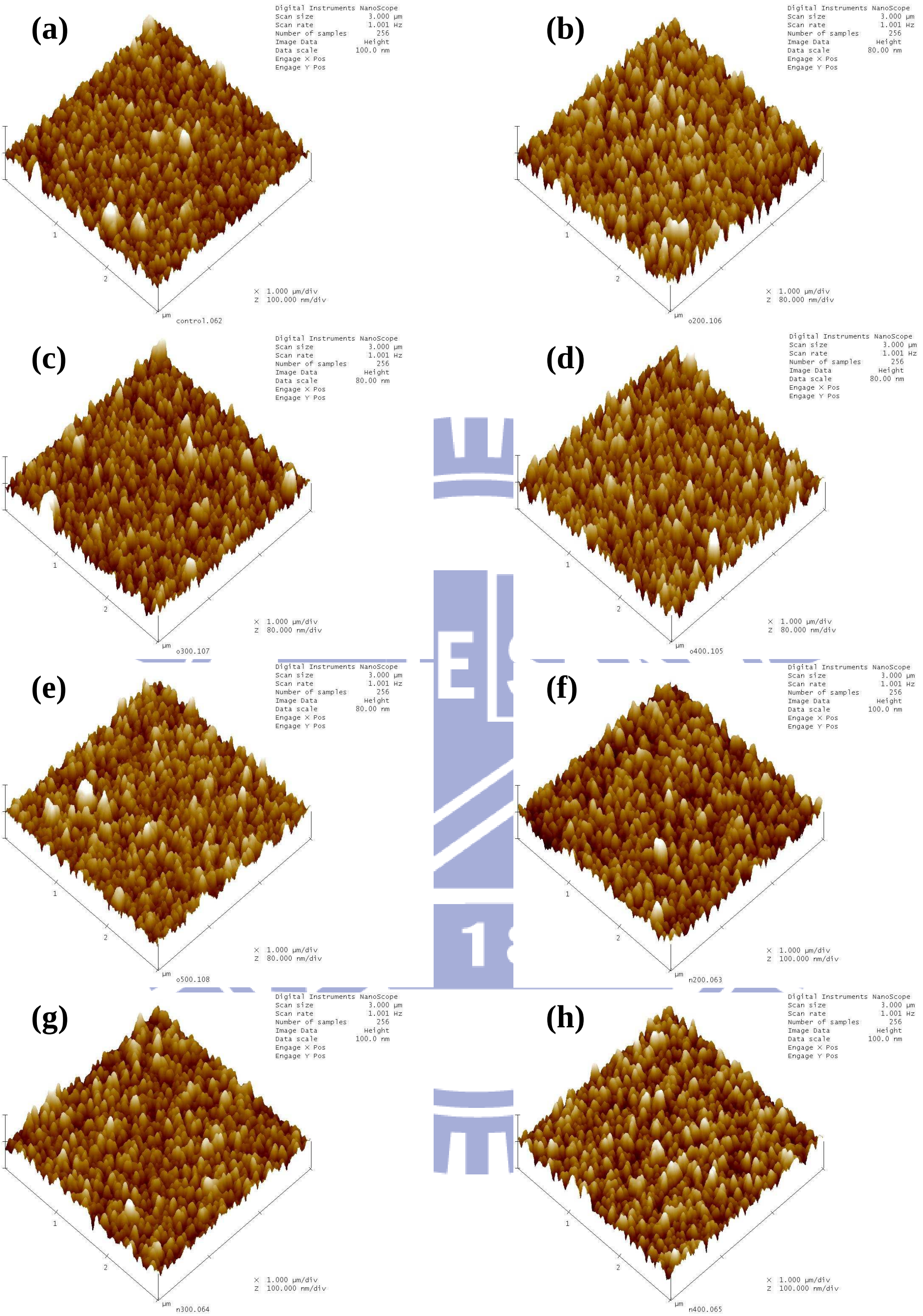(a)
Digital Instruments NanoScope
Scan size 3.000 µm
Scan rate 1.001 Hz
Number of samples 256
Image Data Height
Data scale 100.0 nm
Engage X Pos
Engage Y Pos
1
2
µm
X 1.000 µm/div
Z 100.000 nm/div
control.062
(b)
Digital Instruments NanoScope
Scan size 3.000 µm
Scan rate 1.001 Hz
Number of samples 256
Image Data Height
Data scale 80.00 nm
Engage X Pos
Engage Y Pos
1
2
µm
X 1.000 µm/div
Z 80.000 nm/div
o200.106
(c)
Digital Instruments NanoScope
Scan size 3.000 µm
Scan rate 1.001 Hz
Number of samples 256
Image Data Height
Data scale 80.00 nm
Engage X Pos
Engage Y Pos
1
2
µm
X 1.000 µm/div
Z 80.000 nm/div
o300.107
(d)
Digital Instruments NanoScope
Scan size 3.000 µm
Scan rate 1.001 Hz
Number of samples 256
Image Data Height
Data scale 80.00 nm
Engage X Pos
Engage Y Pos
1
2
µm
X 1.000 µm/div
Z 80.000 nm/div
o400.105
(e)
Digital Instruments NanoScope
Scan size 3.000 µm
Scan rate 1.001 Hz
Number of samples 256
Image Data Height
Data scale 80.00 nm
Engage X Pos
Engage Y Pos
1
2
µm
X 1.000 µm/div
Z 80.000 nm/div
o500.108
(f)
Digital Instruments NanoScope
Scan size 3.000 µm
Scan rate 1.001 Hz
Number of samples 256
Image Data Height
Data scale 100.0 nm
Engage X Pos
Engage Y Pos
1
2
µm
X 1.000 µm/div
Z 100.000 nm/div
n200.063
(g)
Digital Instruments NanoScope
Scan size 3.000 µm
Scan rate 1.001 Hz
Number of samples 256
Image Data Height
Data scale 100.0 nm
Engage X Pos
Engage Y Pos
1
2
µm
X 1.000 µm/div
Z 100.000 nm/div
n300.064
(h)
Digital Instruments NanoScope
Scan size 3.000 µm
Scan rate 1.001 Hz
Number of samples 256
Image Data Height
Data scale 100.0 nm
Engage X Pos
Engage Y Pos
1
2
µm
X 1.000 µm/div
Z 100.000 nm/div
n400.065

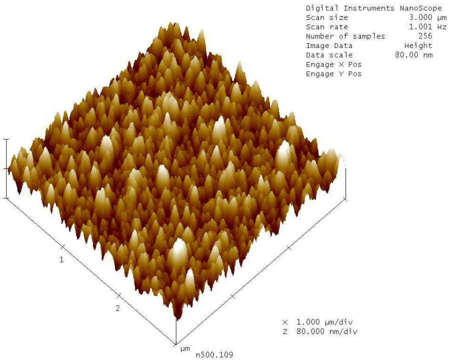

Figure 4-42 AFM images of deposited GZO thin films which is annealed with different treatment condition (a) Control; (b) 200°C (c) 300°C (d) 400°C (e) 500°C in oxygen ambient; (f) 200°C (g) 300°C (h) 400°C (i) 500°C in nitrogen ambient.

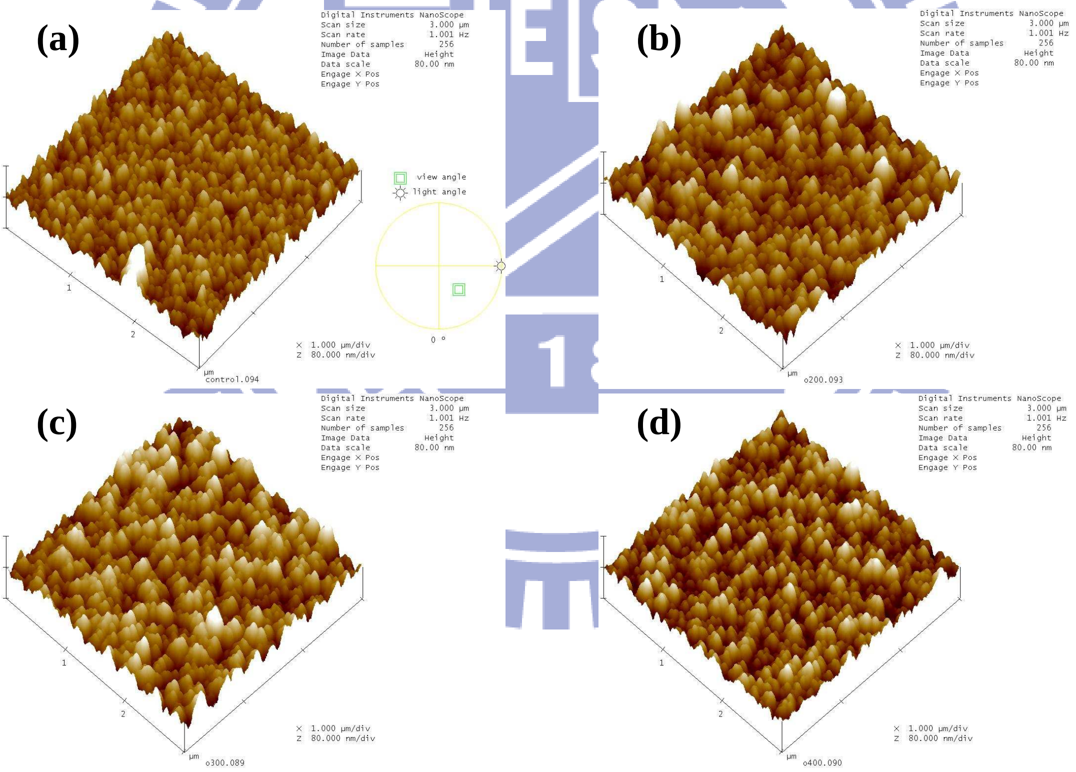

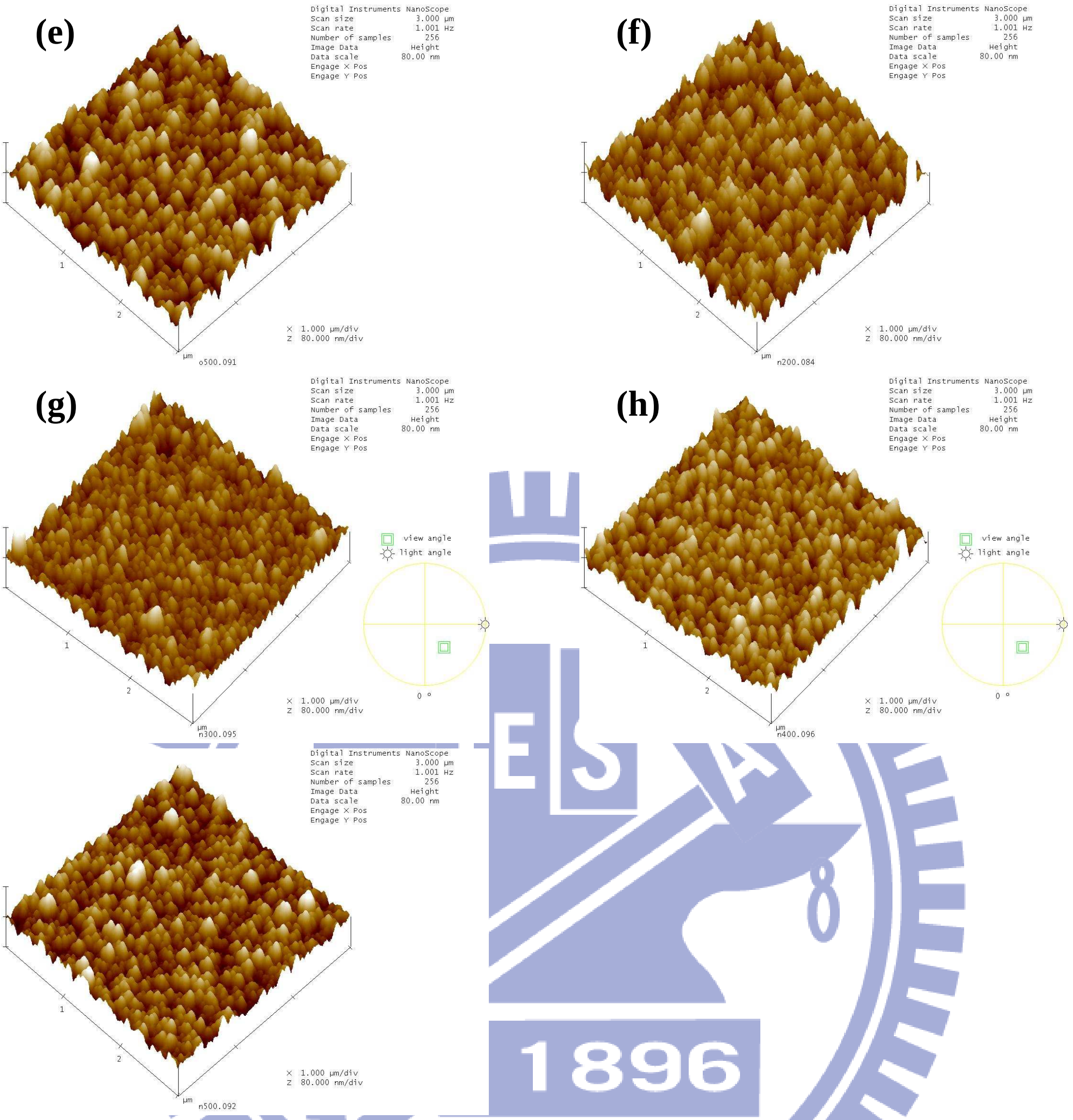

Figure 4-43 AFM images of deposited ZnO thin films which is annealed with different treatment condition (a) Control; (b) 200^{o}C (c) 300^{o}C (d) 400^{o}C (e) 500^{o}C in oxygen ambient; (f) 200^{o}C (g) 300^{o}C (h) 400^{o}C (i) 500^{o}C in nitrogen ambient.

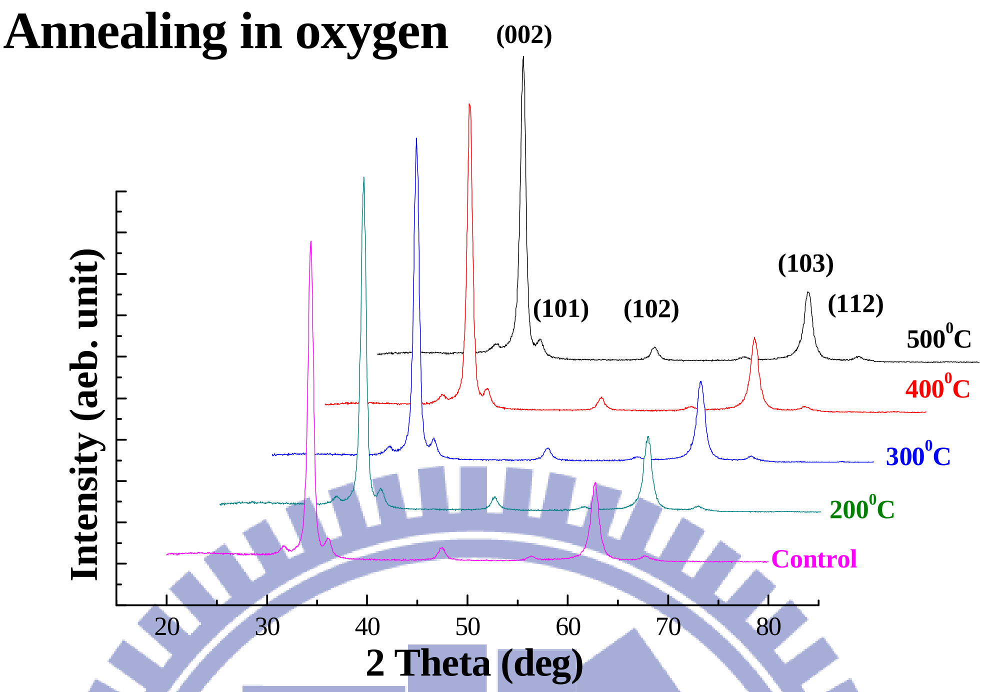

Figure 4-44 GIXRD patterns of IZO thin films annealing with different temperature at oxygen ambient.

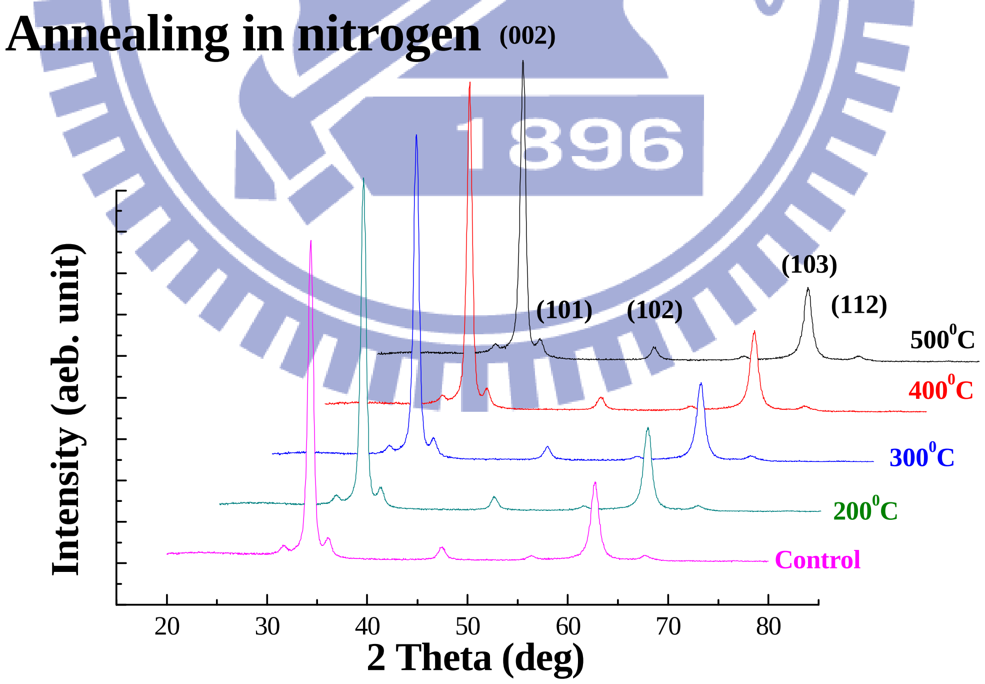

Figure 4-45 GIXRD patterns of IZO thin films annealing with different temperature at nitrogen ambient.

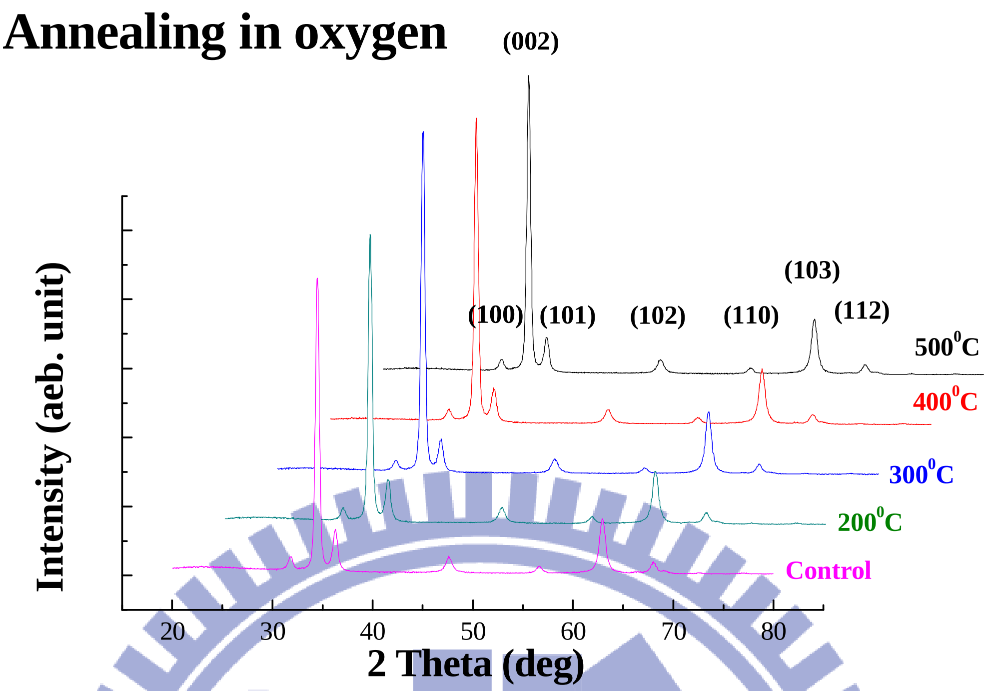

Figure 4-46 GIXRD patterns of GZO thin films annealing with different temperature at oxygen ambient.

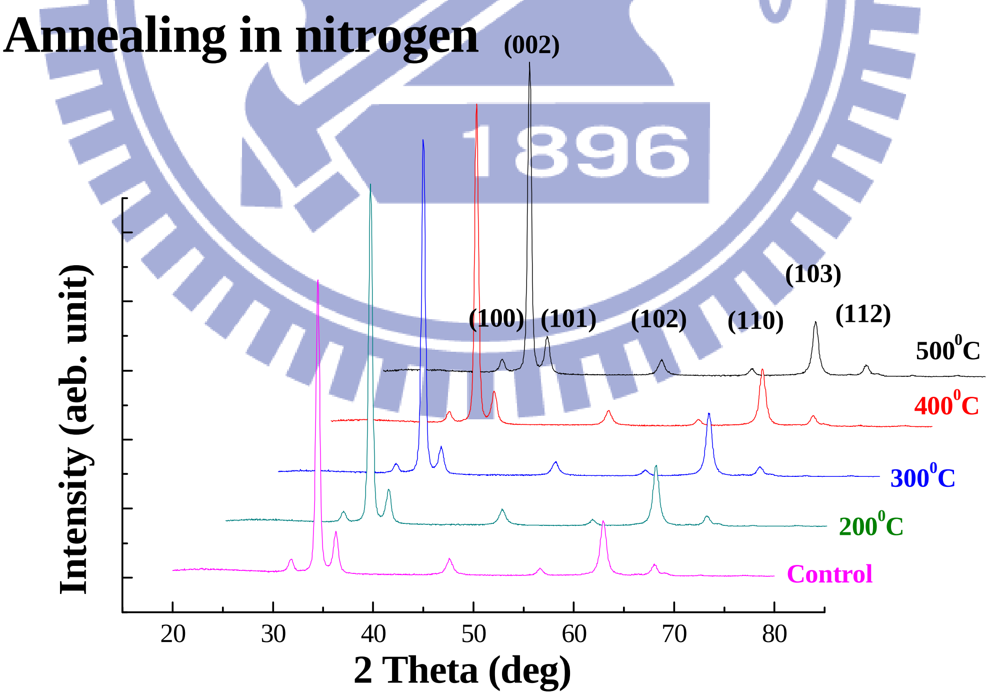

Figure 4-47 GIXRD patterns of GZO thin films annealing with different temperature at nitrogen ambient.

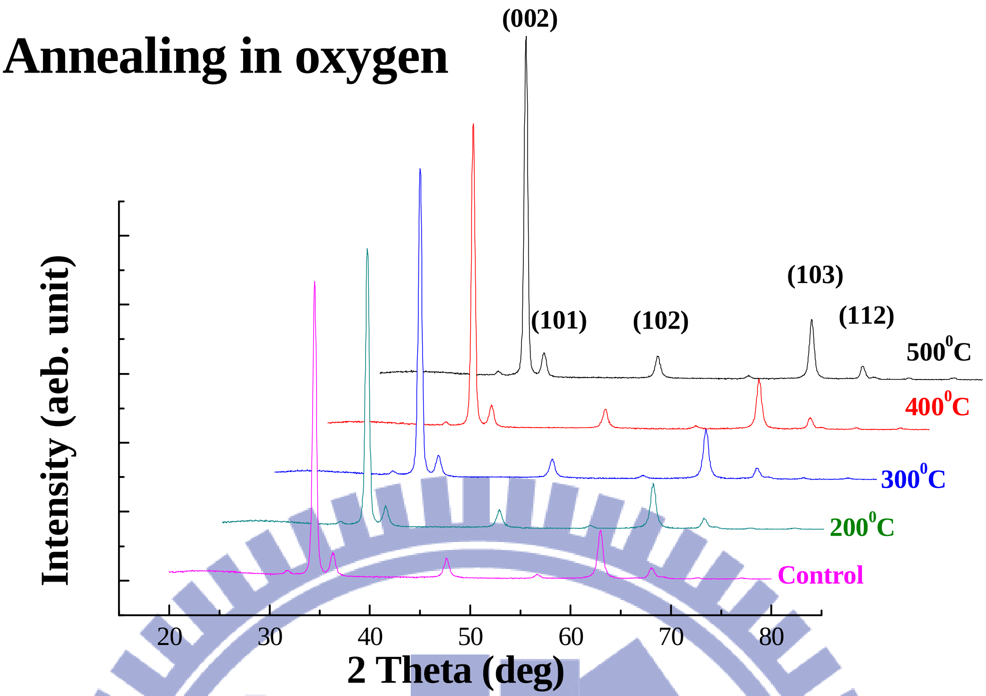

Figure 4-48 GIXRD patterns of ZnO thin films annealing with different temperature at oxygen ambient.

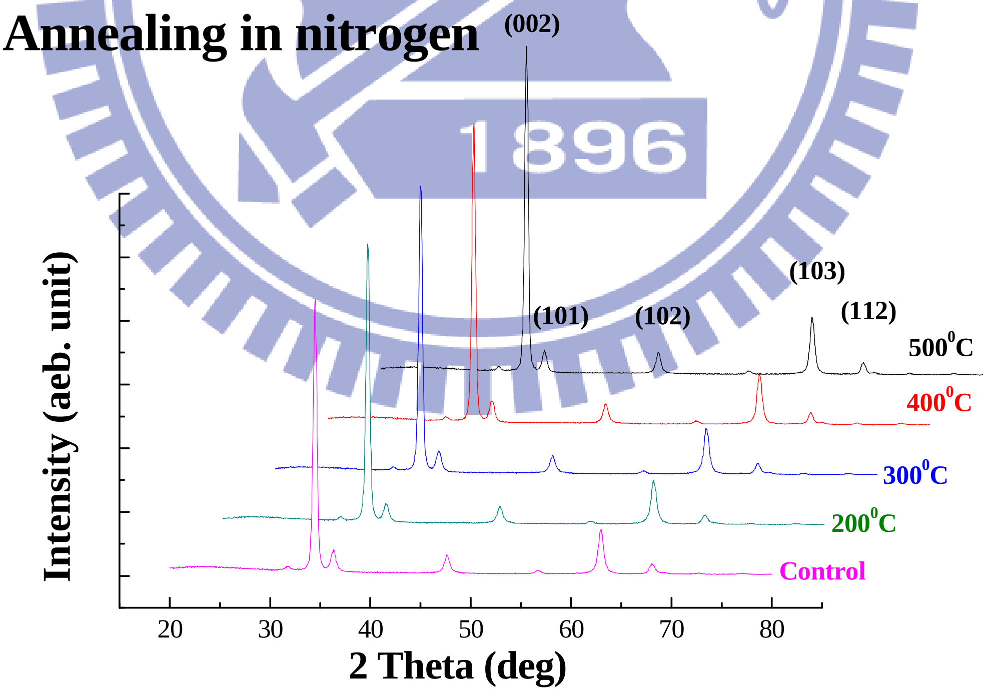

Figure 4-49 GIXRD patterns of ZnO thin films annealing with different temperature at nitrogen ambient.

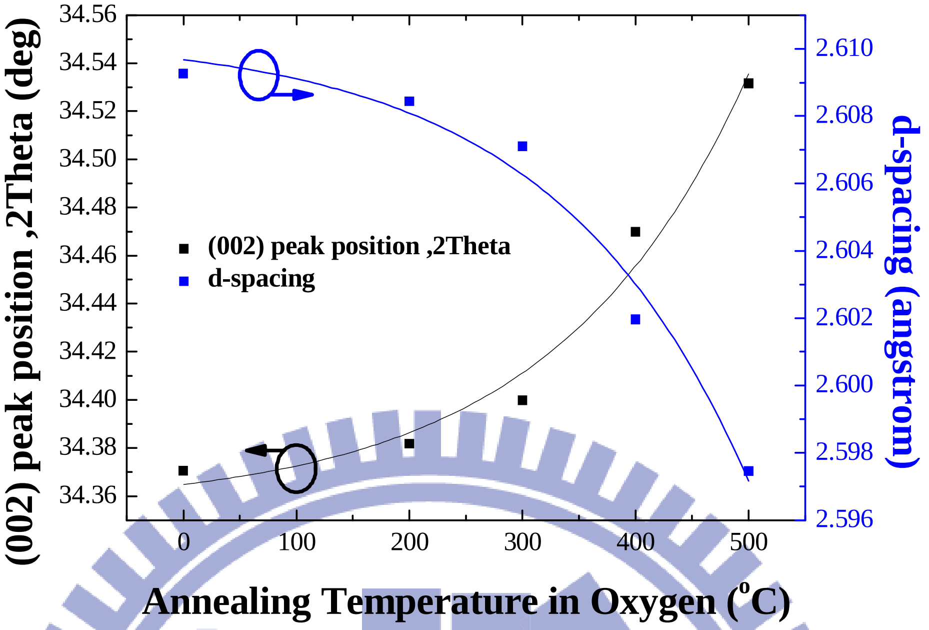

Figure 4-50 Variation of the (002) peak position and the d-spacing of IZO thin films with different annealing temperature in oxygen gas.

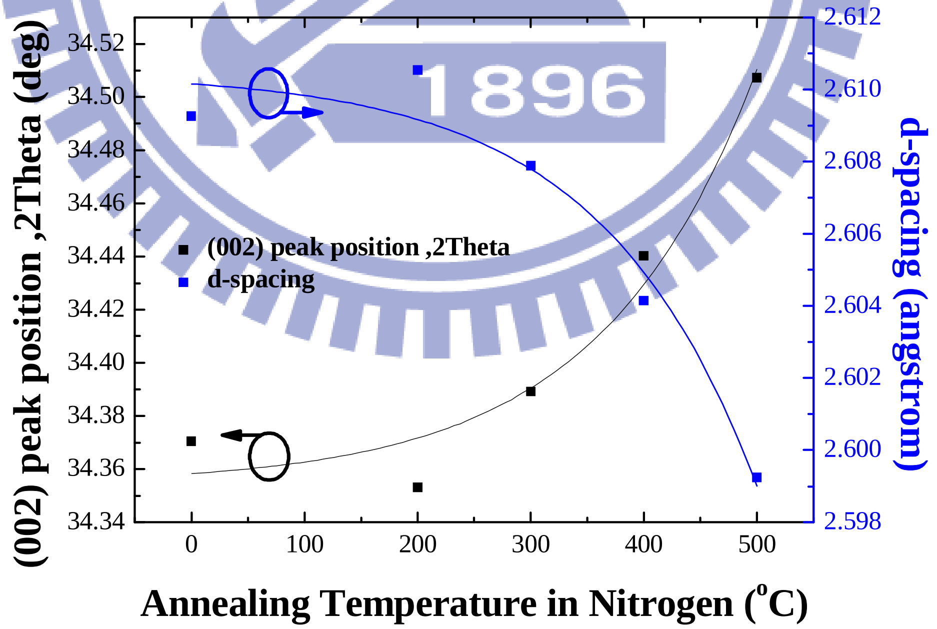

Figure 4-51 Variation of the (002) peak position and the d-spacing of IZO thin films with different annealing temperature in nitrogen gas.

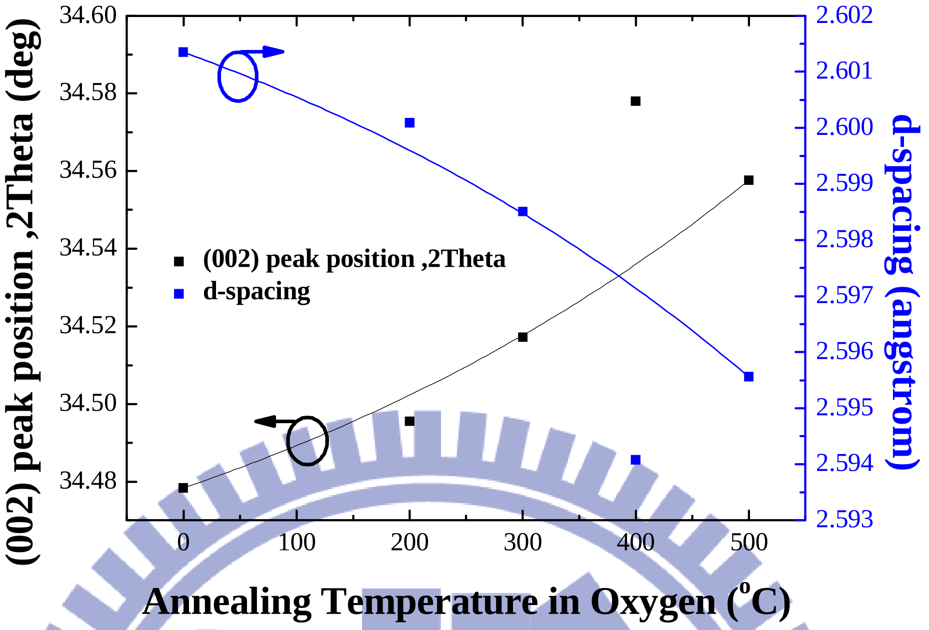

Figure 4-52 Variation of the (002) peak position and the d-spacing of GZO thin films with different annealing temperature in oxygen gas.

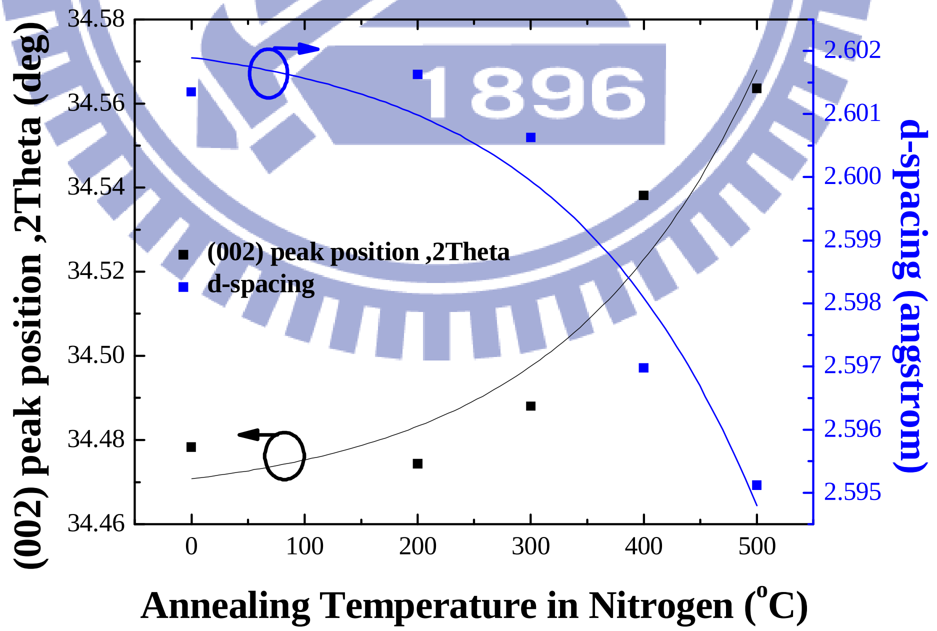

Figure 4-53 Variation of the (002) peak position and the d-spacing of GZO thin films with different annealing temperature in nitrogen gas.

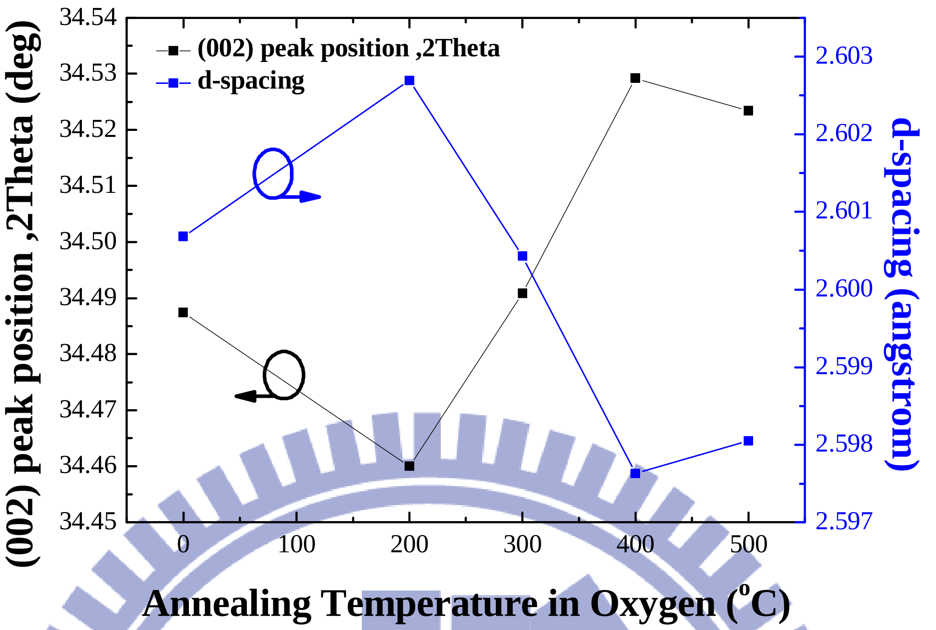

Figure 4-54 Variation of the (002) peak position and the d-spacing of ZnO thin films with different annealing temperature in oxygen gas.

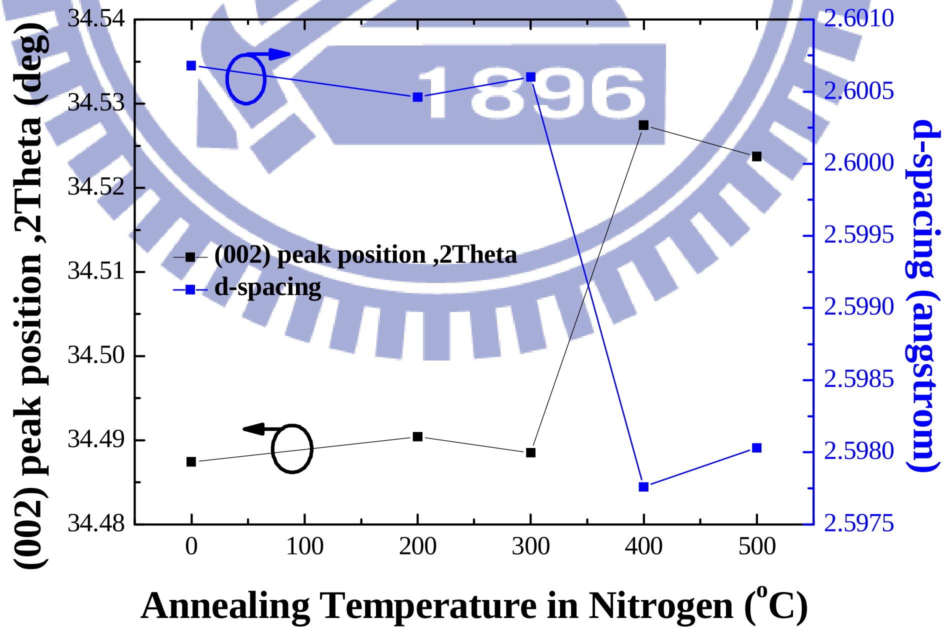

Figure 4-55 Variation of the (002) peak position and the d-spacing of ZnO thin films with different annealing temperature in nitrogen gas.

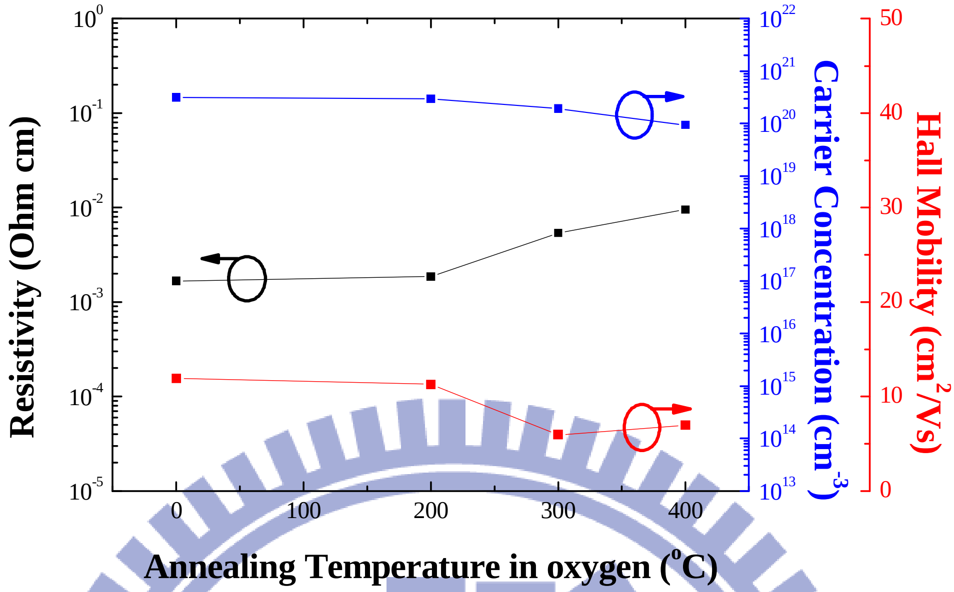

Figure 4-56 Variation of the resistivity, carrier concentration and hall mobility of IZO thin films with different annealing temperature in oxygen ambient.

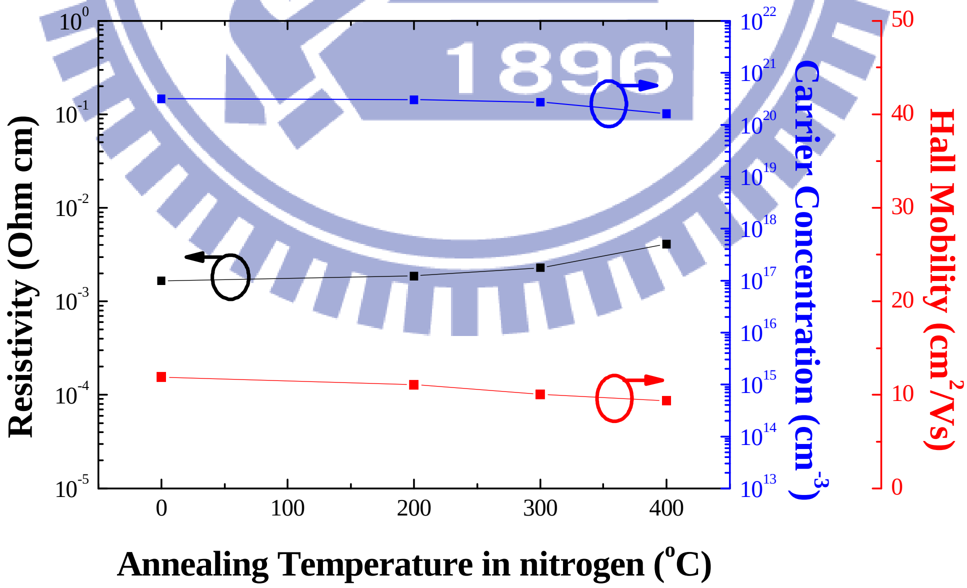

Figure 4-57 Variation of the resistivity, carrier concentration and hall mobility of IZO thin films with different annealing temperature in nitrogen ambient.

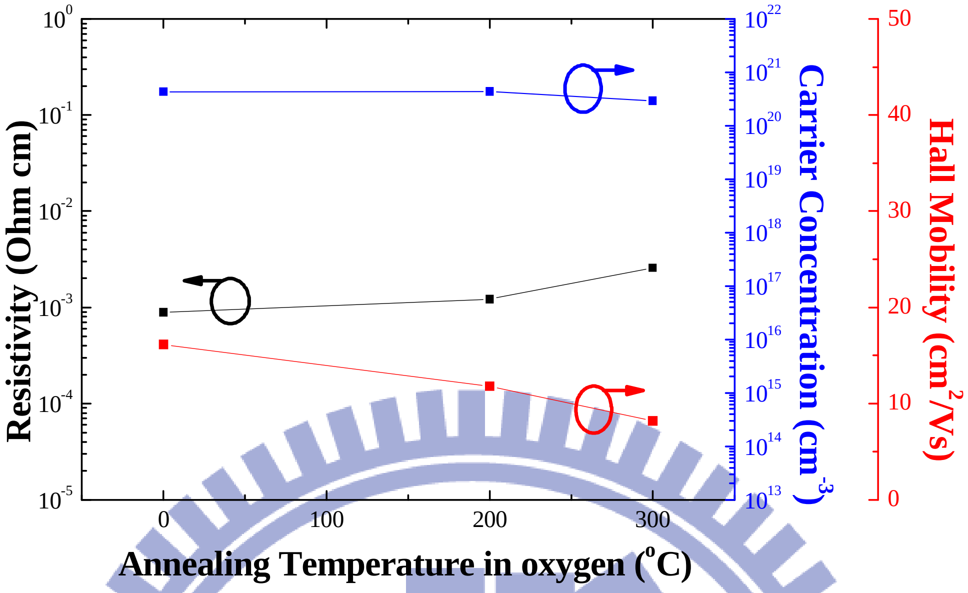

Figure 4-58 Variation of the resistivity, carrier concentration and hall mobility of GZO thin films with different annealing temperature in oxygen ambient.

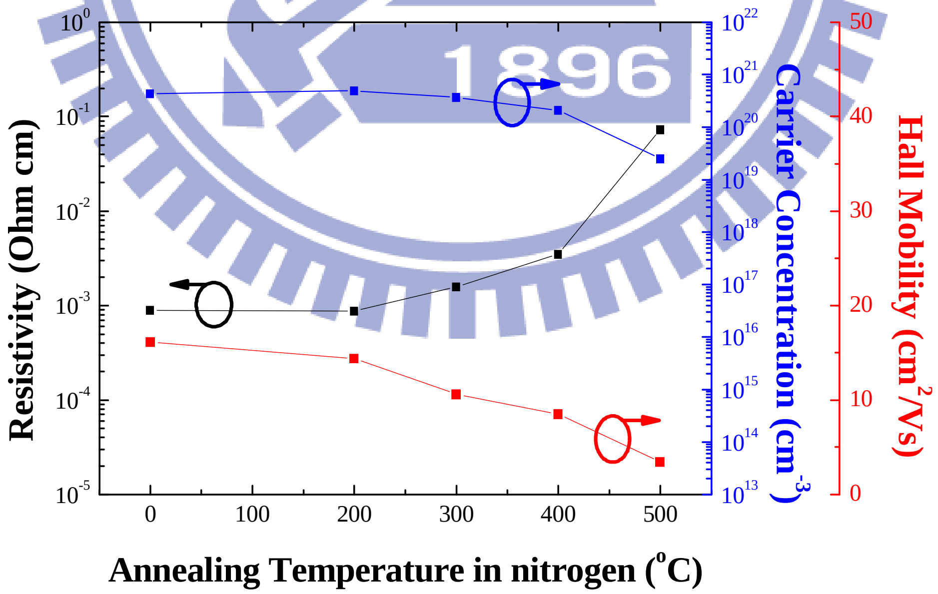

Figure 4-59 Variation of the resistivity, carrier concentration and hall mobility of GZO thin films with different annealing temperature in nitrogen ambient.

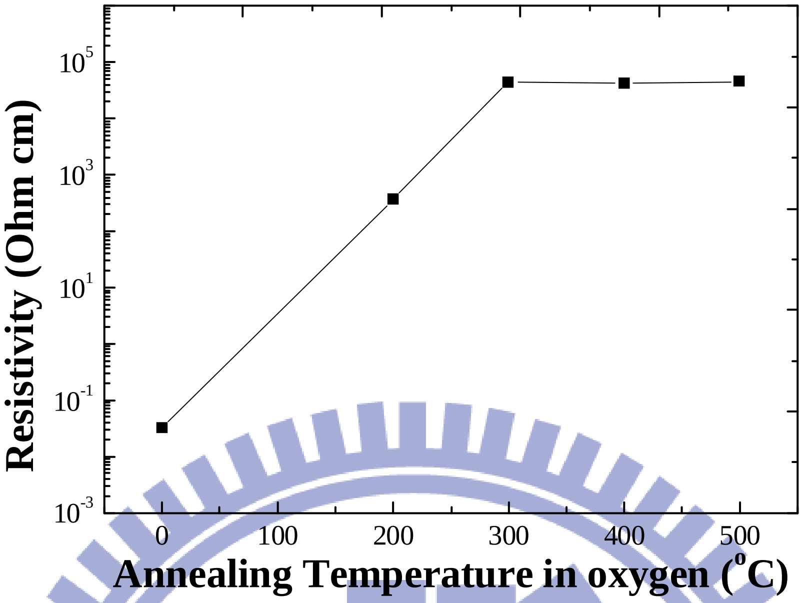

Figure 4-60 Variation of the resistivity of ZnO thin films with different annealing temperature in oxygen ambient.

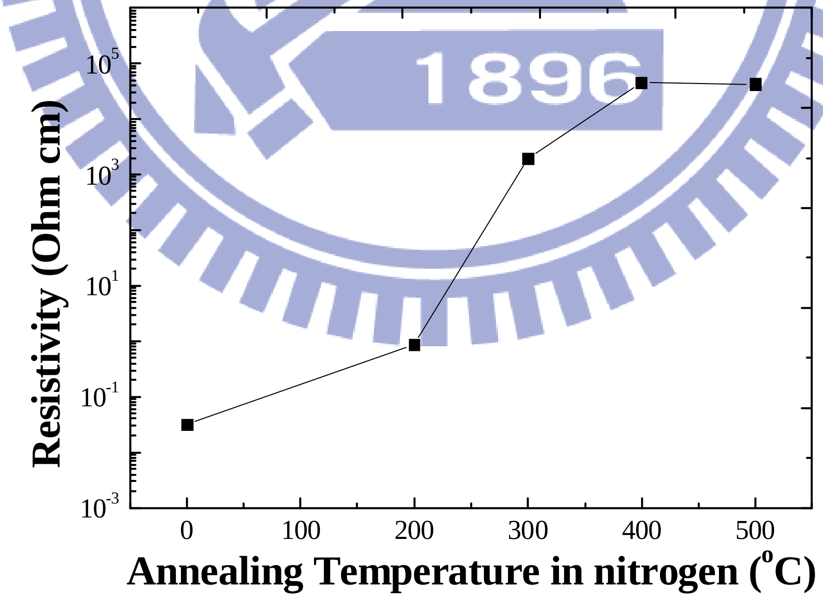

Figure 4-61 Variation of the resistivity of ZnO thin films with different annealing temperature in nitrogen ambient.

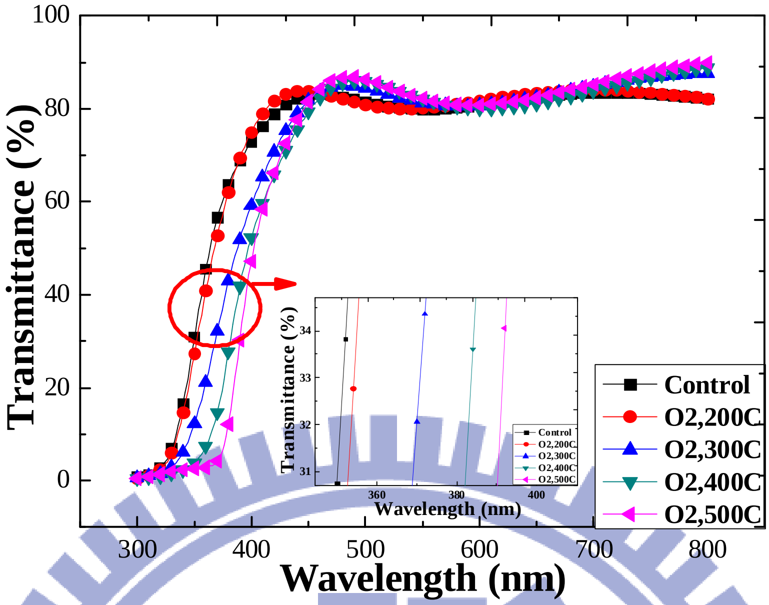

Figure 4-62 The optical transmittance spectra of IZO thin films annealed with different temperature in oxygen ambient.

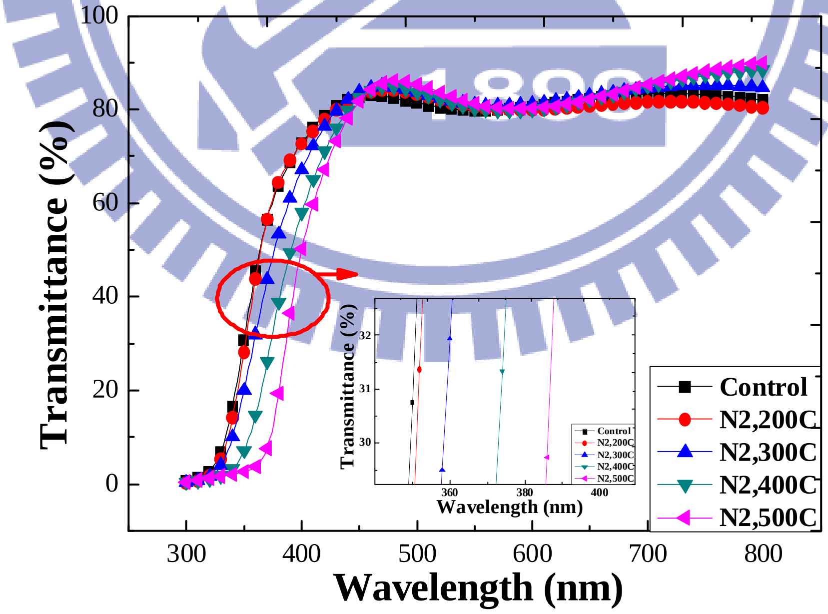

Figure 4-63 The optical transmittance spectra of IZO thin films annealed with different temperature in nitrogen ambient.

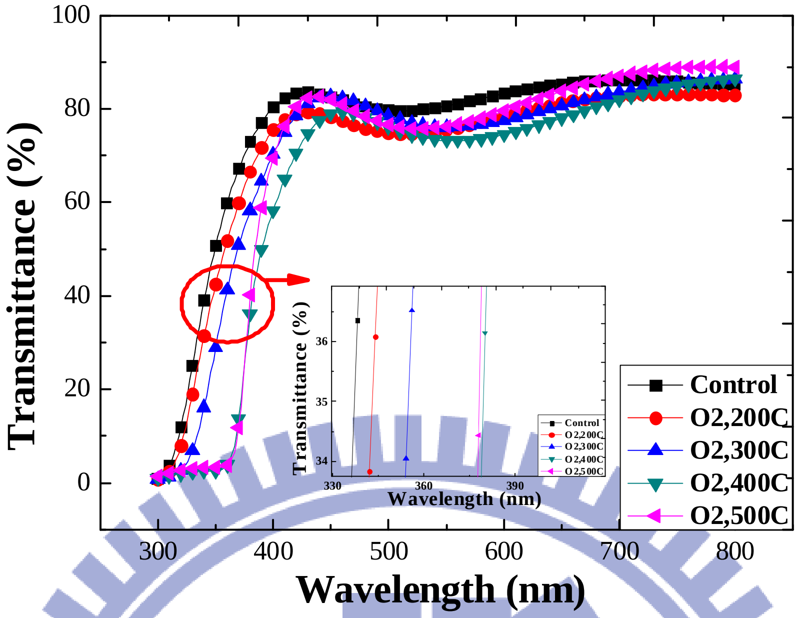

Figure 4-64 The optical transmittance spectra of GZO thin films annealed with different temperature in oxygen ambient.

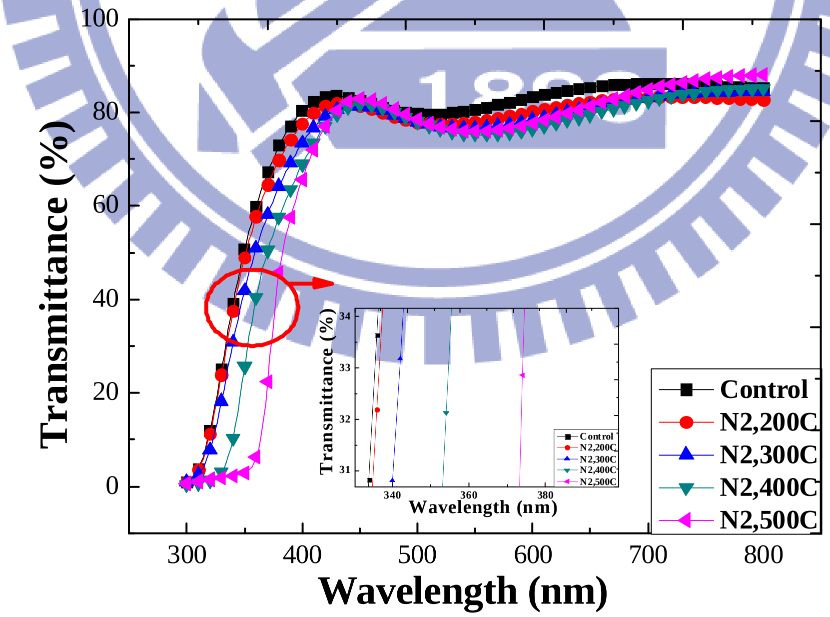

Figure 4-65 The optical transmittance spectra of GZO thin films annealed with different temperature in nitrogen ambient.

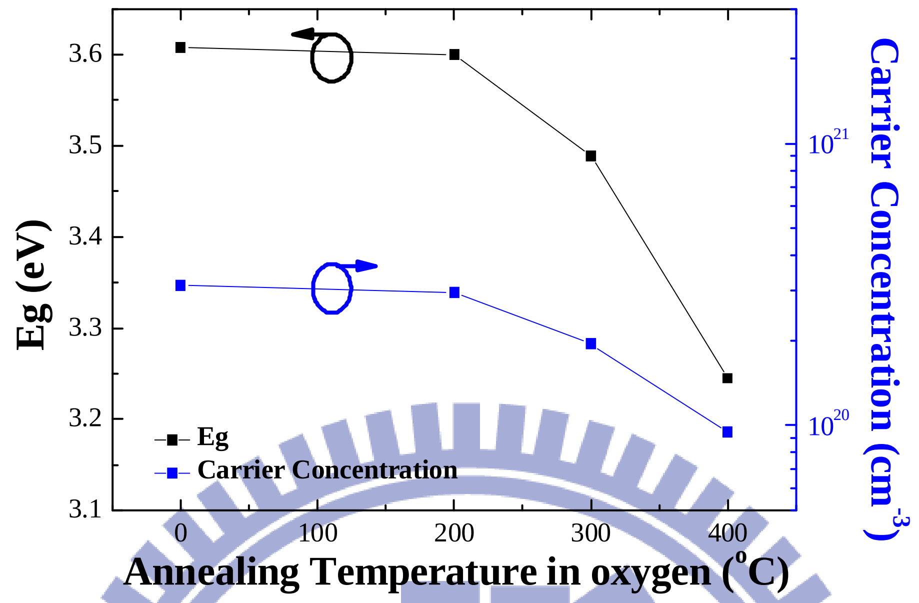

Figure 4-66 Variation of energy band gap and carrier concentration of IZO thin films annealed with different temperature in oxygen gas.

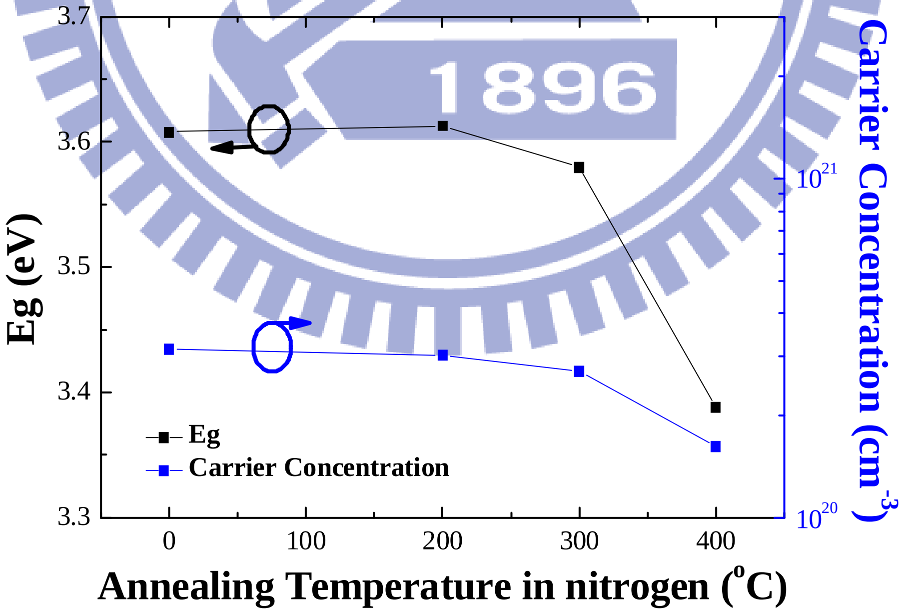

Figure 4-67 Variation of energy band gap and carrier concentration of IZO thin films annealed with different temperature in nitrogen gas.

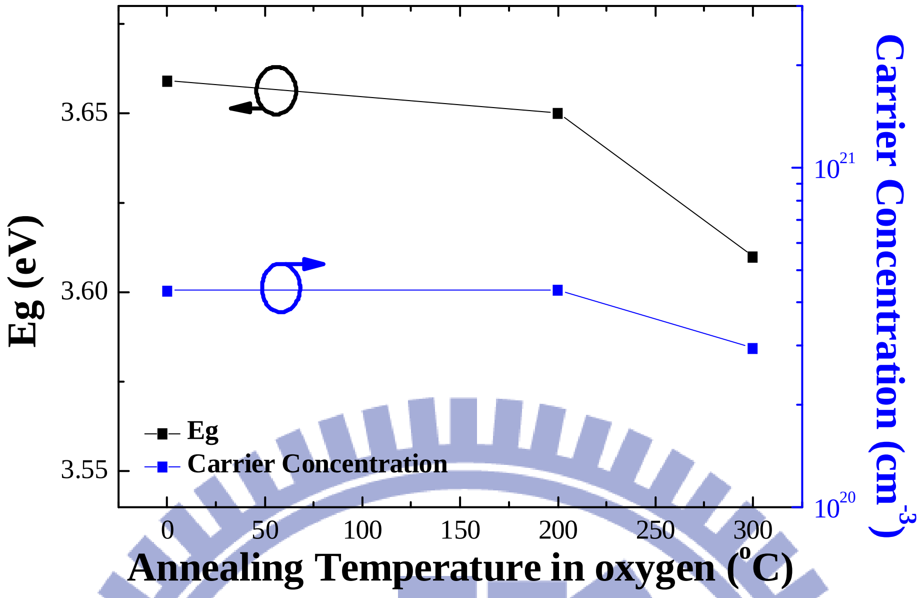

Figure 4-68 Variation of energy band gap and carrier concentration of GZO thin films annealed with different temperature in oxygen gas.

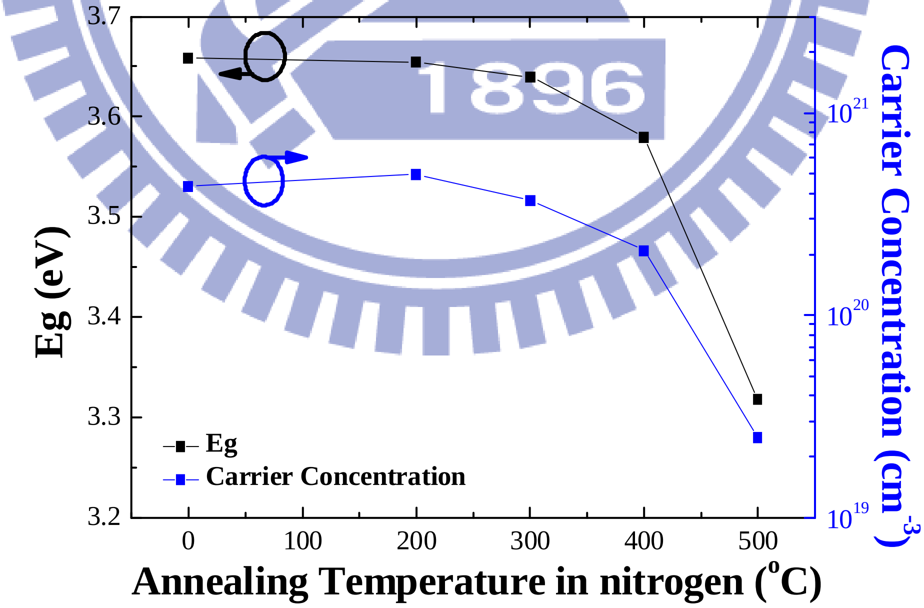

Figure 4-69 Variation of energy band gap and carrier concentration of GZO thin films annealed with different temperature in nitrogen gas.

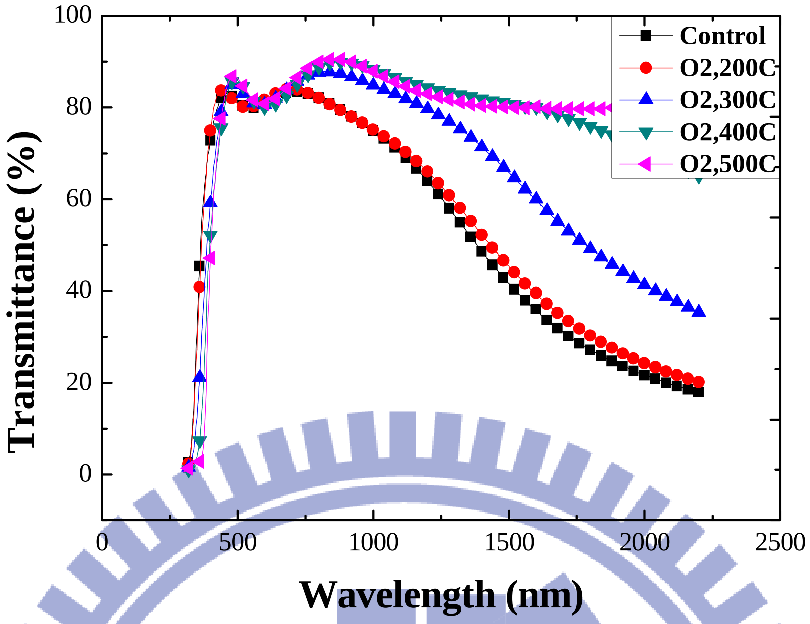

Figure 4-70 The optical transmittance spectra included IR region of IZO thin films annealed with different temperature in oxygen ambient.

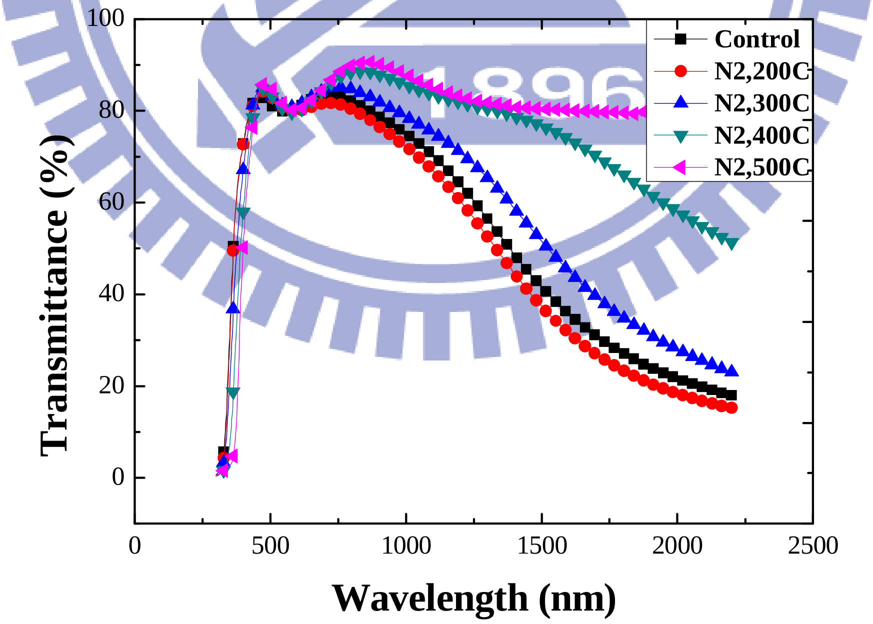

Figure 4-71 The optical transmittance spectra included IR region of IZO thin films annealed with different temperature in nitrogen ambient.

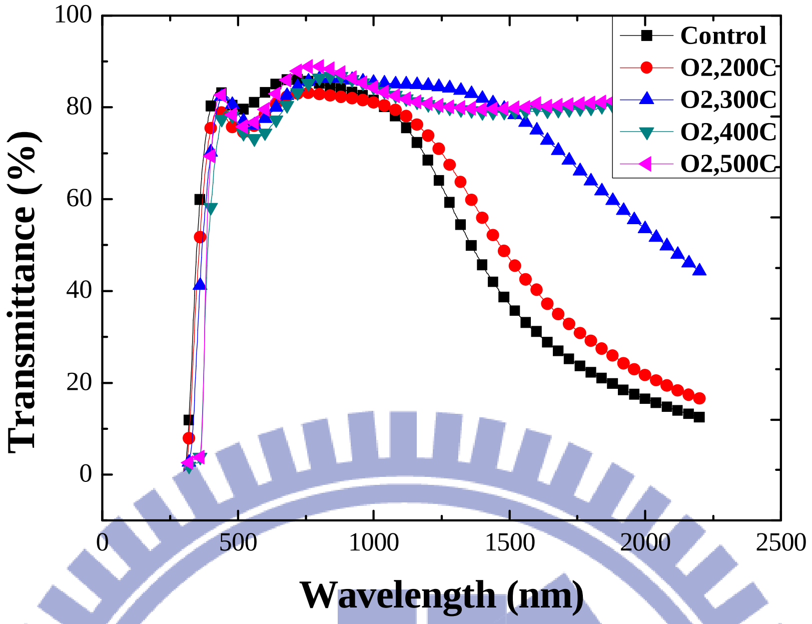

Figure 4-72 The optical transmittance spectra included IR region of GZO thin films annealed with different temperature in oxygen ambient.

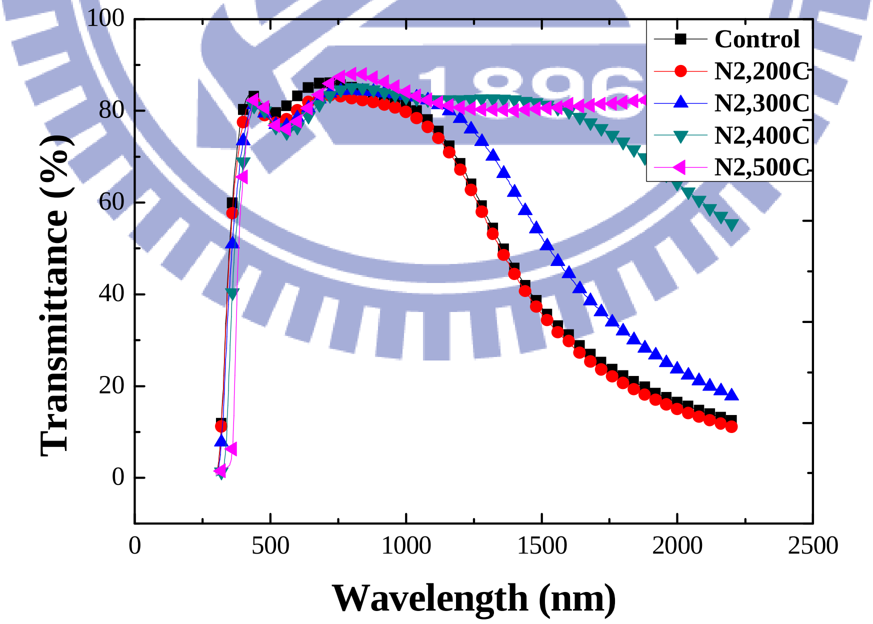

Figure 4-73 The optical transmittance spectra included IR region of GZO thin films annealed with different temperature in nitrogen ambient.

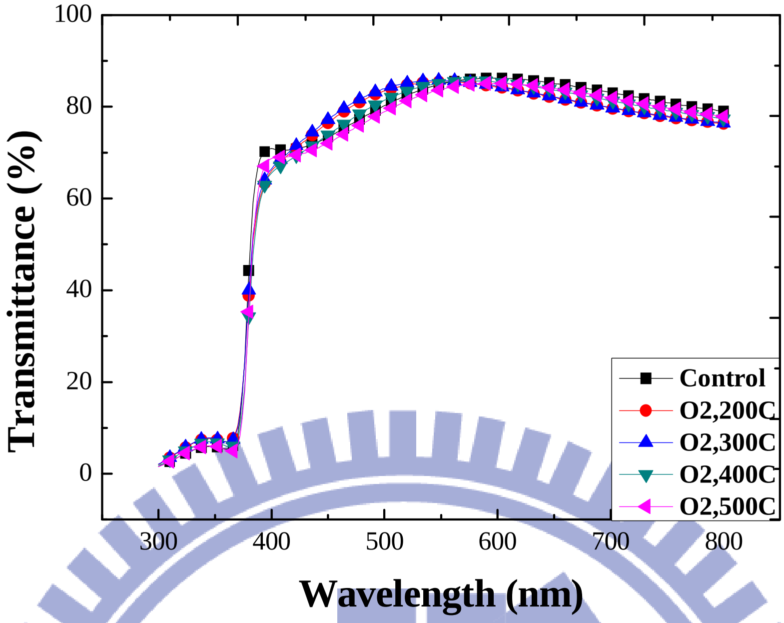

Figure 4-74 The optical transmittance spectra of ZnO thin films annealed with different temperature in oxygen ambient.

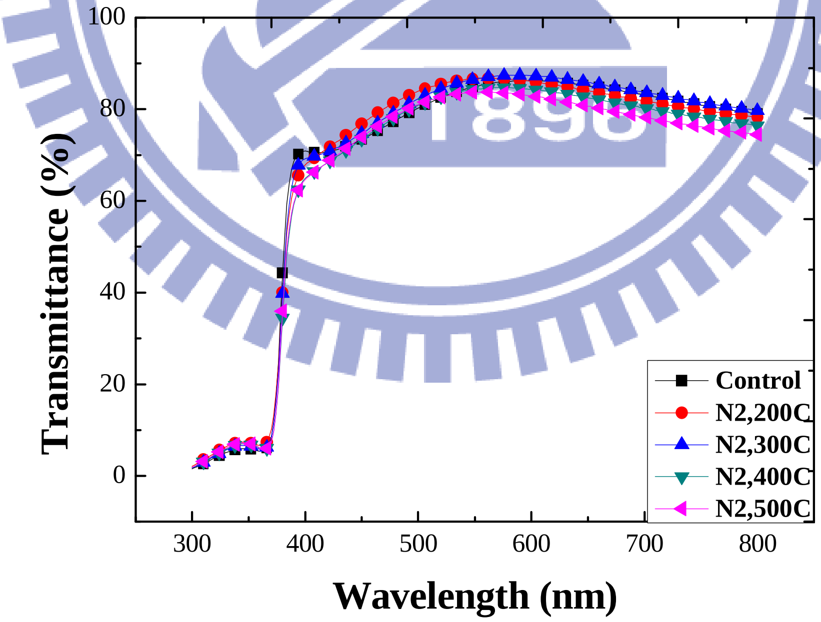

Figure 4-75 The optical transmittance spectra of ZnO thin films annealed with different temperature in nitrogen ambient.

Table 4-1 Whole data with different In concentration of IZO films

	2at%	4at%	6at%	8at%	10at%	12at%	20at%
Resistivity (Ωcm)	5.84 E-3	2.64 E-3	2.1 E-3	1.71 E-3	2.05 -3E	2.01 E-3	2.46 E-3
Mobility (cm^2/Vs)	7.174	10.2	14.72	13.51	14.62	14.48	14.94
Concentration (cm^{-3})	1.49 E20	2.32 E20	2.013 E20	2.7 E20	2.08 E20	2.14 E20	1.7 E20
Thickness(nm)	254	286	286	309	301	397	301
Rs (Ω/□)	195	57	36	28	33	28	36
Haze (%)	8.4	8.97	7.04	3.6	5.83	5.97	8.28
Transmittance (%) (at550nm)	75.57	77.42	85.36	84.05	86.96	84.55	82.41
Figure of merit (1/Ω)	3.115 E-4	1.36 E-3	5.71 E-3	6.28 E-3	7.49 E-3	6.67 E-3	4.01 E-3
Grain size(nm)	78.44	326.1	30.42	27.75	25.23	15.4	10.4
Energy band gap (ev)	3.394	3.487	3.52	3.508	3.506	3.496	3.466
Surface roughness(nm)	12.7	21.76	28.53	24.52	34.81	9.235	10.76
(002) peak position (deg.)	34.47	34.47	34.42	34.45	34.36	34.3	33.89
FWHM (2 theta)	0.447	0.366	0.614	0.641	0.671	0.881	1.139
D-spacing (Å)	2.602	2.602	2.606	2.604	2.61	2.615	2.645

Table 4-2 Whole data with different Al concentration of AZO films

	2at%	6at%	12at%	20at%
Resistivity (Ωcm)	4.78E-3	2.83E-3	2.3E-3	1.4E-3
Mobility (cm^2/Vs)	32.48	24.93	23.2	24.27
Concentration (cm^{-3})	4.021E19	8.833E19	1.172E20	1.842E20
Thickness(nm)	198	206	214	135
Rs (Ω/□)	110	46	41	50.6
Haze (%)	17.5	25.4	22	37.5
Transmittance (%) (at550nm)	71.63	63.8	69.29	52.33
Figure of merit (1/Ω)	3.233E-4	2.429E-4	6.222E-4	3.043E-5
Grain size (nm)	57.81	71.14	75.98	59.33
Energy band gap (ev)	3.34	3.38	3.46	3.46
Surface roughness(nm)	12.927	15.417	13.82	19.363
(002) peak position (deg.)	34.459	34.473	34.474	34.521
FWHM(2 theta)	0.4847	0.4577	0.4502	0.4816
D-spacing (angstrom)	2.603	2.602	2.602	2.598

Table 4-3 Whole data with different substrate temperature of IZO films

	100^{o}C	200^{o}C	300^{o}C
Resistivity (Ωcm)	6.24E-3	2.39E-3	3.29E-3
Mobility (cm^{2}/Vs)	8.318	12.94	13.35
Concentration (cm^{-3})	1.2E20	2.02E20	1.42E20
Thickness (nm)	182	270	286
Rs (Ω/□)	139	44.6	56.2
Haze (%)	7.69	4.59	2.86
Transmittance (%) (at550nm)	90.44	85.4	86.47
Figure of merit (1/Ω)	2.63E-3	4.63E-3	4.16E-3
Grain size (nm)	27.746	27.799	26.775
Energy band gap (ev)	3.451	3.461	3.41
Surface roughness(nm)	4.29	28.485	28.026
(002) peak position (deg.)	34.453	34.453	34.479
FWHM(2 theta)	0.641	0.64	0.652
D-spacing (angstrom)	2.603	2.603	2.601

Table 4-4 Whole data with different substrate temperature of AZO films

	100°C	200°C	300°C
Resistivity (Ωcm)	2.01E-3	2.31E-3	5.682E-2
Mobility (cm^2/Vs)	20.2	17.49	0.9517
Concentration (cm^{-3})	1.54E20	1.546E20	1.154E20
Thickness (nm)	139	175	230
Rs (Ω/□)	70	110	2500
Haze (%)	19	13.7	11.4
Transmittance (%) (at550nm)	73.57	76.35	64.39
Figure of merit (1/Ω)	6.636E-4	6.119E-4	4.901E-6
Grain size (nm)	53.55	66.58	110.78
Energy band gap (ev)	3.458	3.471	3.385
Surface roughness(nm)	13.339	15.423	15.691
(002) peak position (deg.)	34.4667	34.5238	34.4873
FWHM(2 theta)	0.4958	0.4655	0.4161
D-spacing (angstrom)	2.602	2.598	2.601

Table 4-5 Whole data with different annealing temperature in nitrogen ambient of GZO films

	Control	200°C	300°C	400°C	500°C
Resistivity (Ωcm)	8.9E-4	8.741E-4	1.58E-3	3.49E-3	7.284E-2
Mobility (cm^2/Vs)	16.14	14.41	10.61	8.528	3.436
Concentration (cm^{-3})	4.34E20	4.96E20	3.72E20	2.1E20	2.49E19
Thickness(nm)	294	278	294	286	286
Rs (Ω/□)(2)	28.82	37.96	62.8	280	11.1k
Transmittance (%) (at550nm)	80.59	77.82	76.66	75.27	75.94
Grain size (nm)	63.65	67.82	45.64	66.28	61.77
Energy band gap (ev)	3.659	3.655	3.64	3.58	3.318
Surface roughness(nm)	13.467	15.611	14.082	14.607	14.374
(002) peak position (deg.)	34.478	34.474	34.488	34.538	34.564
FWHM (2 theta)	0.4712	0.4633	0.5227	0.4664	0.4754
D-spacing (angstrom)	2.601	2.602	2.601	2.597	2.595

Table 4-6 Whole data with different annealing temperature in nitrogen ambient of IZO films

	Control	200°C	300°C	400°C	500°C
Resistivity (Ωcm)	1.67E-3	1.87E-3	2.29E-3	4.1E-3	1.629
Mobility (cm^2/Vs) (1)	11.9	11.1	10.06	9.388	
Concentration (cm^{-3}) (1)	3.15E20	3.01E20	2.71E20	1.62E20	
Thickness (nm)	278	278	286	294	286
Rs (Ω/□) (2)	68.36	78.75	150.8	445	56.95k
Transmittance (%) (at550nm)	79.86	80.53	81.1	80.19	81.27
Grain size(nm)	25.54	37.58	24.26	28.23	25.42
Energy band gap (ev)	3.608	3.613	3.58	3.388	3.201
Surface roughness(nm)	19.352	21.424	16.843	19.828	22.699
(002) peak position (deg.)	34.371	34.353	34.389	34.44	34.507
FWHM (2 theta)	0.666	0.562	0.684	0.636	0.668
D-spacing (angstrom)	2.609	2.611	2.608	2.604	2.599

Table 4-7 Whole data with different annealing temperature in nitrogen ambient of ZnO films

	Control	200^{o}C	300^{o}C	400^{o}C	500^{o}C
Resistivity (Ωcm)	3.2E-2	0.854	1983.72	44596.2	42716.5
Mobility (cm^2/Vs) (1)	33.34				
Concentration (cm^{-3}) (1)	5.86E18				
Thickness(nm)	202	214	183	174	185
Rs (Ω/□) (2)	5.38k	39.91k	108.4M	2.56G	2.31G
Transmittance (%) (at550nm)	84.94	86.65	86.6	84.36	83.69
Grain size (nm)	72.2	68.13	72.93	91.28	90.71
Energy band gap (ev)	3.27	3.26	3.257	3.25	3.25
Surface roughness(nm)	11.205	13.19	10.618	10.977	10.001
(002) peak position (deg.)	34.487	34.49	34.489	34.527	34.524
FWHM (2 theta)	0.456	0.453	0.455	0.432	0.433
D-spacing (angstrom)	2.601	2.6	2.6	2.598	2.598

Table 4-8 Whole data with different annealing temperature in oxygen ambient of GZO films

	Control	200°C	300°C	400°C	500°C
Resistivity (Ωcm)	8.9E-4	1.21E-3	2.59E-3	1.745	1.319
Mobility (cm^{2}/Vs) (1)	16.14	11.8	8.205		
Concentration (cm^{-3}) (1)	4.34E20	4.357E20	2.943E20		
Thickness(nm)	294	278	254	294	293
Rs (Ω/□) (2)	28.82	62.39	118.7	59.36k	45.03k
Transmittance (%) (at550nm)	80.59	75.46	76.09	73.2	76.2
Grain size (nm)	63.65	66.88	70.45	62.3	60.23
Energy band gap (ev)	3.659	3.65	3.61	3.288	3.282
Surface roughness(nm)	13.467	15.345	13.626	15.112	12.655
(002) peak position (deg.)	34.478	34.496	34.517	34.578	34.558
FWHM (2 theta)	0.471	0.465	0.459	0.474	0.479
D-spacing (angstrom)	2.601	2.6	2.599	2.594	2.596

Table 4-9 Whole data with different annealing temperature in oxygen ambient of IZO films

	Control	200°C	300°C	400°C	500°C
Resistivity (Ωcm)	1.67E-3	1.87E-3	5.4E-3	9.5E-3	18.456
Mobility (cm^2/Vs) (1)	11.9	11.27	5.932	6.944	
Concentration (cm^{-3}) (1)	3.15E20	2.97E20	1.95E20	9.46E19	
Thickness(nm)	278	286	301	278	286
Rs (Ω/□) (2)	68.36	104.6	458.3	1.494k	645.3k
Transmittance (%) (at550nm)	79.86	80.1	81.32	82.12	82.24
Grain size (nm)	25.54	44.5	28.9	26.29	71.5
Energy band gap (ev)	3.608	3.6	3.489	3.245	3.183
Surface roughness(nm)	19.352	20.857	17.019	28.485	31.088
(002) peak position (deg.)	34.371	34.382	34.4	34.47	34.532
FWHM (2 theta)	0.666	0.528	0.629	0.657	0.457
D-spacing (angstrom)	2.609	2.608	2.607	2.602	2.597

Table 4-10 Whole data with different annealing temperature in oxygen ambient of ZnO films

	Control	200°C	300°C	400°C	500°C
Resistivity (Ωcm)	3.2E-2	365.23	44329	41909.4	45599.4
Mobility (cm^2/Vs) (1)	33.34				
Concentration (cm^{-3}) (1)	5.86E18				
Thickness(nm)	202	175	194	162	198
Rs (Ω/□) (2)	5.38k	20.87M	2.285G	2.587G	2.303G
Transmittance (%) (at550nm)	84.94	85.44	85.76	85.21	83.77
Grain size (nm)	72.2	138.2	101.49	72.57	102.21
Energy band gap (ev)	3.27	3.248	3.264	3.251	3.26
Surface roughness(nm)	11.205	12.702	12.904	10.833	12.637
(002) peak position (deg.)	34.487	34.46	34.491	34.529	34.523
FWHM (2 theta)	0.456	0.401	0.423	0.455	0.422
D-spacing (angstrom)	2.601	2.603	2.6	2.598	2.598

Note: (1) The measurement value is over the instrument limit, so we can’t measure the specific data.

(1) The measurement instrument of sheet resistant is different from the above-mentioned opto-electrical properties, so the sheet resistance will be distinct value.

Chapter 5
Conclusion

We have successfully deposited IZO and AZO thin films by atmospheric pressure plasma jet. All films show a strong preferred (002) orientation perpendicular to the substrate. The best opto-electrical properties were exhibited in IZO thin films with 8at% doping concentration. The lowest resistivity and its transmittance were the value of 1.71E-3 and 84.05% respectively. AZO thin films were easy influenced by air ambient, causing difficult to control the processing conditions. IZO thin films show better thermal stability than GZO and ZnO thin films in both nitrogen and oxygen gases below 400^{o}C temperature environment.

Chapter 6

Future Work

I am presenting primary results of a novel experiment that will be further analyzed, expanded and replicated. We can deposit IZO thin films on large area substrate to demonstrate the application of FPDs. The IZO films incorporated with other group III elements that may be promoted the opto-electrical properties. Increasing the mole ratio of In doping concentration to make the amorphous IZO thin films which were shown in our experiments used in TFT application. Minimization the effect of air ambient might control the processing condition more specific. The large area and high deposition rate will achieved by using multiple jets to deposit TCO thin films. Annealing in the forming gases at high temperature that may be improved the optical and electrical characterizations of IZO and GZO thin films.

.

Reference

[1] A.L.DawarandJ.C.Joshi,J.Marer.Sci., 19(1984) 1

[2] K.L. Chopra, S. Major and D.K. Pandya, Thin Solid Films, 102 (1983) 1

[3] I. Hamberg and C.G. Granqvist, J. Appl. Phys., 60 (1986) R123

[4] T. Minami, H. Sato, H. Nanto and S. Takata, Jpn. J. Appl. Phys., 24 (1985) L781

[5] B. Rech, T. Repmann, S. Wieder, M. Ruske, U. Stephan, Thin Solid Films 502 (2006) 300

[6] T. Mizuta, T. Ishibashi, T. Minemoto, H. Takakura, Y. Hamakawa, Thin Solid Films 515 (2006) 2458

[7] W.J. Jeong, S.K. Kim, G.C. Park, Thin Solid Films 180 (2006) 506

[8] S. Major, A. Banerjee, K.L. Chopra, Thin Solid Films 143 (1986) 19

[9] E.V. Lavrov, Physica B 195 (2003) 340

[10] K. Tabuchi, W. W. Wenas, A. Yamada, M. Konagai and K. Kakahashi: Jpn. J. Appl. Phys. 32 (1993) 3764

[11] R. T. Tuenge, Digest 1991 SID Int. Symp., Anaheim, CA ~Society for Information Display, Anaheim, CA, 1991!, p. 279

[12] F. S. Becker, D.Pawlik, H. Anzinger, A. Spitizer, J. Vac. Sci.Technol. B, Vol 5, No 6, pp 1555-1563, Nov / Dec 1987

[13] S. C. Deshmukha, E. S. Aydilb, J. Vac. Sci.Technol. A, Vol 13, No 5, pp 2355-2367, Sep / Oct 1995

[14] J. D. Chapplesokol, W. A. Pliskin, R. A. Conti, J. Electrochem. Soc., Vol. 138, No. 12, pp 3723-3726, December 1991

[15] P. Mitra, A.P. Chatterjee, H.S. Maiti, Mater. Lett. 35 (1998) 33

[16] C.H. Kwon, H.K. Hong, D.H. Yun, K. Lee, S.T. Kim, Y.H. Roh, B.H. Lee, SensorsActuators B 25 (1995) 610

[17] J.B. Yoo, A.L. Fahrenbruch, R.H. Bube, J. Appl. Phys. 68 (1990) 4694

[18] D. Dimova-Malinovska, J. Lumin. 80 (1999) 207

[19] Z.-C. Jin, I. Hamberg, C.G. Granqvist, B.E. Sernelius, K.-F. Berggren, Thin Solid Films 164 (1988) 381

[20] J.G.E. Gardeniers, Z.M. Rittersma, G.J. Burger, J. Appl. Phys. 83 (1998) 7844

[21] S.B. Majumder,M. Jain, P.S. Dobal, R.S. Katiyar, Mater. Sci. Eng. B 103 (2003) 16

[22] S. Ghosh, A. Sarkar, S. Chaudhuri, A.K. Pal, Thin Solid Films 205 (1991) 64

[23] W.W. Wang, X.G. Diao, Z. Wang, M. Yang, T.M. Wang, Z. Wu, Thin Solid Films 491 (2005) 54

[24] C. Xu, M. Kim, J. Chun, D. Kim, Appl. Phys. Lett. 86 (2005) 133107

[25] M. Go¨ ppert, F. Gehbauer, M. Hetterich, J. Mu¨ nzel, D. Queck, C. Klingshirn, J. Lumin. 72–74 (1997) 430

[26] X. Yu, J. Ma, F. Ji, Y. Wang, C. Cheng, H. Ma, Appl. Surf. Sci. 245 (2005) 310

[27] S.Y. Bae, C.W. Na, J.H. Kang, J. Part, J. Phys. Chem. B 109 (2005) 2526

[28] Th. Agne, Z. Guan, X.M. Li, H. Wolf, Th. Wichert, H. Natter, R. Hempelmann, Appl. Phys. Lett. 83 (2003) 1204

[29] H. Gomez, A. Maldonado, R. Asomozo, E.P. Zironi, J. Canetes-

Ortega, J. Palacios-Gomez, Thin Solid Films 293 (1997) 117

[30] P.M. Ratheesh Kumar, C. Sudha Kartha, K.P. Vijayakumar, T. Abe, Y. Kashiwaba, F. Singh, D.K. Avasthi, Semicond. Sci. Technol. 20 (2005) 120

[31] A. Maldonado, R. Asomoza, J. Canetas-Ortega, E.P. Zironi, R. Hernandez, R. Patino, O. Solorza-Feria, Sol. Energy Mater. Sol. Cells 57 (1999) 331

[32] M. Miki-Yoshida, F. Paraguay-Delgado, W. Estrada-Lopez, E. Andrade, Thin Solid Films 376 (2000) 99

[33] C. Klingshirn, Phys. Status Solidi B 71 (1975) 547

[34] F.H. Nicoll, Appl. Phys. Lett. 9 (1996) 13

[35] J.M. Hvam, Solid State Commun. 12 (1973) 95

[36] Segawa Y, Ohtomo A, Kawasaki M, Koinuma H, Tang Z K, Yu P and Wong G K L 1997 Phys. Status Solidi b 202 669

[37] Cooray N F Y, Kushiya K, Fujimaki A, Okumura D, Sato M, Ooshita M and Yamase O 1999 Japan. J. Appl. Phys. 38 6213

[38] K. Nomura, H. Ohta, K. Ueda, T. Kamiya, M. Hirano, H. Hosono, Science 300 (2003)

[39] N. Xu, L. Liu, X. Sun, X. Liu, D. Han, Y. Wang, R. Han, J. Kang, and B. Yu, Appl. Phys. Lett. 92, 232113 (2008)

[40] W. Y. Chang, Y. C. Lai, T. B. Wu, S. F. Wang, F. Chen, and M. J. Tsai, Appl. Phys. Lett. 92, 022110 (2008)

[41] S. Kim, H. Moon, D. Gupta, S. Yoo, and Y. K. Choi, IEEE Trans. Electron Devices, 56, 4 (2009)

[42] 楊明輝編著, “透明導電膜”, 藝軒圖書出版社出版, 2006

[43] J. Ma, F. Ji, H. Ma, S. Li, J. Vac. Sci. Technol. A 13 (1995) 92–94

[44] B.H. Choi, H.B. Im, J.S. Song, K.H. Yoon, Thin Solid Films 193 (1990) 712

[45] V. Assunção, E. Fortunato, A. Marques, H. Águas, I. Ferreira, M.E.V. Costa, R. Martins, Thin Solid Films 427 (2003) 401

[46] R. Groenen, J.L. Linden, H.R.M. van Lierop, D.C. Schram, A.D. Kuypers, M.C.M. van de Sanden, Appl. Surf. Sci. 173 (2001) 40–43

[47] Myoung J M, Yoon W H and Lee D H 2002 Japan. J. Appl. Phys. 41 28

[48] J. Chang, P. Lawless, T. Yamamoto, IEEE Trans. Plasma Sci., Vol. 19, Issue 6, pp 1152-1166, 1991

[49] Ye J.D., Gu S.L., Zhu S.M., Liu S.M., Zheng Y.D., Zhang R., Shi Y., Yu H.Q., Ye Y.D., J. Cryst. Growth, 283 (2005), 279

[50] Ghosh R., Paul G.K., Basak D., Mater. Res. Bull., 40 (2005), 1905

[51] M. Goldman, N Goldman, Gaseous Electronics, Academic, Vol. 1,New York, 1978

[52] H. Ohmi, H. Kakiuchi, K. Nishijima, H. Watanabe, K. Yasutake, J. Appl. Phys., Vol. 45, No. 10B, pp 8488-8493, Oct 2006

[53] S. Babayan, J.Y. Jenog, A. Schutze, V.J. Tu, M. Moravej, G.S. Selwyn, R.F. Hicks, Plasma Sources Sci. Technol. Vol. 10, Issue 4, pp 573-578, Nov 2001

[54] Ayouchi R., Leinen D., Martin F., Gabas M., Dalchiele E., Ramos-Barrado J. R., Thin Solid Films, 426 (2003) 68

[55] Martins R., Igreja R., Ferreira I., Marques A., Pimentel A., Goncalves A., Fortunato E., Mat. Sci. Eng. B, 118 (2005), 135

[56] B. Eliasson, U Kogelschatz, IEEE Trans. Plasma Sci., Vol.19, Issue6, pp 1063-1077, Dec 1991

[57] V. Gibalov, G. Pietsch, J. Phys. D: Appl. Phys., Vol.33, Issue 20, pp 2618-2636, Oct 2000

[58] S. Kanazawa, M. Kogoma, T. Moriwaki, J. Phys. D: Appl. Phys., Vol.21, Issue 5, pp 838-840, May 1988

[59] T. Yokoyama, M. Kogoma, S. Okazaki, J. Phys. D: Appl. Phys., Vol. 23, Issue 8, pp 1125-1128, Aug 1990

[60] D. Trunec, A. Brablec, F. Stastny, Contrib. Plasma Phys., Vol. 38, Issue 3, pp 435-445, 1998

[61] Sematech, "Deposition Processes in Furnace Processes and Related Topics", Austin, pp 6, 1994

[62] J. Bulow, K. Rogoff, Quar. J.Econ., Vol. 106, Issue 4, pp 1219-1235, Nov 1991

[63] J. Roth, Industrial Plasma Engineering, Vol. I, Principles, Institute of Physics Publishing, Bristol and Philadelphia, 1995

[64] Leszczynski, M. (1999) Common crystal structure of the group III-nitrides, in Properties, Processing and Applications of Gallium Nitride and Related Semiconductors (eds J.H. Edgar, S. Strite, I. Akasaki, H. Amano and C.Wetzel), EMIS Datareviews Series No. 23, INSPEC, The Institution of Electrical Engineers, Stevenage, UK, pp. 3–5

[65] Ambacher, O., Majewski, J., Miskys, C., Link, A., Hermann, M., Eickhoff, M., Stutzmann, M., Bernardini, F., Fiorentini, V., Tilak, V., Schaff, B. and Eastman, L.F. (2002) Pyroelectric properties of Al(In)GaN/GaN heteroand quantum well structures. Journal of

Physics: Condensed Matter, 14, 3399

[66] Leszczynski, M., Suski, T., Perlin, P., Teisseyre, H., Grzegory, I., Bockowski, M., Jun, J., Porowski, S., Pakula, K., Baranowski, J.M., Foxon, C.T. and Cheng, T.S. (1996) Applied Physics Letters, 69, 73

[67] Speed Tech, Home page, All production, Interface parts, Sputtering Application

[68] P. Nash and R. F. Bunshah, Thin Solid Films 69 (1980) 63

[69] P. Nash, R. F. Bunshah, B. M. Basol and O. M. Staffsud, Yhin Solid Films 72 (1980) 463

[70] T. J. Jackson, S. B. Palmer, J. Phys. D: Appl. Phys., Vol. 27, 1581 (1994)

[71] J. C. Viquie’ and J. Spitz, J. Electrochem. Soc.: Solid-State Sci. Technol. 122 [4] (1975) 585

[72] H. Schmidt and M. Mennig, The Sol-Gel Gateway, November (2000)

[73] JunSun Tech, atomic layer deposition, December (2006)

[74] H. O. Pierson, Handbook of Chemical Vapor Deposition, Noyes Publications, Park Ridge (1992)

[75] G. B. Stringfellow, Organometallic Vapor-Phase Epitaxy: Theory and practice, Academic Press, New York (1994)

[76] H. Xiao, Introduction to semiconductor manufacturing technology, PersonED Publications, (2001)

[77] TFOT, Home, Articles, Computer Technology, Ionic Wind-Chillin’ the PC, (2007)

[78] Kinema Research & Software, L.L.C., Multi-Dimensional Modeling of Dielectric Barrier Discharges Using PLASMATOR, (2003)

[79] Apjet, Textile Applications, Key Concepts, (2004)

[80] Dr. Dmitri Kopeliovich, Plasma arc wielding, SubsTech, (2009)

[81] A. Schutze, J. Jeong, S. Babayan, J. Park, G. Swlwyn, R. Hicks, IEEE Tran. Plasma Sci., Vol.26, Issue 6, pp 1685-1694, Dec 1998

[82] J.Y. Seto, J. Appl. Phys. 46, 5247 (1975)

[83] B. E. Sernelius, K. F. Berggren, Z. C. Jin, I. Hamberg and C. G Granqvist: Phys. Rev. B 37 (1988) 10244

[84] J. C. Tsang, P. J. Dean, and P. T. Landsberg, Phys. Rev., 173, 814 (1998)

[85] V. Swaminathan, A. T. Macrander, Materials Aspects of GaAs and InP Based Structures (Prentice-Hall, New Jersey, 1982), p. 319

[86] Lin B, Fu Z and Jia Y 2001 Appl. Phys. Lett. 79 943

簡歷

姓　　名：林煒力

性　　別：男

出生日期：民國 74 年 10 月 22 日

出生地：　台灣省彰化縣

住　　址：台灣省彰化縣永靖鄉永南村永西路 137 巷 36 號

學　　歷：員林高中

(民國 90 年 09 月～民國 93 年 06 月)

國立彰化師範大學電機工程學系

(民國 93 年 09 月～民國 97 年 06 月)

國立交通大學電機學院電子工程研究所碩士班

(民國 97 年 09 月～民國 99 年 07 月)

碩士論文：利用大氣電漿沉積以氧化鋅為主的透明導電膜其光電特性和熱穩定性的研究

Investigation on Opto-electrical Properties and Thermal Stability of Zinc Oxide Based Transparent Conductive Oxides Prepared by Atmospheric Pressure Plasma Jet